A locally modified finite element method for two-phase flow problems

Dissertation

zur Erlangung des akademischen Grades

doctor rerum naturalium
(Dr. rer. nat.)

von Gozel Judakova, M.Sc.
geb. am 15.01.1975 in Lebap

genehmigt durch die Fakultät für Mathematik
der Otto-von-Guericke-Universität Magdeburg

Gutachter: Prof. Dr. rer.nat. Thomas Richter
Univ.-Prof. Dr. rer. nat. habil. Thomas Apel

eingereicht am: 24.10.2022
Verteidigung am: 18.04.2023

Abstract

In this thesis, we extend the locally modified finite element method, which is introduced in [47], to second order in two space dimensions. The method is based on a fixed patch mesh, which is then refined into sub-elements, to resolve an interface locally. The splitting into sub-elements is slightly different from the one presented in [47] and leads in general to a better bound for the maximal angles within the triangles.

We begin in the stationary case by analysing a locally modified second order finite element method applied to elliptic interface problems. We prove some auxiliary estimates in order to control the mismatch between continuous and discrete bilinear forms and then show an optimal a priori error estimates in the L^2-norm and in the discrete energy norm.

Furthermore, we study two-phase flow problems and show stability. For the discretization of the stationary Stokes interface problem, we apply a locally modified second order finite element scheme for the velocity and piecewise constant elements for the pressure. The technique used to check the inf-sup stability is a macroelement technique, which is tested by checking local stability and a relatively simple global stability. For that we use a two-level family of meshes, i.e. micro- and macrotriangulation. First, we show the stability locally for each macroelement by constructing a Fortin operator. There is only one rare case, where the macroelement is not stable and we must add further stabilization terms. Second, we define a subspace by introducing an appropriate projection and show the stability of the subspace. With the macroelement approach, we prove a discrete inf-sup condition for the $\mathcal{P}_2 - \mathcal{P}_0$ element and present optimal error estimations. Moreover, we consider Stokes interface problems with surface tension. In the variational formulation of these problems, we use a linear functional which describes the surface tension force. This functional depends on the location and the curvature of the interface. To handle the curvature, we apply a Laplace-Beltrami operator. Compared to one-phase flows, two-phase flows with a surface tension force have very high numerical complexity. Thus, we use the Rothe method. For time discretization, we use the implicit Euler method for the unsteady Stokes problem combined with a semi-implicit time integration of the surface tension force. For spatial discretization, we use the locally modified second order finite element method.

In the final part of the thesis, we study a fluid-structure-interaction problem. We consider a rigid body model for falling particles and an unsteady Stokes problem for the fluid model. For spatial discretization, we use the locally modified finite element scheme and the implicit Euler method for time discretization. To evaluate the solution on the new spatial mesh, we use the discrete Stokes projection.

We present detailed numerical studies for all three applications including a numerical convergence analysis.

Zusammenfassung

In dieser Arbeit erweitern wir die in [47] eingeführte lokal modifizierte Finite-Elemente-Methode auf die zweite Ordnung in zwei Raumdimensionen. Die Methode basiert auf einem fest strukturierten groben Gitter, das dann in Unterelemente verfeinert wird, um das Interface lokal aufzulösen. Die Aufteilung in Unterelemente unterscheidet sich von der in [47] vorgestellten und das führt zu einer besseren Begrenzung für der maximale Winkel des Dreiecks.

Zunächst betrachten wir den stationären Fall und analysieren eine lokal modifizierte Finite-Elemente-Methode zweiter Ordnung für elliptische Interface-Problems. Wir beweisen einige Hilfs-Abschätzungen, um den Unterschied zwischen kontinuierlichen und diskreten bilinearen Formen zu kontrollieren. Dann zeigen wir optimale a priori-Fehlerschätzungen in der L^2-Norm und in der diskreten Energie-Norm.

Weiterhin untersuchen wir Zweiphasenströmungsprobleme und zeigen die Stabilität. Für die Diskretisierung des stationären Stokes-Interface-Problems verwenden wir lokal modifizierte Finite-Elemente-Schemata zweiter Ordnung für die Geschwindigkeit und stückweise konstante Elemente für den Druck. Um die inf-sup Stabilität zu überprüfen, verwenden wir die Makroelementtechnik, die durch die lokale Stabilität und eine relativ einfache globale Stabilität getestet wird. Dafür verwenden wir eine zweistufige Familie von Gittern, d.h. eine Mikro- und Makrotriangulation. Zunächst zeigen wir die lokale Stabilität für jedes Makroelement durch Konstruktion des Fortin-Operators. Es gibt nur einen seltenen Fall, in dem das Makroelement nicht stabil ist. Wir müssen in diesem Fall einen Stabilisierungsterm hinzufügen. Zweitens definieren wir einen Unterraum durch eine geeignete Projektion und zeigen die Stabilität des Unterraums. Mit Hilfe der Makroelementtechnik beweisen wir die diskrete Inf-Sup-Bedingung für die $\mathcal{P}_2 - \mathcal{P}_0$-Elemente und präsentieren die optimalen Fehlerschätzungen. Darüber hinaus betrachten wir die Stokes-Interface-Probleme mit der Oberflächenspannung. Bei der Variationsformulierung dieser Probleme verwenden wir ein lineares Funktional, das die Oberflächenspannungskraft beschreibt. Dieses Funktional hängt von dem Ort und der Krümmung des Interfaces ab. Daher wenden wir einen Laplace-Beltrami-Operator an, um die Krümmungsterm zu behandeln. Im Vergleich zu Einphasenströmungen haben Zweiphasenströmungen mit Oberflächenspannungskräften eine sehr hohe numerische Komplexität. Deswegen wenden wir die Rothe-Methode an. Für die Zeitdiskretisierung verwenden wir die implizite Euler-Methode für das instationäre Stokes-Problem in Kombination mit einer semi-impliziten Zeitintegration der Oberflächenspannungskraft. Für die räumliche Diskretisierung verwenden wir die lokal modifizierte Finite-Elemente-Methode zweiter Ordnung.

Im letzten Teil dieser Arbeit betrachten wir ein Fluid-Struktur-Interaktionsproblem. Wir betrachten ein Starrkörpermodell für fallende Partikel und ein instationäres Stokes-

Problem für das Fluidmodel. Für die örtliche Diskretisierung verwenden wir das lokal modifizierte Finite-Elemente-Schema zweiter Ordnung und für die Zeitdiskretisierung das implizite Euler-Verfahren. Um die Lösung auf dem neuen räumlichen Gitter zu bewerten, entwickeln wir die diskrete Stokes-Projektion.

Wir präsentieren detaillierte numerische Studien für alle drei Anwendungen, einschließlich einer numerischen Konvergenzanalyse.

Contents

Chapter 1: Introduction

In this thesis, we investigate interface problems, where the normal derivative of the solution may have a jump over an interior interface.
Examples of such interface problems are ubiquitous in technology, industry, science and medicine. Some of the most prominent examples include fluid-structure interactions [17,83] or multiphase flows [58]. Fluid-structure interactions arise in aerodynamical applications like flow around the airplanes or parachutes [88], in the biomedical problems such as a blood flow through the cardiovascular system [43, 81, 94] or the airflow within the respiratory system [98] and even in the tribological applications [71]. Multiphase problems include gas-liquid and particle-laden gas flows [33, 60, 69], rising bubbles [67], droplets in microfluidic devices [31] or simulations of tumor growth [57]. Another field of application are shape or topology optimization problems including multi-component structures [30, 56].
The simplest possible setting, which is the scope of this thesis, is a diffusion problem where the diffusion coefficient is discontinuous across an interior interface.

1.1 Motivation

The aim of this thesis is to develop accurate discretization techniques for interface problems. We assume that the domain $\Omega \subset \mathbb{R}^2$ is divided into $\Omega = \Omega_1 \cup \Gamma \cup \Omega_2$ with an interior interface $\Gamma := \partial\Omega_1 \cap \partial\Omega_2$. Let $\nu > 0$ be a discontinuous diffusion coefficient across Γ. In order to simplify the analysis, we will assume that the domain Ω is a two-dimensional convex domain with polygonal boundary. We consider the equations for $i = 1, 2$

$$\begin{aligned} -\nabla \cdot (\nu_i \nabla u) &= f \quad \text{on } \Omega_i, \\ [\![u]\!] = 0,\ [\![\nu \partial_n u]\!] &= 0 \quad \text{on } \Gamma, \end{aligned}$$

where $\nu|_{\Omega_i} := \nu_i > 0$, $i = 1, 2$ and $\boldsymbol{n}$ is the unit normal at the interface which is pointing from Ω_1 into Ω_2. The jump operator across the interface is denoted by $[\![w]\!] := (w|_{\Omega_2})|_\Gamma - (w|_{\Omega_1})|_\Gamma$.
This interface problem is intensively discussed in the literature. Babuška [8] shows that a standard finite element ansatz has low accuracy, regardless of the polynomial degree of the finite element space

$$||u - u_h||_\Omega = \mathcal{O}(h), \quad ||\nabla(u - u_h)||_\Omega = \mathcal{O}(h^{1/2}).$$

To improve the accuracy, the interface needs to be resolved within the discretization. Frei and Richter [47] presented *a locally modified finite element method* based on first-order polynomials with a first-order accuracy in the energy norm and a second order in the L^2-norm such that

$$||u - u_h||_\Omega = \mathcal{O}(h^2), \quad ||\nabla(u - u_h)||_\Omega = \mathcal{O}(h).$$

The method is based on a fixed coarse *patch mesh* consisting of quadrilaterals, which is independent of the position of the interface. The patch elements are then divided into sub-elements, such that the interface is locally resolved.
Due to the fixed background *patch mesh* this approach is particularly suitable for problems involving moving interfaces, where functions $u_h(t_{n-1})$ and $u_h(t_n)$ defined on different sub-meshes need to be integrated against each other within a time-stepping scheme [49]. Due to the implicit adaption of the finite element spaces within *the locally modified finite element method*, a costly re-meshing procedure is avoided. Similarly, *the locally modified finite element method* might be useful in shape or topology optimization problems, where problems need to be solved for different interface and boundary positions, while approaching the solution [30, 56].
The discretization is based on piecewise linear finite elements which have a natural extension to second order finite element spaces in two space dimensions. We were able to show optimal-order estimates of order two in the discrete energy norm and almost of order three (up to a logarithmic term) in the L^2-norm.
Furthermore, we study the Stokes interface problems. The motivation for considering and analysing the Stokes interface problems comes from two-phase incompressible flows. In order to guarantee the stability of mixed finite elements, the approximating spaces must satisfy the well-known discrete $inf - sup$ condition. In this thesis, we prove that the discrete $inf - sup$ constant does not depend on the mesh size and the interface position. To show the stability of the $\mathcal{P}_2 - \mathcal{P}_0$ elements, we use a macroelements technique. Moreover, we prove optimal error estimates in the L^2-norm and energy norm for Stokes interface problems. Also we present numerical examples to substantiate the analytical results.
Moreover, we investigate stationary and time dependent Stokes interface problems in which a localized force at the interface describes the effect of surface tension. The location of the interface $\Gamma(t)$ is in general unknown and is coupled to the local flow field which transports the interface. The variational formulation of these problems include a linear functional which describes the surface tension force. In this work, we use a Laplace-Beltrami approximation for the surface tension force. For temporal discretization of the time depend problems, we use semi-implicit time integration for surface tension force.
Finally, we consider fluid-structure-interaction problems, namely, a single rigid solid particle falling freely in a viscous fluid. For rigid body motion, most numerical studies

are interpreted qualitatively or compared to artificial, analytically derived solutions. The forces acting on the solid are evaluated by means of the Babuška-Miller Trick, see [11] and [83]. For time discretization of the time-dependent Stokes system we apply the implicit Euler method. Dynamically changing meshes require a projection of the discrete soultion at the old time level onto a different spatial mesh at the new time step. The mesh changes, especially when the mesh topology is also changed, may yield serious convergence problems. Dupont in [38] considered the problem for the heat equation in one dimension and has shown that the frequent and rapid mesh changes introduce an artificial dissipation to damp the numerical solution to zero, whereas the exact solution is nonvanishing. In computing incompressible flows, the solenoidal condition has to be taken into account. We use the discrete Stokes projection to evaluate the old solution on the new spatial mesh.

1.2 The organization of this thesis

After this introduction, we introduce our model problems for two-phase flows and fluid-structure problems and review known existence and uniqueness results of solutions in Chapter 2. In Chapter 3, we describe a locally modified second order finite element scheme for spatial discretization of interface problems. We analyse this scheme in detail for elliptic interface problems and show convergence results of optimal order and the findings are substantiated by means of numerical results in Chapter 4. Chapter 5 presents the main results for Stokes interface problems. To prove the discrete inf-sup condition, we use the macroelement technique. Furthermore, we use the Laplace-Beltrami approximation to handle a curvature. In Section 5.3, we use Rothe method for time depend Stokes interface problem with moving interfaces and the semi-implicit time integration for the surface tension force. We combine the discretization and Stokes projection techniques in the context of fluid-structure interaction problems in Chapter 6. The conclusion of our work and future work follows in Chapter 7.

Chapter 2: Mathematical Modelling

In this chapter, we introduce model problems of two-phase flow and fluid-structure-interaction problems and review known existence and uniqueness results of solutions.

2.1 Elliptic interface problems

2.1.1 Problem setting

We assume that the domain $\Omega \subset \mathbb{R}^2$ is divided into $\Omega = \Omega_1 \cup \Gamma \cup \Omega_2$ with an interior interface $\Gamma := \partial\Omega_1 \cap \partial\Omega_2$ and a discontinuous diffusion coefficient $\nu > 0$ across Γ and consider the equations

$$\begin{aligned} -\nabla \cdot (\nu_i \nabla u) &= f \quad \text{on } \Omega_i, \quad i = 1, 2, \\ [\![u]\!] = 0,\ [\![\nu \partial_n u]\!] &= 0 \quad \text{on } \Gamma, \\ u &= 0 \quad \text{on } \partial\Omega, \end{aligned} \tag{2.1.1}$$

where $\nu|_{\Omega_i} := \nu_i$, $i = 1, 2$. The unit normal $\boldsymbol{n}$ at the interface is pointing from Ω_1 into Ω_2. The jump operator across the interface is denoted by $[\![w]\!] := (w|_{\Omega_2})|_\Gamma - (w|_{\Omega_1})|_\Gamma$. For the notations see Figure 2.1.

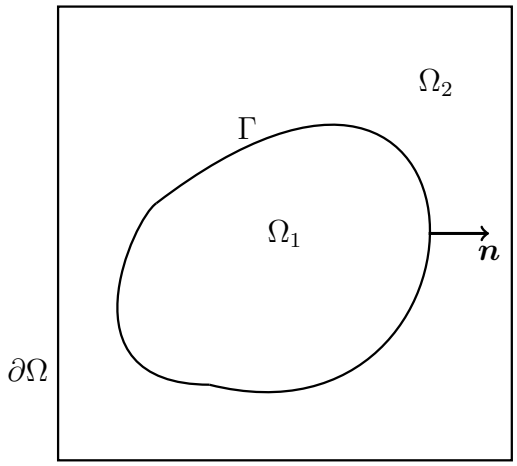

Figure 2.1: Geometry and notations of the interface problems, $\Omega = \Omega_1 \cup \Gamma \cup \Omega_2$.

The corresponding variational formulation of the problem (2.1.1) is given by

$$u \in H_0^1(\Omega): \quad \sum_{i=1}^{2}(\nu_i \nabla u, \nabla \varphi) = (f, \varphi) \quad \forall \varphi \in H_0^1(\Omega). \tag{2.1.2}$$

2.1.2 Existence and uniqueness

We define the following space

$$V := H^1(\Omega) \cap H^2(\Omega_1) \cap H^2(\Omega_2)$$

and a norm

$$||u||_V := ||u||_{H^1(\Omega)} + ||u||_{H^2(\Omega_1)} + ||u||_{H^2(\Omega_2)}, \quad \forall u \in V.$$

Theorem 2.1.1. *Let $f \in L^2(\Omega)$. Then the problem (2.1.1) has a unique solution $u \in V$ and u satisfies the a priori estimate*

$$||u||_V \leq C\,||f||_{L^2(\Omega)}.$$

Proof. The proof is given in Babuška [8] or Kellogg [70]. □

2.2 Incompressible flow problems

In this section, we consider the Stokes problem and show the existence and uniqueness results.

2.2.1 Stokes problem

Problem setting

Let $\Omega \subset \mathbb{R}^2$ be an open bounded set with a boundary $\partial\Omega$. We denote a velocity of the fluid by $\boldsymbol{u} \in \boldsymbol{C}^2(\Omega) \cap \boldsymbol{C}(\bar{\Omega})$ and a scalar function $p \in C^1(\Omega)$ as pressure, and a constant $\nu > 0$ as a diffusion coefficient. The pair $(\boldsymbol{u}, p)$ is defined in Ω and satisfies the following equation and Dirichlet or Neumann boundary conditions:

$$\begin{aligned} -\nu\Delta\boldsymbol{u} + \nabla p &= \boldsymbol{f} \quad \text{in} \quad \Omega, \\ \nabla \cdot \boldsymbol{u} &= \boldsymbol{0} \quad \text{in} \quad \Omega. \end{aligned} \tag{2.2.1}$$

For simplicity, we consider the problem (2.2.1) with homogeneous Dirichlet boundary condition on $\partial\Omega$. By denoting $\boldsymbol{V} := [H_0^1(\Omega)]^2$ and $L := L^2(\Omega)\backslash\mathbb{R}$ the corresponding variational formulation of the problem (2.2.1) is given by

$$\begin{aligned} &(\boldsymbol{u}, p) \in \boldsymbol{V} \times L: \\ &(\nu\nabla\boldsymbol{u}, \nabla\boldsymbol{\varphi})_\Omega - (p, \nabla\cdot\boldsymbol{\varphi})_\Omega + (\nabla\cdot\boldsymbol{u}, \phi)_\Omega = (\boldsymbol{f}, \boldsymbol{\varphi})_\Omega \quad \forall(\boldsymbol{\varphi}, \phi) \in \boldsymbol{V} \times L. \end{aligned} \tag{2.2.2}$$

2.2.2 Existence and uniqueness

We start with the theorem of existence and uniqueness for the velocity solution of the Stokes problem. We define the divergence free space as follows:

$$\boldsymbol{V}_{\text{div}} := \{\boldsymbol{u} \in \boldsymbol{V} : \quad (\nabla \cdot \boldsymbol{u}, \phi)_\Omega = 0 \quad \forall \phi \in L\} \subset \boldsymbol{V}$$

Then, we can restrict the variational formulation (2.2.2) to the divergence free space. We obtain

$$\boldsymbol{u} \in \boldsymbol{V}_{\text{div}} : \quad (\nu \nabla \boldsymbol{u}, \nabla \boldsymbol{\varphi})_\Omega = (\boldsymbol{f}, \boldsymbol{\varphi})_\Omega \quad \forall \boldsymbol{\varphi} \in \boldsymbol{V}_{\text{div}}. \tag{2.2.3}$$

Lemma 2.2.1. *Let $\boldsymbol{f} \in [H^{-1}(\Omega)]^2$. Then the problem (2.2.3) has a unique solution $\boldsymbol{u} \in \boldsymbol{V}_{div} \subset \boldsymbol{V}$ and $\boldsymbol{u}$ satisfies the following estimate with the constant c, it holds*

$$||\nabla \boldsymbol{u}|| \leq c\, ||f||_{-1}.$$

Proof. The vector space $\boldsymbol{V}_{\text{div}} \subset \boldsymbol{V}$ is a Hilbert space. With a scalar product defined as $(\nabla \boldsymbol{v}, \nabla \boldsymbol{v})_\Omega$. Using the Lax-Milgram theorem, it can be easily shown that there exists the unique solution $\boldsymbol{u} \in \boldsymbol{V}_{\text{div}}$ of the problem (2.2.3) (the continuity of the solution results from the Cauchy-Schwarz inequality, and the coercivity from the Poincaré inequality) and further gives the error estimate. □

Now, we show the existence and uniqueness of the pressure. For that, we will need results of next two theorems. We define the space which is the subspace of $\boldsymbol{H}^{-1}$ as follows:

$$\boldsymbol{V}^0_{\text{div}} := \{\boldsymbol{f} \in \boldsymbol{H}^{-1} : \quad \boldsymbol{f}(\boldsymbol{\varphi}) = 0 \quad \forall \boldsymbol{\varphi} \in \boldsymbol{V}_{\text{div}}\} \subset \boldsymbol{H}^{-1}$$

Theorem 2.2.2. *Let $\boldsymbol{g} \in \boldsymbol{H}^{-1}$. If and only if $\boldsymbol{g} \in \boldsymbol{V}^0_{div}$ then there exist a unique solution $p \in L$ such that*

$$-\nabla\, p = \boldsymbol{g},$$

where $-\nabla : L \longrightarrow \boldsymbol{V}^0_{div}$ is the weak gradient operator.

Proof. For the proof see, e.g. [34]. □

Theorem 2.2.3. *Let domain Ω with Lipschitz boundary be bounded. The gradient of the pressure solution $p \in L$ of the problem (2.2.2) should be from $\boldsymbol{H}^{-1}(\Omega)$ such that $\nabla\, p \in \boldsymbol{H}^{-1}(\Omega)$. Then, the next estimation holds*

$$C(\Omega)\, \|p\|_L \;\leq\; \|\nabla\, p\|_{-1},$$

here the constant C depends only on the domain Ω.

Proof. The proof of this theorem is given in the literature, e.g. [92]. □

We now determine the pressure $p \in L$ with the velocity $\boldsymbol{u} \in \boldsymbol{V}_{\text{div}} \subset \boldsymbol{V}$ as follows:

$$p \in L : \quad (p, \nabla \cdot \boldsymbol{\varphi})_\Omega = g(\boldsymbol{\varphi}),$$

here $g \in \boldsymbol{H}^{-1}$ is a linear functional defined by

$$g(\boldsymbol{\varphi}) \;=\; (\boldsymbol{f}, \boldsymbol{\varphi})_\Omega - (\nu \nabla \boldsymbol{u}, \nabla \boldsymbol{\varphi})_\Omega \quad \forall \boldsymbol{\varphi} \in \boldsymbol{V}.$$

We can reformulate this variational equation in operator notation as follows:

$$-\langle \nabla\, p, \boldsymbol{\varphi} \rangle \;=\; \langle g, \boldsymbol{\varphi} \rangle \quad \forall \boldsymbol{\varphi} \in \boldsymbol{V}.$$

The next theorem shows the equivalence with the theorem 2.2.3.

Theorem 2.2.4. *The theorem 2.2.3 is equivalent with next properties:*

- *The weak gradient operator $-\nabla : L \longrightarrow \boldsymbol{V}^0_{div}$ is an isomorphism;*
- *The inf-sup condition holds with a constant β sucht that*

$$\inf_{\phi \in L} \sup_{\boldsymbol{\varphi} \in \boldsymbol{V}} \frac{(\phi, \nabla \cdot \boldsymbol{\varphi})}{\|\phi\| \, \|\nabla \boldsymbol{\varphi}\|} \geq \beta.$$

Proof. The proof of this theorem is given in [92] or [77]. □

Lemma 2.2.5. *The following inequalities hold*

- $\|\nabla \cdot \boldsymbol{u}\| \leq \sqrt{d}\, \|\nabla\, \boldsymbol{u}\| \quad \forall \boldsymbol{u} \in [H^1(\Omega)]^d$ *$(d = 2, 3)$,*
- $\|\nabla \cdot \boldsymbol{u}\| \leq \|\nabla\, \boldsymbol{u}\| \quad \forall \boldsymbol{u} \in [H^1_0(\Omega)]^d$ *$(d = 2, 3)$.*

Proof. The proof of these inequalities follows with help of Young's inequality. For the second inequality first we use the integration by parts of the mixed terms and then Young's inequality. □

The next theorem gives us the existence and uniqueness of the Stokes problem (2.2.2).

Theorem 2.2.6. *Let the domain Ω be have a Lipschitz boundary. For every $\boldsymbol{f} \in \boldsymbol{H}^{-1}$ the problem (2.2.2) has a unique solution pair $(\boldsymbol{u}, p) \in \boldsymbol{V} \times L$. It holds*

$$\|\nabla \boldsymbol{u}\| \;+\; \beta\, \|p\| \;\leq\; c\, \|\boldsymbol{f}\|_{-1},$$

where $c > 0$ is the constant.

Proof. The existence and uniqueness of the velocity solution $\boldsymbol{u} \in \boldsymbol{V}_{\text{div}}$ is shown in Lemma 2.2.1. With Lemma 2.2.1 it holds

$$||\nabla \boldsymbol{u}|| \leq c\,||f||_{-1}.$$

The functional g defined above as

$$g(\boldsymbol{\varphi}) = (\boldsymbol{f}, \boldsymbol{\varphi}) - (\nu \nabla \boldsymbol{u}, \nabla \boldsymbol{\varphi})$$

is bound in $\boldsymbol{H}^{-1}(\Omega)$. Further, it holds that $g \in \boldsymbol{V}^0_{\text{div}}$. By the Theorem 2.2.2 there exists a unique pressure solution $p \in L$ of the equation

$$-\nabla\, p = \boldsymbol{g}.$$

By using the *inf-sup* inequality and then an a priori estimate for the velocity from Lemma 2.2.1 and Lemma 2.2.5 we get

$$\begin{aligned} \beta\,\|p\| \;&\leq\; \sup_{\boldsymbol{\varphi}\in\boldsymbol{V}} \frac{(p, \nabla\cdot\boldsymbol{\varphi})}{\|\nabla\boldsymbol{\varphi}\|} \;=\; \sup_{\boldsymbol{\varphi}\in\boldsymbol{V}} \frac{(\boldsymbol{f},\boldsymbol{\varphi}) - (\nu\nabla\boldsymbol{u}, \nabla\boldsymbol{\varphi})}{\|\nabla\boldsymbol{\varphi}\|} \\ &\leq\; \|\boldsymbol{f}\|_{-1} + \|\nabla\boldsymbol{u}\| \;\leq\; 2\,c\,\|\boldsymbol{f}\|_{-1}. \end{aligned}$$

□

Theorem 2.2.7. *Let domain Ω be a convex polygonal domain and $\boldsymbol{f} \in [L^2(\Omega)]^d$. Then the solution of the Stokes equation is bounded. It holds*

$$\|\nabla^2\boldsymbol{u}\| \;+\; \|\nabla p\| \;\leq\; \tilde{c}\|\boldsymbol{f}\|,$$

here $\tilde{c} > 0$ is the stability constant.

If $\Omega \subset \mathbb{R}^d$ is a domain with smooth C^{l+2} - boundary for $l \geq 0$ and $\boldsymbol{f} \in \boldsymbol{H}^l(\Omega)$ it holds

$$\|\boldsymbol{u}\|_{\boldsymbol{H}^{l+2}(\Omega)} \;+\; \|p\|_{\boldsymbol{H}^{l+1}(\Omega)} \;\leq\; c\|\boldsymbol{f}\|_{\boldsymbol{H}^l(\Omega)},$$

with a constant $c > 0$.

Proof. The proof of this theorem is given in the literature, e.g. [92]. □

2.3 Two-phase flow problems

In this section, we consider stationary and time dependent Stokes interface problems. A motivation for considering of this comes from two-phase incompressible flows. We analyse the *inf-sup* property for the variational Stokes interface problem in two subdomains. Here we follow the results given in the paper [79].

2.3.1 Stokes interface problem and well-posedness results

Problem setting

We present the Stokes interface problem on Lipschitz domain $\Omega \subset \mathbb{R}^2$, such that the Stokes equation in $\Omega = \Omega_1 \cup \Gamma \cup \Omega_2$ with a discontinuous coefficients $\nu_1, \nu_2 > 0$ across an interface $\Gamma := \partial\Omega_1 \cap \partial\Omega_2$ is given as

$$\begin{aligned} -\nabla \cdot (\nu_i \nabla \boldsymbol{u}) + \nabla p &= \boldsymbol{f} \quad \text{in} \quad \Omega_i, \\ \nabla \cdot \boldsymbol{u} &= \boldsymbol{0} \quad \text{in} \quad \Omega_i, \quad i = 1, 2 \\ [\![\boldsymbol{u}]\!] &= \boldsymbol{0} \quad \text{on} \quad \Gamma, \\ [\![(\nu \nabla \boldsymbol{u} - p\,\mathbb{I})\ \boldsymbol{n}]\!] &= \tau\, \mathcal{K}\, \boldsymbol{n} \quad \text{on} \quad \Gamma, \\ \boldsymbol{u} &= \boldsymbol{0} \quad \text{on} \quad \partial\Omega, \end{aligned} \tag{2.3.1}$$

where $\nu_i = 2\mu_i$, $i = 1, 2$ with the viscosity of the respective liquids μ_1 and μ_2, τ the surface tension coefficient, $\mathcal{K}$ the curvature of Γ, and $\boldsymbol{n}$ the unit normal at the interface Γ pointing from Ω_1 to Ω_2, for notations see Figure 2.1. The jump operator across the interface is denoted by $[\![w]\!] := (w|_{\Omega_2})|_\Gamma - (w|_{\Omega_1})|_\Gamma$.

Definition of the spaces and variational form

For the velocity field we use space $\boldsymbol{V} = [H_0^1]^2$ with the scalar product on $\boldsymbol{V}$ as $(\nu\nabla\cdot, \nabla\cdot)$. Then we define an induced norm for any $\boldsymbol{u} \in \boldsymbol{V}$ as follows:

$$\|\nabla \boldsymbol{u}\|_\nu := (\nu \nabla \boldsymbol{u}, \nabla \boldsymbol{u})^{\frac{1}{2}}$$

For the pressure, we define the space as follows:

$$L_\nu := \left\{ q \in L^2(\Omega) : \quad \int_\Omega \nu^{-1} q \,\mathrm{d}x = 0 \right\}.$$

The scalar product and an induced norm in L_ν are denoted by:

$$(p, q)_\nu := \int_\Omega \nu^{-1} pq \,\mathrm{d}x = \left(\nu^{-1} p, q\right) \quad \forall p, q \in L_\nu,$$

and $\|p\|_\nu := (p, p)_\nu^{\frac{1}{2}}$.

In the analysis on the product space $\boldsymbol{V} \times L_\nu$, we use the norms depending of ν such that

$$\left(\|\nabla \boldsymbol{u}\|_\nu^2 + \|p\|_\nu^2 \right)^{\frac{1}{2}}.$$

The corresponding variational formulation of the problem (2.3.1) without curvature term

given by

$$\begin{aligned} &(\boldsymbol{u}, p) \in \boldsymbol{V} \times L_\nu : \\ &(\nu \nabla \boldsymbol{u}, \nabla \boldsymbol{\varphi})_\Omega - (p, \nabla \cdot \boldsymbol{\varphi})_\Omega + (\nabla \cdot \boldsymbol{u}, \phi)_\Omega = (\boldsymbol{f}, \boldsymbol{\varphi})_\Omega \quad \forall (\boldsymbol{\varphi}, \phi) \in \boldsymbol{V} \times L_\nu. \end{aligned} \tag{2.3.2}$$

Well-posedness results

Now we show the well-posedness of the problem (2.3.2). By definition, we have ellipticity and continuity of the bilinear form $(\nu \nabla \boldsymbol{u}, \nabla \boldsymbol{u})$ in the space $\boldsymbol{V}$ with the norm $\|\boldsymbol{u}\|_\nu$. The following Lemma shows continuity of the bilinear form $(\nabla \cdot \boldsymbol{u}, p)$.

Lemma 2.3.1. *The following inequality holds*

$$|(\nabla \cdot \boldsymbol{u}, p)| \leq \|\nabla \boldsymbol{u}\|_\nu \, \|p\|_\nu \qquad \forall (\boldsymbol{u}, p) \in \boldsymbol{V} \times L_\nu.$$

Proof. The proof of these inequality is straightforward and it follows with help of Cauchy inequality and Lemma 2.2.5. In our case, the second inequality of Lemma 2.2.5 is as follows:

$$\|\nu^{\frac{1}{2}} \nabla \cdot \boldsymbol{u}\| \leq \|\nabla \boldsymbol{u}\|_\nu \qquad \forall \boldsymbol{u} \in \boldsymbol{V}.$$

□

We derive now the *inf-sup* condition to problem (2.3.2). For that, we recall the Nečas inequality from Theorem 2.2.3. It holds with $C_\Omega > 0$

$$C_\Omega \, \|p\| \;\leq\; \|\nabla p\|_{-1} := \sup_{\boldsymbol{u} \in \boldsymbol{V}} \frac{(\nabla \cdot \boldsymbol{u}, p)}{\|\nabla \boldsymbol{u}\|} \qquad \forall p \in L^2(\Omega) \backslash \mathbb{R}. \tag{2.3.3}$$

Further, we will need an equivalent form of Nečas inequality (2.3.3):
For any $p \in L^2(\Omega) \backslash \mathbb{R}$ there exist $\boldsymbol{u} \in \boldsymbol{V}$ such that

$$\|p\|^2 = (\nabla \cdot \boldsymbol{u}, p) \quad \text{and} \quad C_\Omega \, \|\nabla \boldsymbol{u}\| \leq \|p\|. \tag{2.3.4}$$

Theorem 2.3.2. *There exists a positive constant α independent of ν such that*

$$\sup_{\boldsymbol{u} \in \boldsymbol{V}} \frac{(\nabla \cdot \boldsymbol{u}, p)}{\|\nabla \boldsymbol{u}\|_\nu} \geq \alpha \, \|p\|_\nu \qquad \forall p \in L_\nu. \tag{2.3.5}$$

Proof. The proof of this theorem is given in [80]. □

2.3.2 Two-phase Stokes problem and well-posedness

Two phase Stokes problem

In this section we give a mathematical model of the time dependent Stokes interface problem. We denote a space-time domain as $\mathcal{Q}$ and define it as follows:

$$\mathcal{Q} := \{(t, \Omega(t)),\ t \in [0,T]\} \subset \mathbb{R} \times \mathbb{R}^2, \quad \Omega(t) = \Omega_1(t) \cup \Gamma(t) \cup \Omega_2(t)$$

The space-time domain is split into two space-time domains $\mathcal{Q}_1$ and $\mathcal{Q}_2$ by an interface G, such that:

$$\mathcal{Q} = \mathcal{Q}_1 \cup G \cup \mathcal{Q}_2, \quad G := \{(t, \Gamma(t)),\ t \in [0,T]\} \subset \mathbb{R} \times \mathbb{R}$$

The Figure 2.2 shows us the sketch of the domain. We define our model problem for given $\boldsymbol{u}_0$ and with $p = p(t,x)$, $\boldsymbol{u} = \boldsymbol{u}(t,x)$ as follows:

$$\begin{aligned}
\rho_i\, \partial_t \boldsymbol{u}_i - \nabla \cdot (\nu_i\, \mathbb{D}(\boldsymbol{u}_i)) + \nabla p &= \boldsymbol{f} \quad \text{in } \mathcal{Q}_i, \quad i = 1,2, \\
\nabla \cdot \boldsymbol{u}_i &= \boldsymbol{0} \quad \text{in } \mathcal{Q}_i, \quad i = 1,2, \\
[\![\boldsymbol{u}]\!] &= \boldsymbol{0} \quad \text{on} \quad \Gamma(t), \\
[\![(\nu\, \mathbb{D}(\boldsymbol{u}) - p\, \mathbb{I})\ \boldsymbol{n}]\!] &= -\tau\, \mathcal{K}\, \boldsymbol{n} \quad \text{on} \quad \Gamma(t), \\
\boldsymbol{u}_\Gamma &= \boldsymbol{u} \cdot \boldsymbol{n} \quad \text{on} \quad \Gamma(t), \\
\boldsymbol{u} &= \boldsymbol{u}_D \quad \text{on} \quad \partial\Omega(t), \\
\boldsymbol{u}(0,x) &= \boldsymbol{u}_0 \quad \text{in} \quad \Omega(0),
\end{aligned} \tag{2.3.6}$$

where the the density and viscosity, ρ_i and ν_i, $i = 1,2$, are assumed to be constant in each phase. The force term is defined as $\boldsymbol{f} = \rho_i\, \boldsymbol{g}$, where ρ_i is the density in the subdomain $\Omega_i(t)$, $i = 1,2$, and $\boldsymbol{g}$ is an external gravity force. In our case we assume that $\rho_1 = \rho_2$. $\mathbb{D}(\boldsymbol{u}) := \frac{1}{2}(\nabla \boldsymbol{u} + \nabla \boldsymbol{u}^T)$ is the symmetric gradient, τ is the surface tension coefficient, $\mathcal{K}$ is the unknown curvature of $\Gamma(t)$. In general, the location of the interface $\Gamma(t)$ is unknown and is determined by the local flow field, which transports the interface. For two immiscible fluids this transport of the interface is modeled by a kinematic interface condition by the fifth equation of (2.3.6), where $\boldsymbol{u}_\Gamma$ is the normal velocity of the interface, and $\boldsymbol{n}$ is the unit normal at the interface which is pointing from Ω_1 into Ω_2.
The jump operator across the interface is denoted by $[\![w]\!] := (w|_{\Omega_2})|_\Gamma - (w|_{\Omega_1})|_\Gamma$. To formulate problem (2.3.6) as a well-posed problem, we need to assume suitable initial and boundary conditions for $\boldsymbol{u}$ and Γ. Due to the coupling of the interface dynamics and the fluid dynamics in the two phases, this is very a komplex problem. There is a wide variety of literature on the existence of solutions and well-posedness of different formulations of this problem. In publications [36], [35], [87], and [86] on this topics the authors study quite regular solutions in Hölder spaces and deal with well-posedness locally in time existence of solutions close to equilibrium states.

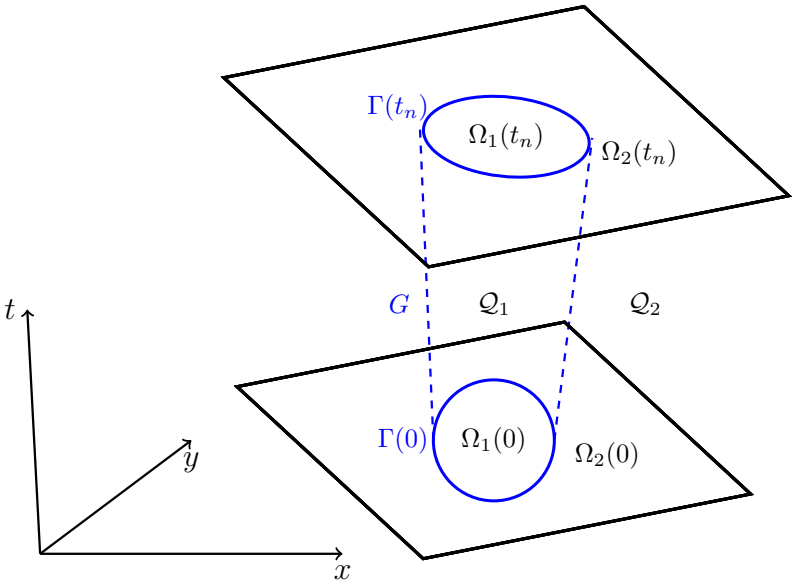

Figure 2.2: Geometry and notations of the problem (2.3.6). The space-time domain: $\mathcal{Q} = \mathcal{Q}_1 \cup G \cup \mathcal{Q}_2$. The interface $\Gamma(t)$ might move and the outer boundary $\partial\Omega(t)$ does not move in time.

Existence and uniqueness

First, we consider problem (2.3.6) with the assumption that $\nu \in L^\infty(\Omega)$. We define the operator π as the trace mapping from $H^1(Q)$ onto $H^{1/2}(\Omega)$. We assume that the initial value $\boldsymbol{u}_0$ is the trace of some divergence free function $\tilde{\boldsymbol{u}}_0$ belonging to $\boldsymbol{H}^1(\mathcal{Q})$ such that

$$\boldsymbol{u}_0 = \pi\left(\tilde{\boldsymbol{u}}_0\right), \quad \tilde{\boldsymbol{u}}_0 \in \boldsymbol{H}^1(\mathcal{Q}), \quad \operatorname{div}\left(\tilde{\boldsymbol{u}}_0\right) = 0. \tag{2.3.7}$$

The assumption (2.3.7) was introduced by Temam in [92] for obtaining the existence and uniqueness result for the Stokes problem.

Theorem 2.3.3. *Let the initial value $\boldsymbol{u}_0$ satisfy (2.3.7) for some divergence free function $\tilde{\boldsymbol{u}}_0$ and let $\nu \in L^\infty(\Omega)$ be a bounded function such that $0 < \nu_l < \nu(x) < \nu_r < \infty$. Then there exists a unique solution pair $(\boldsymbol{u}, p)$ of the time dependent Stokes problem. Moreover,*

$$\|\boldsymbol{u}\|_{H^1(\Omega)} \leq 2\, C(\Omega) \sqrt{\frac{\nu_r}{\nu_l}}\, \|\boldsymbol{u}_0\|_{H^1(\mathcal{Q})}$$

where $C(\Omega)$ is a Poincaré constant.

Proof. The proof of this theorem is given in [78]. The authors used a Schauder fixed point theorem and the concept of renormalized solutions introduced in [37]. □

Next, we follow [96] to show the well-posedness of (2.3.6). As usually done in the analysis of Stokes equations, we also restrict to a suitable subspace of divergence free

velocity fields. We introduce the spaces:

$$\boldsymbol{V}_{\mathrm{div}} := \Big\{\boldsymbol{v} \in [H_0^1(\Omega)]^d \,|\, \mathrm{div}\boldsymbol{v} = 0\Big\},\ \boldsymbol{X}_{\mathrm{div}} := L^2(I; \boldsymbol{V}_{\mathrm{div}}),$$

$$\boldsymbol{W} := \Big\{\boldsymbol{v} \in \boldsymbol{X}_{\mathrm{div}} \,|\, \rho\,\partial_t \boldsymbol{v} \in \boldsymbol{X}'_{\mathrm{div}}\Big\},\ \|\boldsymbol{v}\|^2_{\boldsymbol{W}} = \|\boldsymbol{v}\|^2_{\boldsymbol{X}_{\mathrm{div}}} + \|\rho\partial_t\,\boldsymbol{v}\|^2_{\boldsymbol{X}'_{\mathrm{div}}},$$

$$\boldsymbol{V}^0_{\mathrm{div}} := \Big\{\boldsymbol{v} \in \boldsymbol{V}_{\mathrm{div}} \,|\, \boldsymbol{v}(0) = 0\Big\}.$$

Theorem 2.3.4. *Let $a(\cdot,\cdot)$ be a continuous bilinear form on $\boldsymbol{V}_{div} \times \boldsymbol{V}_{div}$ that does not depend on time. For every $F \in \boldsymbol{X}'_{div}$ there exists a unique solution $\boldsymbol{u} \in \boldsymbol{V}^0_{div}$ such that*

$$\langle \rho\partial_t\,\boldsymbol{v}, \varphi\rangle + \int_0^T a(\boldsymbol{u}(t), \boldsymbol{\varphi}(t))dt = F(\boldsymbol{\varphi}) \quad \forall \varphi \in \boldsymbol{X}_{div}.$$

Moreover, it holds

$$\|\boldsymbol{u}\|_{\boldsymbol{V}_{div}} \leq c\,\|F\|_{\boldsymbol{X}'_{div}}$$

where c is a constant independent of F.

Proof. The proof is based on a standard Galerkin technique known in literature, e.g. [39] and is given in [96]. □

2.4 Fluid-structure interaction problems

2.4.1 Model problem

In this section we consider a linear fluid-structure interaction problem such that a time dependent Stokes equation is coupled with a solid structure equation.
Let $\Omega \in \mathbb{R}^2$ be a bounded domain and $I = [0, T]$ be a finite time interval. Further, we denote the time dependent domain as $\Omega := \Omega(t)$. We split this domain into a fluid domain and a solid domain which is described by $\Omega_s := \{(x - x_0)^2 + (y - y_0)^2 < r^2\}$ with the middle point (x_0, y_0) and a radius r of the rigid body and there is an interface between these domains, such that $\Omega = \Omega_s \cup \Gamma_I \cup \Omega_f$, see Figure 2.3.

$$\begin{aligned}
\rho_f\ \partial_t \boldsymbol{u}_f - \nabla\cdot\boldsymbol{\sigma}(\boldsymbol{u}_f, p_f) &= \mathbf{0} \quad \text{in} \quad \Omega_f,\\
\nabla\cdot\boldsymbol{u}_f &= \mathbf{0} \quad \text{in} \quad \Omega_f,\\
\frac{\mathrm{d}}{\mathrm{dt}}\boldsymbol{u}_s \cdot m_s &= \mathbf{f}_s \quad \text{in} \quad \Omega_s,\\
\boldsymbol{u}_f &= \boldsymbol{u}_s \quad \text{on} \quad \Gamma_{\mathrm{I}},\\
\boldsymbol{u}_f &= \mathbf{0} \quad \text{on} \quad \Gamma_{\mathrm{W}} \cup \Gamma_{\mathrm{B}},\\
\boldsymbol{\sigma}(\boldsymbol{u}_f, p_f)\,\boldsymbol{n} &= 0 \quad \text{on} \quad \Gamma_{\mathrm{T}},
\end{aligned} \tag{2.4.1}$$

with the stress tensor

$$\boldsymbol{\sigma}(\boldsymbol{u}_f, p_f) := \mu\nabla\boldsymbol{u}_f - p_f\mathbb{I}. \tag{2.4.2}$$

We denote by $\boldsymbol{u}_f$ the fluid and $\boldsymbol{u}_s$ the solid velocities, p_f is the fluid pressures, μ is the dynamic viscosity and ρ_f is the density of the fluid, m_s is the mass of the solid body, $\mathbf{f}_s$ is the force acting on the rigid body

$$\mathbf{f}_s = \begin{pmatrix} 0 \\ m_s\, g - V_s\, \rho_f\, g + \boldsymbol{F}_{drag} \end{pmatrix} \tag{2.4.3}$$

where $V_s = \dfrac{m_s}{\rho_s}$ is the volume of the solid body and g is a gravitational acceleration and it is given constant $g = -9,81 \frac{m}{s^2}$. The drag force $\boldsymbol{F}_{drag}$ is defined as follows

$$\boldsymbol{F}_{drag} = \int_{\Gamma_\mathrm{I}} \boldsymbol{\sigma}(\boldsymbol{u}_f, p_f)\, \boldsymbol{n}\, \boldsymbol{e}_2 \, \mathrm{d}s, \tag{2.4.4}$$

where $\boldsymbol{e}_2$ is the unit vector in vertical direction.

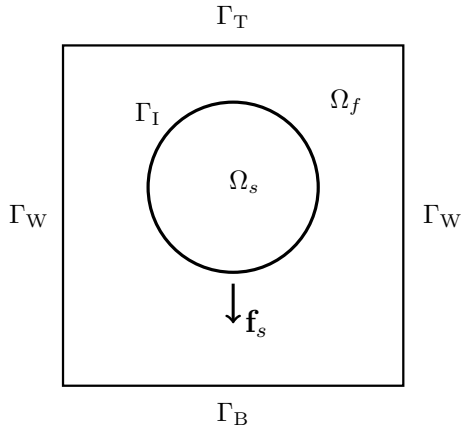

Figure 2.3: Geometry and notations of the fsi problem, $\Omega = \Omega_s \cup \Gamma_\mathrm{I} \cup \Omega_f$.

2.4.2 Existence and uniqueness results

The analysis of the well-posedness of problem (2.4.1) is nowadays an active topic in research. The existence and uniqueness of the coupled fluid-structure interaction problems are shown by Coutand and Shkoller in [32].

Theorem 2.4.1 ([32])**.** *Let $\Omega \in \mathbb{R}$ and $\Omega_s \subset \Omega$ be bounded domains of class $\boldsymbol{H}^4$, such that $\Omega = \bar{\Omega}_s \cup \Omega_f$. Let $\boldsymbol{f} \in \boldsymbol{H}^m(I, \boldsymbol{H}^3(\Omega))$, for $m = 0, 1, 2, 3$ with $\boldsymbol{f}(0), \partial_t \boldsymbol{f}(0) \in \boldsymbol{H}^4(\Omega)$. Let assume that the initial velocity satisfies $\boldsymbol{u}^0 \in \boldsymbol{H}^0_1$. Furthermore, let $\boldsymbol{u}^0_f \in \boldsymbol{H}^6(\Omega_f(t))$ with $\nabla \cdot \boldsymbol{u}^0_f = 0$, $\boldsymbol{u}^0_s \in \boldsymbol{H}^6(\Omega_s(t))$. We assume as mentioned in [32] the compatibility conditions for the data corresponding to the interface condition are hold. Then, there exists*

a time $\tilde{t} \in I$ *and a unique solution of (2.4.1) in* $\tilde{I} = [\,0, \tilde{t}\,]$ *with the following regularities:*

$$\begin{aligned} \boldsymbol{u}_f &\in \boldsymbol{H}^m\left(\tilde{I};\, \boldsymbol{H}^{4-n}(\Omega_f(t))\right), \quad m = 0,1,2,3,4 \\ \int_0^t \boldsymbol{u}_s \, dt &\in \boldsymbol{H}^m\left(\tilde{I};\, \boldsymbol{H}^{4-n}(\Omega_s(t))\right), \quad m = 0,1,2,3,4 \\ p_f &\in H^m\left(\tilde{I};\, H^{3-n}(\Omega_f(t))\right), \quad m = 0,1,2. \end{aligned}$$

In the article [68] the global existence in time was shown. The authors study in this article the coupling between the incompressible Navier-Stokes equations and a wave equation.

Chapter 3: A locally modified finite element method

The locally modified finite element method introduced by Frei and Richter in [47], [83] and [44], is a simple fitted finite element method that is able to resolve weak discontinuities in interface problems. The method is based on a fixed structured coarse mesh, which is then refined into sub-elements to resolve an interior interface. In this work, we extend the locally modified finite element method in two space dimensions to second order using an isoparametric approach in the interface elements. Therewith we need to take care that the resulting curved edges in the second order elements do not lead to degenerate sub-elements. The splitting into subelements that we propose in this work is slightly different from the one presented in [47] and leads in general to a better bound for the maximal angles within the triangles.

3.1 A locally modified first order finite element method

Let Ω_P be a fully shape-regular quadrilateral mesh of convex domain Ω with polygonal boundary. We call the elements $P \in \Omega_P$ the patches and these do not necessarily resolve the partitioning. The interface Γ may cut the patches, but $\Gamma \cap \partial\Omega = \emptyset$. In this case we make the next assumption:

Assumption 3.1.1. *1. Each patch $P \in \Omega_P$ is either cut $P \cap \Gamma \neq \emptyset$ or not cut $P \cap \Gamma = \emptyset$. If it is cut, then it is cut in exactly two points on the boundary, see Figure 3.1 (top).*

2. The interface can not cut the same edge multiple times and may not enter and leave the patch at the same edge, see Figure 3.1 (bottom).

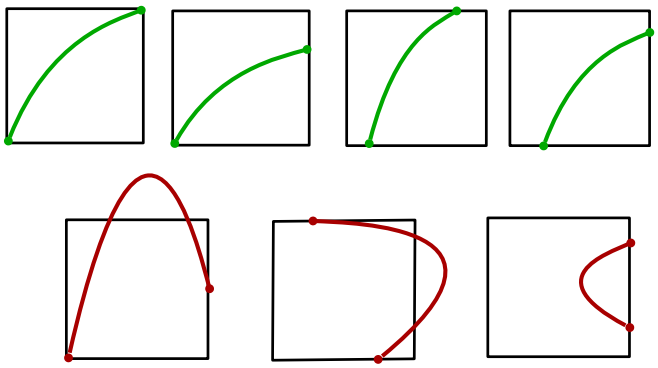

Figure 3.1: Patches with possible configurations (top), and not allowed configurations (bottom).

Given a smooth interface Γ, this assumption is fulfilled after sufficient refinement. The patch mesh Ω_P is the fixed background mesh used in the parametric finite element method described below. We will introduce a further local refinement of the mesh, denoted Ω_h where the interface is resolved. However, this refined mesh is only for illustrative purpose. The numerical realization is based on the fixed mesh Ω_P and the "refinement" is in fact only included in a parametric way within the reference map for each patch $P \in \Omega_P$.
If the interface is matched by one of the edges of the patch, then the patch is considered as not cut. We will split such patches into four quadrilaterals. If the interface cuts the patch, then the patch splits either in eight triangles or in four quadrilaterals. In both cases, the patch P is first split into four quadrilaterals, which are then possibly refined into two triangles each. This two-step procedure will simplify the following proofs.

3.1.1 Modification of the finite element space

We define the isoparametric finite element space $V_h \subset H_0^1(\Omega)$ on the triangulation Ω_P

$$V_h := \{\varphi \in C(\bar{\Omega}) \cap H_0^1(\Omega) \,|\, (\varphi \circ K_P^{-1}) \in \hat{\mathcal{Q}}_P \text{ for all } P \in \Omega_P\}, \tag{3.1.1}$$

where $K_P \in [\hat{\mathcal{Q}}_P]^2$ is the mapping between the reference patch and the patch from Ω_P such that:

$$K_P(\hat{x}_i) \,=\, x_i, \quad i = 1, ..., 9,$$

here $x_1, ..., x_9$ are the nodes of the patch, see Figure 3.2.
$\hat{\mathcal{Q}}_P$ is the piecewise first order polynomial space. The reference space $\hat{\mathcal{Q}}_P$ will depend

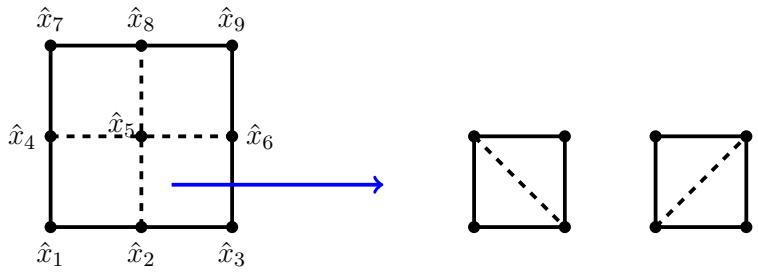

Figure 3.2: *Left*: Reference patch $\hat{P} = (0, 1)^2$ with four elements. *Right*: Splitting the patch elements into two triangles.

on whether a patch P is cut or not cut by the interface. There are two possibilities of choosing the reference element:

- For the patches which are not cut by the interface, we choose the reference space $\hat{\mathcal{Q}}_P$ as the standard space of piecewise bilinear functions. In this case, we divide the reference patch into four quadrilaterals $\hat{Q}_i$, $i = 1, ..., 4$ and define

$$\hat{\mathcal{Q}} := \{\phi \in C(\hat{P}) \,,\, \phi|_{\hat{Q}_i} \in span\{1, x, y, xy\},\ \hat{Q}_i \in \hat{P},\ i = 1, ..., 4\}.$$

- For the patches which are cut by the interface, we choose the reference space $\hat{\mathcal{Q}}_P$ as a modified space. In this case we divide the reference patch into eight triangles $\hat{T}_i$, $i = 1, ..., 8$ and define a modified space as follows

$$\hat{\mathcal{Q}}_{\text{mod}} := \{\phi \in C(\hat{P})\,,\ \phi|_{\hat{T}_i} \in span\{1, x, y\},\ \hat{T}_i \in \hat{P},\ i = 1, ..., 8\}.$$

Depending on the position of the interface Γ in the patch $\hat{P}$, we consider different types of the reference configurations by splitting the quadrilaterals into two triangles via the largest angle.
We note here, that the the functions in $\hat{\mathcal{Q}}$ and $\hat{\mathcal{Q}}_{\text{mod}}$ are all piecewise linear on the edges of the patch $\hat{P}$, such that mixing different element types does not affect the continuity of the global finite element space. We denote by $\hat{\phi}_i$, $i = 1, ..., 9$ the standard Lagrange basis of $\hat{\mathcal{Q}}$ or $\hat{\mathcal{Q}}_{\text{mod}}$ with $\hat{\phi}_i(x_j) = \delta_{ij}$. The transformation $K_{\hat{P}}$ is given as follows

$$K_{\hat{P}}(\hat{x}) = \sum_{k=1}^{9} x_i\, \hat{\phi}_i(\hat{x}).$$

In order to show optimal-order error estimates, the finite element mesh needs to fulfill a maximum angle condition in a fitted finite element method. We first analyse the maximum angles of the subtriangles for a Cartesian patch grid Ω_P. A bound for a general regular patch mesh can be obtained by using the regularity of the patch mesh.

3.1.2 Linear interface approximation and maximum angle condition

We distinguish between five different types of interface cuts, depending on how the interface intersects a patch, see Figure 3.3. We denote the relative cut positions on an edge e by $r, s \in (0, 1)$. in the case of adjacent edges, we distinguish further between the case that $r \leq \frac{1}{2}$ and $s \geq \frac{1}{2}$ and the case that one of these inequalities is violated. In all cases the patch element is split in four large quadrilaterals $Q_1, ..., Q_4$ first, which are then divided into two sub-triangles $T_1, ..., T_8$, if the interface cuts through the patch.
We consider the following five cases, see Figure 3.3

- Configuration A: The patch is cut in two opposite nodes.
- Configuration B: The patch is cut at the interior of one edge and in one node.
- Configuration C: The patch is cut at the interior of two opposite edges.
- Configuration D: The patch is cut at the interior of two adjacent edges with $r \in (0, \frac{1}{2}),\ s \in (\frac{1}{2}, 1)$.
- Configuration E: The patch is cut at the interior of two adjacent edges with
  - $r \in (0, 1)$ and $s \in (0, \frac{1}{2})$

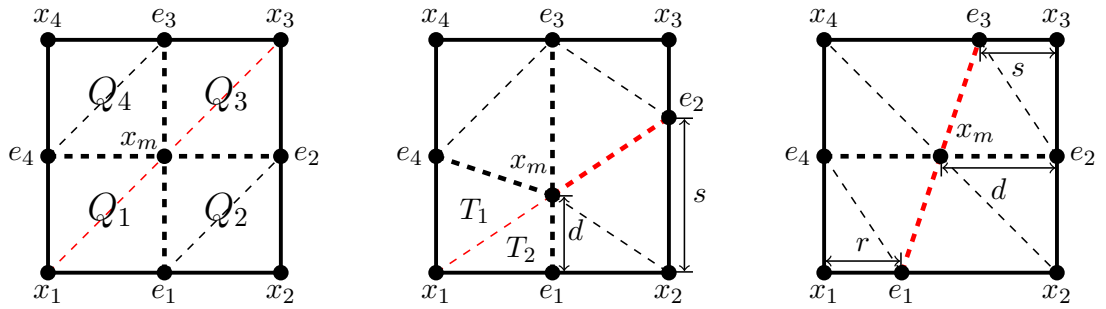

(a) Configuration A (b) Configuration B (c) Configuration C

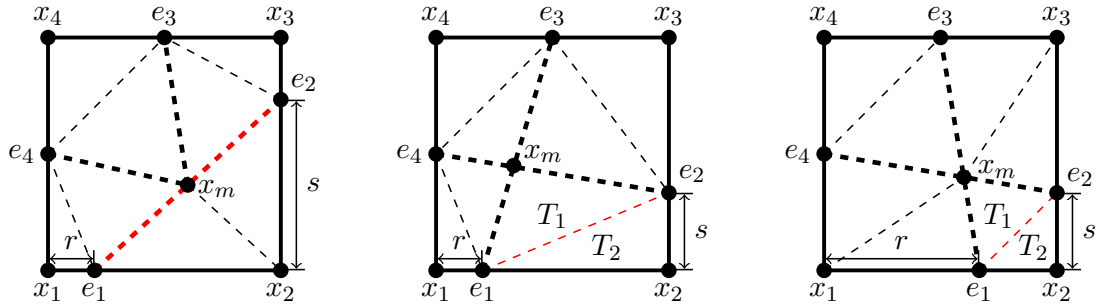

(d) Configuration D (e) Configuration E
$r \in (0,1)$, $s \in (0,1/2)$

(f) Configuration E
$r \in (1/2,1)$, $s \in (0,1)$

Figure 3.3: Different configurations and splitting into four large quadrilaterals $Q_1, ..., Q_4$. The red dashed line shows a linear approximation of the interface. Triangles T_1 and T_2 are taken from dividing the quadrilateral by the interface. In quadrilaterals that are not split by the interface, we divide in such a way into subtriangles, that the largest angle is split.

– $r \in (\frac{1}{2}, 1)$ and $s \in (0, 1)$

The subdivisions can be anisotropic with the parameters $r, s \in (0, 1)$ in the configurations B, C, D and E. These parameters describe the relative position of the intersection points with the interface on the edges. We denote by $e_i \in \mathbb{R}$, $i = 1, 2, 3, 4$, the vertices on the edges. When the interface intersects an edge, then we move the corresponding point e_i, $i = 1, ..., 4$ on the intersected edge to the point of the intersection (see Figure 3.3). If an edge is not intersected by the interface then we take e_i as midpoint of this edge. By $x_m \in \mathbb{R}^2$ we denote the midpoint of the patch, which has different positions depending on the configurations. We choose the midpoint as the intersection of the line connecting e_1 and e_3 with the line connecting e_2 and e_4 for the configurations A, C and E. For the configuration B we choose the midpoint as the intersection of the line connecting e_1 and e_3 with the line connecting x_1 and e_2. The midpoint for the configuration D is chosen as the midpoint of the line segment $\overline{e_1 e_2}$.
The patch is first divided into four quadrilaterals in all configurations, see Figure 3.3.

Depending on the configuration, we will get different types of the quadrilaterals. We note that each quadrilateral $Q_1, ..., Q_4$ in the patch has at least one right angle. The quadrilaterals in configuration A are squares. There are right-angled trapezoids in the configurations B and C. Furthermore, there are one quadrilateral with a large interior angle 180° and one quadrilateral with two large interior angles between $(90°, 180°)$ in the configuration D and E, respectively. We split all types of quadrilaterals into sub-triangles by dividing the largest interior angle of the quadrilaterals. Considering arbitrary interface positions, anisotropic elements can arise, when the relative cut position $r, s \in (0, 1)$ on an edge e tends to 0 or 1 (see Figure 3.3). We can not guarantee a minimum angle condition for the sub-triangles, but we can ensure that the maximum angles remain bounded away from 180°.

Lemma 3.1.1 (Linear approximation of the interface)**.** *All interior angles of the Cartesian patch elements shown in Figure 3.3 are bounded by* 127° *independently of the parameters* $r, s \in (0, 1)$.

Proof. First, the patch is split into four sub-quadrilaterals $Q_1, ..., Q_4$, and some of the quadrilaterals are already divided into two triangles by the interface. Other quadrilaterals which are not divided by the interface, we split in such a way that the largest angle of Q_i is divided.
We consider exemplary configurations A, B, C, D, E as shown in Figure 3.3 separately. We note that in all cases the angles at the vertices $x_i, i = 1, ..., 4$ are exactly 90°.
In configuration A we have two squares and four right-angled triangles. This case is obvious and the maximum angle of the sub-triangles is 90°.
In configuration B and C each quadrilateral $Q_i\,(i = 1, ..., 4)$ has two right angles, as the positions of e_1 and e_3, or e_2 and e_4, respectively, are fixed. In the configuration B, there are two triangles T_1, T_2 and three right-angled trapezoids in the patch, see Figure 3.3 (b). Here, T_2 is the right-angled triangle and all interior angles of the triangle T_1 less than or equal to 90°. Then we note that all right-angled trapezoids in the configurations B and C have one possible largest interior angle, see Figure 3.3 (b) and (c). In the configuration B, first, we show that the largest interior angle of all three quadrilaterals which are not divided by the interface is bounded by 135°. It holds:

$$\begin{aligned}\cos(\angle x_4 e_4 x_m) &= \frac{(x_4 - e_4) \cdot (x_m - e_4)}{|x_4 - e_4| \cdot |x_m - e_4|} = \frac{(0, 1/2) \cdot (1/2, s/2 - 1/2)}{1/2 \cdot \sqrt{(1/2)^2 + (s/2 - 1/2)^2}} \\ &= \frac{s - 1}{\sqrt{1 + (s - 1)^2}} \in \Big(-\frac{1}{\sqrt{2}}, 0 \Big)\end{aligned}$$

such that $\angle x_4 e_4 x_m \in (90°, 135°)$. By denoting $\angle e_1 x_m e_2 = \angle x_m e_2 x_3 = \alpha^B_{max}$ we obtain:

$$\begin{aligned}\cos(\alpha^B_{max}) &= \frac{(e_1 - e_3)\cdot(e_2 - x_1)}{|e_1 - e_3|\cdot|e_2 - x_1|} = \frac{(0,-1)\cdot(1,s)}{\sqrt{1+s^2}} \\ &= \frac{-s}{\sqrt{1+s^2}} \in \Big(-\frac{1}{\sqrt{2}}, 0\Big)\end{aligned}$$

such that $\alpha^B_{max} \in (90°, 135°)$.
Now, we show that the largest interior angle for all quadrilaterals of the configuration C is bounded also by 135°. It holds:

$$\cos(\alpha^C_{max}) = \pm\frac{1-s-r}{\sqrt{1+(1-s-r)^2}} \in \Big(-\frac{1}{\sqrt{2}}, \frac{1}{\sqrt{2}}\Big)$$

such that $\alpha^C_{max} \in (45°, 135°)$.
The largest interior angle for the right-angled trapezoids of the configurations B and C is $\alpha^{B,C}_{max} = 135°$. Then we split all these trapezoids into two triangles by dividing the largest interior angle which is equal to 135°.Then the largest interior angle of the sub-triangles are less than or equal to 90°. It holds:

$$\cos(\alpha_\triangle)(\text{or } \cos(\beta_\triangle)) \in \Big(0, \frac{1}{\sqrt{2}}\Big)$$

such that $\alpha_\triangle (\text{or } \beta_\triangle) \in (45°, 90°)$. We showed that all interior angles of the triangles bounded by 90° for the configurations B and C.

In the configurations D and E could have two kind of quadrilaterals as mentioned above. First, we consider the quadrilaterals in configuration D. As shown in Figure 3.3 (d), we have one quadrilateral with largest interior angle equal to 180°. In this case, we divide this angle into two angles by connecting x_m and x_2. In this case it holds:

$$\begin{aligned}\cos(\angle e_1 x_m x_2) &= \frac{(e_1 - x_m)\cdot(x_2 - x_m)}{|e_1 - x_m|\cdot|x_2 - x_m|} = \frac{((r-1),-s)\cdot((1-r),-s)}{(1-r)^2+s^2} \\ &= \frac{-(1-r)^2+s^2}{(1-r)^2+s^2} \in \Big(-\frac{3}{5}, \frac{3}{5}\Big)\end{aligned}$$

such that $\angle e_1 x_m x_2 \in (53°, 127°)$.
All other quadrilaterals could have one or two largest angles between 90° and 180°. It holds:

$$\begin{aligned}\cos(\angle x_1 e_1 e_2) &= \frac{(x_1 - e_1)\cdot(e_2 - e_1)}{|x_1 - e_1|\cdot|e_2 - e_1|} = \frac{(-r,0)\cdot(1-r,s)}{r\cdot\sqrt{s^2+(1-r)^2}} \\ &= \frac{r-1}{\sqrt{s^2+(1-r)^2}} \in \Big(-\frac{2}{\sqrt{5}}, -\frac{1}{\sqrt{5}}\Big)\end{aligned}$$

such that $\angle x_1 e_1 e_2 \in (117°, 153°)$,
and

$$\cos(\angle e_1 e_2 x_3) = \frac{(e_1 - e_2)\cdot(x_3 - e_2)}{|e_1 - e_2|\cdot|x_3 - e_2|} = \frac{(r-1,-s)\cdot(0,1-s)}{\sqrt{s^2+(1-r)^2}\cdot(1-s)}$$
$$= \frac{-s}{\sqrt{s^2+(1-r)^2}} \in \Big(-\frac{2}{\sqrt{5}}, -\frac{1}{\sqrt{5}}\Big)$$

such that $\angle e_1 e_2 x_3 \in (117°, 153°)$,
and

$$\cos(\angle x_4 1 e_4 x_m) = \frac{(x_4 - e_4)\cdot(x_m - e_4)}{|x_4 - e_4|\cdot|x_m - e_4|} = \frac{(0,1/2)\cdot((r+1)/2,(s-1)/2)}{1/4\cdot\sqrt{(r+1)^2+(s-1)^2}}$$
$$= \frac{s-1}{\sqrt{(r+1)^2+(s-1)^2}} \in \Big(-\frac{1}{\sqrt{5}}, -\frac{1}{\sqrt{10}}\Big)$$

such that $\angle x_4 e_4 x_m \in (108°, 117°)$.
Then, by dividing the largest angle of the quadrilateral we obtain two triangles and one of them is the right-angled triangle. It holds for not right-angled triangles:

$$\cos(\angle e_4 e_1 e_2) = \frac{(e_4 - e_2)\cdot(e_2 - e_1)}{|e_4 - e_2|\cdot|e_2 - e_1|} = \frac{(-r,1/2)\cdot(1-r,s)}{\sqrt{r^2+1/4}\cdot\sqrt{s^2+(1-r)^2}}$$
$$= \frac{r(r-1)+s/2}{\sqrt{r^2+1/4}\cdot\sqrt{s^2+(1-r)^2}} \in \Big(0, \frac{1}{\sqrt{2}}\Big)$$

such that $\angle e_4 e_1 e_2 \in (45°, 90°)$.

$$\cos(\angle e_1 e_2 e_3) = \frac{(e_1 - e_2)\cdot(e_3 - e_2)}{|e_1 - e_2|\cdot|e_3 - e_2|} = \frac{(r-1,-s)\cdot(-1/2,1-s)}{\sqrt{s^2+(r-1)^2}\cdot\sqrt{1/4+(1-s)^2}}$$
$$= \frac{(1-r)/2+s(s-1)}{\sqrt{s^2+(r-1)^2}\cdot\sqrt{1/4+(1-s)^2}} \in \Big(0, \frac{1}{\sqrt{2}}\Big)$$

such that $\angle e_4 e_1 e_2 \in (45°, 90°)$.
We note that the right-angled triangle $\Delta e_4 x_4 e_3$ has two equal sides and, therefore, we have $117° - 45° = 72°$ and $108° - 45° = 63°$, then $\angle e_3 e_4 x_m \in (63°, 72°)$. Our results show that all interior angles of the triangles bounded by 127° for configuration D.
Now, we consider the configuration E. In this case, we have two triangles which are divided by the interface, see Figure 3.3 (e) and (f). The triangle T_2 is a right-angled triangle. We need only to show how the largest interior angle of the triangle T_1 is bounded. It holds:

$$\cos(\angle e_1 x_m e_2) = \frac{(e_1 - e_3)\cdot(e_2 - e_4)}{|e_1 - e_3|\cdot|e_2 - e_4|} = \frac{(r-1/2,-1)\cdot(1,s-1/2)}{\sqrt{1+(r-1/2)^2}\cdot\sqrt{1+(s-1/2)^2}}$$
$$= \frac{r-s}{\sqrt{1+(r-1/2)^2}\cdot\sqrt{1+(s-1/2)^2}} \in \Big(-\frac{1}{\sqrt{5}}, \frac{4}{5}\Big)$$

such that $\angle e_1 x_m e_2 \in (36°, 117°)$.
In configuration E, the angles in $e_1, ..., e_4$ are all between 63° and 117°. It holds for example:

$$\cos(\angle x_1 e_1 e_3) = \frac{(x_1 - e_1) \cdot (e_3 - e_1)}{|x_1 - e_1| \cdot |e_3 - e_1|} = \frac{(-r, 0) \cdot (1/2 - r, 1)}{r \cdot \sqrt{1 + (1/2 - r)^2}}$$
$$= \frac{r - 1/2}{\sqrt{1 + (1/2 - r)^2}} \in \Big(-\frac{1}{\sqrt{5}}, \frac{1}{\sqrt{5}} \Big)$$

such that $\angle x_1 e_1 e_3 \in (63°, 117°)$. A bound on the angles of the quadrilaterals at x_m is therefore given by $360° - 2 \cdot 63° - 90° = 144°$. This maximum is attained for $r \to 1, s \to 0$ (cf. Figure 3.3 (f)).
The largest interior angle for quadrilaterals in configuration E is equal to 144°. By dividing the largest angle of the quadrilateral we obtain two triangles. All interior angles of all triangles are bounded by 117° in configuration E. □

Theorem 3.1.2. *We assume that the patch grid Ω_P is Cartesian. For all types of the interface cuts (see Figure 3.3), the interior angles of all subelements are bounded by* 127° *independently of the parameters $r, s \in (0, 1)$.*

Proof. By means of Lemma 3.1.1 all interior angles on the reference patch are bounded by 127°. As all cells are Cartesian, the same bound holds for the elements in Ω_P . □

Remark 3.1.1. *We have assumed for simplicity that the underlying patch mesh is fully Cartesian. This assumption can, however, easily be weakened. Allowing more general form- and shape-regular patch meshes a geometric transformation of each patch to the unit patch will give a bound $\alpha < \alpha_{\max} < 180°$ for the interior angles α (with $\alpha_{\max}$ larger than 127°).*

3.2 Extension to second order finite element method

In this section, we extend the first order approach discussed in the previous section to a second order discretization.

3.2.1 Modified finite element spaces

We define the isoparametric finite element space $V_h \subset H_0^1(\Omega)$

$$V_h := \{\varphi \in C(\Omega) \,|\, (\varphi \circ T^{-1}) \in \mathcal{P}_K^r(\hat{K}) \text{ for } K \in \mathcal{T}_h\},$$

where

$$\mathcal{P}_K^r(\hat{K}) := \begin{cases} \mathbb{Q}_r(\hat{K}), & K \text{ is a quadrilateral,} \\ \mathbb{P}_r(\hat{K}), & K \text{ is a triangle,} \end{cases}$$

and $T \in \mathcal{P}_K^r(\hat{K})$ is a transformation from the reference element $\hat{K}$ to K. The space V_h is continuous, as the restriction of a function in $\mathbb{Q}_r(\hat{K})$ to a line $e \subset \partial\hat{K}$ is in $\mathbb{P}_r(e)$.

3.2.2 Quadratic interface approximation

In this section, we define a quadratic approximation of the interface. In each of the sub-triangles obtained in the previous paragraph, we consider 6 degrees of freedom that lie on the vertices and edge midpints of the triangles (see the dots in Figure 3.4). In order

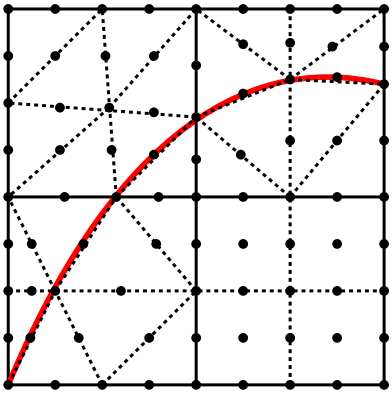

Figure 3.4: Mesh consisting of four patches, three of which are cut by the interface.

to guarantee a higher-order interface approximation those that lie on the discrete interface Γ_h need to be moved.

Lemma 3.2.1. *(Quadratic elements) All interior angles of the triangles under certain assumptions are also bounded by* $127°$ *independently of the parameters* $r, s \in (0, 1)$.

Proof. The proof of this lemma follows by the Lemma 3.1.1. For the elements with curved boundaries we consider two kinds of interfaces:

1. Second order finite elements for the interface given by first order functions. In this case, we use Lemma 3.1.1 and properties of a middle segments of the triangles. We get also easily that all interior angles of the triangles are bounded by $127°$ independently of the parameters $r, s \in (0, 1)$.

2. In the case when the interface is given by second order functions, we need to ensure that all elements are allowed in the sense of Assumption 3.1.1 (see also Figure 3.1) and that the maximum angle condition shown above remains valid.

We need to move certain points to the interface in order to obtain a second-order interface approximation, for the details see also Section 3.2.3. This is possible if the following criteria are satisfied. Otherwise, we leave them in their original positions and obtain a first-order interface approximation in the respective element. By $\alpha_\triangle$ we denote the largest angle in a triangle.

In the first step, we move the midpoint of the patch. If this is possible, we shift the other corresponding points in a second step (if possible). We use the following criteria for each configuration.

First step: Move the midpoints

- **Configuration** A: the midpoint of the patch can be moved along the normal line $\boldsymbol{n}$ (see Figure 3.3a) if $\alpha_{\triangle} \leq \alpha_{max} < 180°$.
- **Configuration** B: the midpoint of the patch can be moved along the line segment e_1e_3, if the relative length $d = \frac{|e_1 - x_m|}{|e_2 - e_1|}$ of the line e_1x_m (see Figure 3.3b) satisfies $\epsilon < d < 1 - \epsilon$ and $\alpha_{\triangle} \leq \alpha_{max} < 180°$.
- **Configuration** C: the midpoint of the patch can be moved along the line segment e_2e_4, if the parameter d (see Figure 3.3c) satisfies $\epsilon < d < 1 - \epsilon$.
- **Configuration** D: the midpoint of the patch can be moved along the normal line $\boldsymbol{n}$ (see Figure 3.3d) if $\alpha_{\triangle} \leq \alpha_{max} < 180°$.
- **Configuration** E: in this configuration we do not need to move the midpoint of the patch (see Figures 3.3e), and 3.3f).

Second step: Move other points

- In the second step, we investigate the other two points that need to be moved in order to obtain a second-order interface approximation. These are the points between the midpoint of the patch and the points where exterior edges are intersected. In all configurations, we obtain triangles with one curved edge. It can happen that this curved edge intersects other edges of the element T. Thus, we shift the corresponding points along the normal line to the interface, if and only if the curved edge of the triangle does not cut any other edges and $\alpha_{\triangle} \leq \alpha_{max} < 180°$.

  In certain "pathological" situations we can not guarantee that the angle conditions imposed above are fulfilled. This is due to the fact that the curved edges that correspond to a quadratic interface approximation might intersect other edges, see Figure 3.5 for an example.
  In this case, we use a linear approximation of the interface in the affected patch. We will see in the numerical examples below that this happens rarely. Moreover, it is reasonable to assume that the maximum number of such patches remains bounded under refinement independently of h. We give a heuristic argument for this assumption. Let us consider the situation sketched in Figure 3.5. In the configuration on the right the quadratic interface approximation lies slightly outside of the triangle. On the other hand, the linear approximation of the interface (i.e. the lower edge) will

never leave the patch by definition. The maximum distance between a linear and a quadratic interface approximation is bounded by $\mathcal{O}(h_P^2)$. In relation to the patch size $\mathcal{O}(h_P)$ this means that -considering arbitrary interface positions- the probability that the quadratic interface approximation leaves the patch is bounded by $\mathcal{O}(h_P)$. The number of interface patches, on the other hand, grows like $\mathcal{O}(h_P^{-1})$. Hence it is reasonable to assume that the number of affected patches behaves like $\mathcal{O}(1)$ for $h_P \to 0$. We will denote the maximum number of patches with a linear interface approximation by n_l.

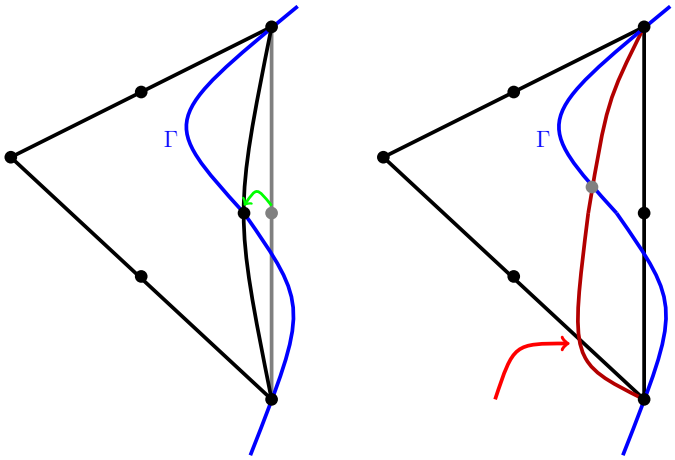

Figure 3.5: The interface Γ needs to be approximated quadratically on all triangles. To achieve this, the midpoint of the edge that corresponds to the interface is pulled onto the curve. *Left*: This is a valid configuration where a quadratic approximation is possible. *Right*: In some configurations a fully quadratic interface approximation would result in a degenerate element with an interface that is leaving triangle (see the mark on the bottom edge). Such triangles are approximated linearly, which results in $n_l > 0$.

□

3.2.3 Implementation

The locally modified finite element method is based on a patch-wise parametric approach. Let Ω_h be the triangulation. We denote by $P \in \Omega_h$ the patches, which are quadrilaterals with 25 degrees of freedom. Depending on the location of the interface, we have two kinds of patches:

- If the patch is not cut by the interface, then the patch is split into four quadrilaterals $Q_1, \ldots, Q_4$. In this case we take the standard space of piecewise biquadratic functions as follows:

$$\hat{\mathcal{Q}} := \{\phi \in C(\hat{P}),\ \phi|_{\hat{Q}_i} \in span\{1, x, y, x^2, xy, y^2, xy^2, x^2y, x^2y^2\},\ i = 1, ..., 4\},$$

where $\hat{P}$ is the reference patch on the unit square $(0,1)^2$ consisting of the four quadrilaterals $\hat{Q}_1, ..., \hat{Q}_4$.

- If the patch is cut by the interface, then the patch is split into eight triangles $T_1, \ ... \ , T_8$. Here we define the space of piecewise quadratic functions as follows:

$$\hat{\mathcal{Q}}_{mod} := \{\phi \in C(\hat{P}) \, , \, \phi|_{\hat{T}_i} \in span\{1, x, y, x^2, xy, y^2\}, \ i = 1, ..., 8\},$$

where the reference patch $\hat{P}$ consists of triangles $\hat{T}_1, ..., \hat{T}_8$.

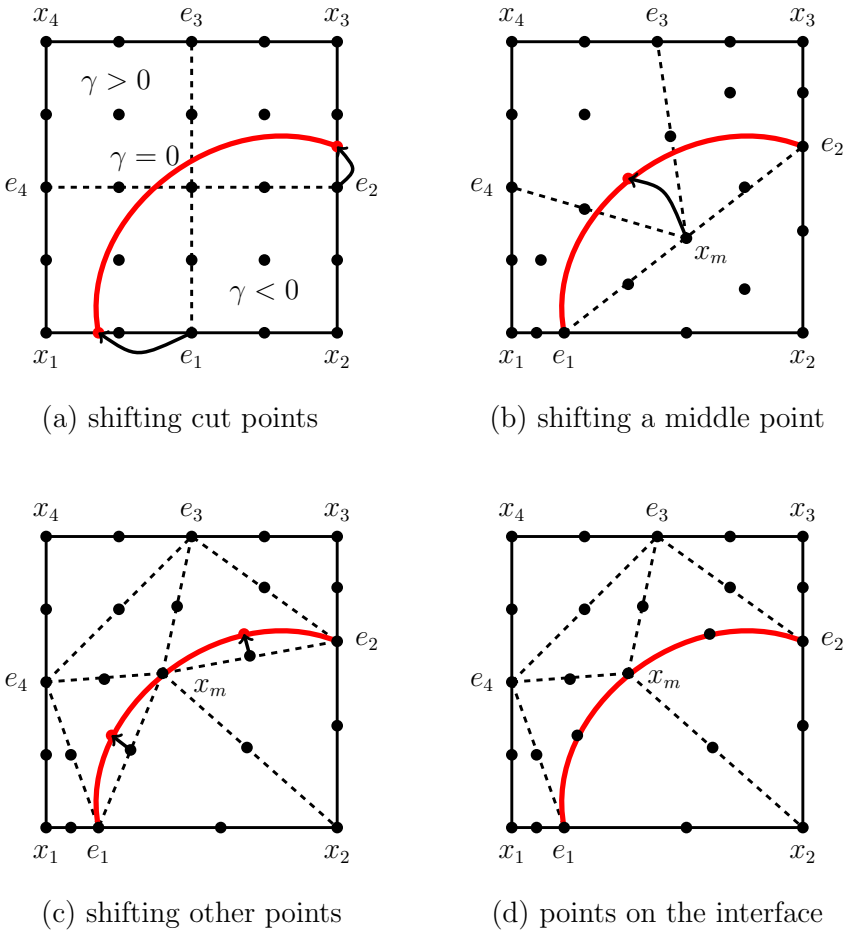

(a) shifting cut points

(b) shifting a middle point

(c) shifting other points

(d) points on the interface

Figure 3.6: Rearrangement of the Lagrangian points on the interface.

In both cases, we have locally 25 basis functions in each patch (see Figure 3.6)

$$\mathcal{Q}(P) := span\{\phi_i\}, \ \ \phi_i := \hat{\phi}_i \circ \hat{T}_P^{-1}, \ \ i = 1, ..., 25,$$

where $\hat{T}_P$ is the reference patch map, which is defined in an isoparametric way as follows

$$\hat{T}_P(\hat{x}) := \sum_{j=1}^{25} x_j \, \hat{\phi}_j.$$

Definining the patch type and movement of mesh nodes

We assume that the interface is given as zero set of an implicit level-set function $\gamma(x)$

$$\gamma(x) = 0 \qquad \Leftrightarrow \qquad x \in \Gamma.$$

The patch type and the edges that are cut can then be easily determined by computing $\gamma(x_i)$ for the exterior vertices $x_1, ..., x_4$, see Figure 3.6. An edge e is cut, if $\gamma(x_1) \cdot \gamma(x_2) < 0$ for its two end points x_1, x_2. The intersection of the interface with the edge can the be found by applying locally a Newton's method to find the zero r of

$$\gamma\Big(x_1 + r(x_2 - x_1)\Big) = 0, \tag{3.2.1}$$

see Figure 3.6 (a). The edge midpoints e_1 and e_2 will be moved to the respective position $x_1 + r(x_2 - x_1)$. Next, we define a preliminary coordinate for the midpoint of the patch x_m as the midpoint of a segment e_1e_2, see Figure 3.6 (b). For a second-order interface approximation, it is necessary to move x_m to the interface Γ in the configurations A to D. We use again Newton's method to move x_m to the interface along a normal line, see Figure 3.6 (c). Second, we also move the midpoints of the segments e_1x_m and x_me_2 analogously, see Figure 3.6 (d). Finally, we need to specify criteria to ensure that the resulting sub-triangles with curved boundaries fulfill a maximum angle condition. For the details see the proof of Lemma 3.2.3.

Remark 3.2.1. *A disadvantage of the modified second order finite element method described above is that the stiffness matrix can be ill-conditioned for certain anisotropies. In particular, the condition number depends not only on the mesh size, but also on how the interface intersects the triangulation (e.g., $s, r \to 0$). In section 4.3 we consider two examples, where the condition number of the stiffness matrix is not bounded. For this reason a hierarchical finite element basis was introduced in [47] for the linear finite elements and it was shown that the stiffness matrix satisfies the usual bound $\mathcal{O}(h_P^{-2})$ with a constant that does not depend on the position of the interface. We extend this approach to the second order finite element method in Chapter 4. We will see that the condition number for a scaled hierarchical basis is reduced significantly, although we can not guarantee the optimal bound for the method presented here.*

Chapter 4: Discretization of elliptic interface problems

In this chapter, we study the interface Laplace equation (2.1.1). We consider the model problem

$$\begin{aligned} -\nabla \cdot (\nu_i \nabla u) &= f \quad \text{on } \Omega_i, \quad i = 1, 2, \\ [\![u]\!] = 0,\ [\![\nu \partial_n u]\!] &= 0 \quad \text{on } \Gamma, \\ u &= 0 \quad \text{on } \partial\Omega, \end{aligned} \tag{4.0.1}$$

For the discretization of this problem we use *the locally modified second order finite element method* introduced in Chapter 3. We prove optimal a priori error estimates in the L^2-norm and in the discrete energy norm. Finally, we present numerical examples to substantiate the theoretical findings.

Literature review

The *locally modified finite element method* has been used by the authors and co-workers [44, 50–52], and by Langer & Yang [72] for fluid-structure interaction (FSI) problems, including the transition from FSI to solid-solid contact [27, 28, 48]. Holm et al. [65] and Gangl & Langer [56] used a corresponding approach based on triangular patches, the latter work being motivated by a topology optimization problem. A pressure stabilization technique for flow problems has been developed in [45] and a suitable (second-order) time discretization scheme in [49]. Details of the implementation in deal.ii and the corresponding source code have been published in [53, 54]. Extensions to three space dimensions have been developed by Langer & Yang [72], where hexahedral coarse cells are divided into sub-elements consisting of hexahedra and tetrahedra, and by Höllbacher & Wittum, where a coarse mesh consisting of tetrahedra is sub-divided into hexahedrons, prisms and pyramids [66, 95].
Alternative approaches are unfitted methods, where the mesh is fixed and does not resolve the interface. Prominent examples are the extended finite element method (XFEM [76]), the generalized finite element (GFEM [10]) and Cut Finite Elements [29, 61] including unfitted DG methods [59]. For Cut Finite Elements a higher order unfitted finite element method has been developed and analyzed by Lehrenfeld and Reusken (see [73–75]).
For further *fitted* finite element methods, we refer to [9,15,25,42,97]. Some works are similar to the *locally modified finite element methods* in the sense that only mesh elements close to the interface are altered [23, 100]. A *fitted* method with a higher order approximation has been developed by Fang [41].

4.1 Discrete variational formulation

We use the space V_h defined as in Chapter 3

$$V_h := \{\varphi \in C(\Omega) \,|\, (\varphi \circ T^{-1}) \in \mathcal{P}_K^r(\hat{K}) \text{ for } K \in \Omega_h\},$$

where the map T resolves the interface with order r in all but n_l elements, where the approximation is only linear. The polynomial order of the trial functions $\varphi \circ T^{-1}$ is r independent of the interface approximation. We consider a C^3- parameterized interface Γ, which is not matched by the triangulation Ω_h. The triangulation induces a discrete interface Γ_h, which is a quadratic and in some special cases a linear approximation to Γ. The discrete interface splits the triangulation in two sub-domains Ω_h^1 and Ω_h^2, such that each triangle $K \in \Omega_h$ is either completely included in Ω_h^1 or in Ω_h^2.
We consider the following discrete variational formulation: *Find $u_h \in V_h$ such that*

$$a_h(u_h, \phi_h) = (f_h, \phi_h)_\Omega \quad \forall \phi_h \in V_h. \tag{4.1.1}$$

By reason of $\Omega_i \neq \Omega_h^i$, we set $f_h|_{\Omega_h^i} := f_i, i = 1, 2$. We note that f_i is a smooth extension of $f|_{\Omega_i}$ to Ω_h^i. The bilinear form is given by

$$a_h(u_h, \phi_h) := (\nu_h \nabla u_h, \nabla \phi_h)_\Omega,$$

where ν_h is defined by

$$\nu_h = \begin{cases} \nu_1, & x \in \Omega_h^1 \\ \nu_2, & x \in \Omega_h^2. \end{cases}$$

4.2 A priori error analysis

Let h_P be the maximum size of a patch element $P \in \Omega_P$ of the regular patch grid. We will denote the mismatch between Ω_h^i and Ω^i by S_h^i, $i = 1, 2$ (see Figure 4.1)

$$S_h^1 := \Omega_h^1 \setminus \Omega_1 = \Omega_2 \setminus \Omega_h^2,$$
$$S_h^2 := \Omega_h^2 \setminus \Omega_2 = \Omega_1 \setminus \Omega_h^1.$$

Moreover, we denote the set of elements $T \in \Omega_h$ that contain parts of S_h^i by

$$S_T^i := \{T \in \Omega_h \,|\, T \cap S_h^i \neq 0\}, \qquad S_T := S_T^1 \cup S_T^2.$$

Further, we split S_h^i into linear parts $S_{h,\text{lin}}^i$ with a linear approximation of the interface and quadratic parts $S_{h,\text{qu}}^i$ with a quadratic approximation of the interface. Similarly, we split

the set of triangles S_T^i that are affected by the interface into parts $S_{T,\text{lin}}^i$ if the triangle (patch) contains a linear approximation of the interface and $S_{T,\text{qu}}^i$ if the approximation is fully quadratic. The union of $S_{T,\text{qu}}^1$ and $S_{T,\text{qu}}^2$ is denoted by $S_{T,\text{qu}}$ and analogously for $S_{T,\text{lin}}$.

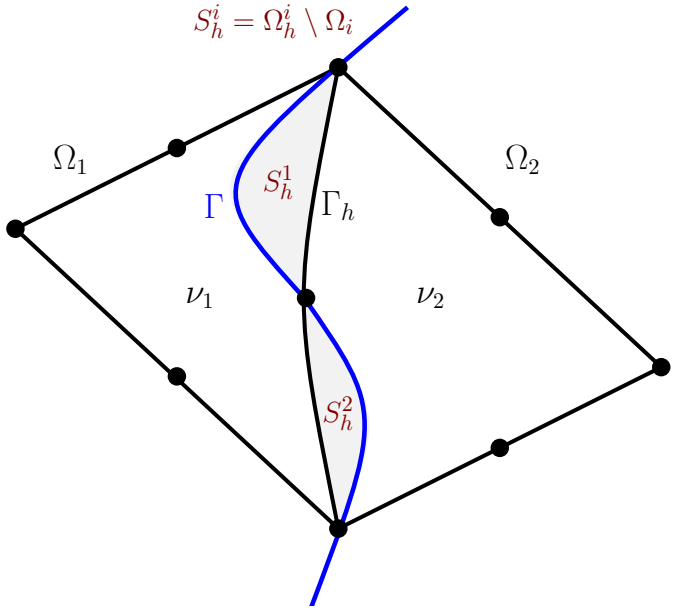

Figure 4.1: Mismatch S_h^i between Ω^i and Ω_h^i, $i = 1, 2$ at two elements along the curved interface.

4.2.1 Auxiliary estimates

First, we need to prove some auxiliary estimates in order to control the mismatch between continuous and discrete bilinear forms. For that we need the following Sobolev imbedding estimation for $2 \leq p < \infty$

$$\|u\|_{L^p(\Omega)} \leq c p^{\frac{1}{2}} \|u\|_{H^1(\Omega)}, \tag{4.2.1}$$

which is valid with a constant c independent of p, see [91]. We start with the following technical result.

Lemma 4.2.1. *Let $\alpha \in \mathbb{N}$, $h \in \mathbb{R}_+$ and $J(p) := \sqrt{p}\, h^{-\frac{\alpha}{p}}$. It holds that*

$$\min_{p \in [2,\infty]} J(p) \leq c\, |\ln(h)|^{\frac{1}{2}}.$$

Proof. We start with the necessary condition for a local minimum: $J'(p) = 0$. It holds:

$$\begin{aligned} J'(p) = \frac{1}{2\sqrt{p}}\, h^{-\frac{\alpha}{p}} + h^{-\frac{\alpha}{p}}\, \ln(h)\, \frac{\alpha}{p\sqrt{p}} &= h^{-\frac{\alpha}{p}} p^{-\frac{1}{2}} \left(\frac{1}{2} + \ln(h)\, \frac{\alpha}{p} \right) \\ \frac{1}{2} + \ln(h)\, \frac{\alpha}{p} &= 0 \\ p &= -2\alpha \ln(h). \end{aligned}$$

The minimum value is

$$J(-2\alpha \ln(h)) = \sqrt{-2\alpha \ln(h)}\; h^{-\frac{\alpha}{(-2\alpha \ln(h))}} = \sqrt{2\alpha\, e}\, |\ln(h)|^{\frac{1}{2}}.$$

The fact that $\lim_{p\to\infty} J(p) = \infty$ and $J(2) > J(-2\alpha \ln(h))$ show that the local minimum is in fact a global one. □

For the estimation of the mismatch between continuous and discrete bilinear forms, we need to prove the following geometry approximation lemma.

Lemma 4.2.2. *Let $T \in S_T$ and let s be the local approximation order of the interface, i.e.*

$$dist\,(\Gamma_h \cap T; \Gamma \cap T) \leq c h_P^{s+1}. \tag{4.2.2}$$

If the number of elements with a linear interface approximation is bounded by n_l, it holds for the areas of the regions $S_{h,lin}$ and $S_{h,qu}$ that

$$|S_{h,lin}| \leq n_l h_P^3, \quad |S_{h,qu}| \leq h_P^3. \tag{4.2.3}$$

For $u \in H^1(\Omega_1 \cup \Omega_2)$ and $\phi_h \in \mathcal{V}_h$ we have the bounds

$$\|\nabla \phi_h\|_{S_h \cap T} \leq c h_P^{\frac{s}{2}} \|\nabla \phi_h\|_T \tag{4.2.4}$$

$$\|u\|_{S_h \cap T} \leq c h_P^{\frac{s+1}{2}} \|u\|_{\Gamma \cap T} + c h_P^{s+1} \|\nabla u\|_{S_h \cap T}. \tag{4.2.5}$$

Moreover, we have for $u \in H^1(\Omega_1 \cup \Omega_2)$ and $v \in H^2(\Omega_1 \cup \Omega_2)$

$$\|u\|_{S_{h,lin}} \leq c h_P \|u\|_{H^1(\Omega_1 \cup \Omega_2)}, \qquad \|u\|_{S_{h,qu}} \leq c h_P^{\frac{3}{2}} \|u\|_{H^1(\Omega_1 \cup \Omega_2)} \tag{4.2.6}$$

and

$$\|u\|_{S_{h,lin}} \leq c n_l^{\frac{1}{2}} h_P^{\frac{3}{2}} |\ln(h)|^{1/2} \|u\|_{H^1(\Omega_1 \cup \Omega_2)}, \qquad \|v\|_{S_{h,lin}} \leq c n_l^{\frac{1}{2}} h_P^{\frac{3}{2}} \|v\|_{H^2(\Omega_1 \cup \Omega_2)}. \tag{4.2.7}$$

For functions $u \in H_0^1(\Omega)$ the H^1-norm on the right-hand side of (4.2.6) and (4.2.7) can be replaced by the H^1-seminorm.

Proof. Estimates (4.2.3)-(4.2.5) have been shown in [83]. (4.2.3) follows from (4.2.2) and simple geometric arguments. For (4.2.4) and (4.2.5) a Poincaré-type estimate is used, see [83, Lemma 4.34]

$$\|u\|^2_{S_h\cap T} \leq ch_P^{s+1}\|u\|^2_{\Gamma_h\cap T} + ch_P^{2s+2}\|\nabla u\|^2_{S_h\cap T}. \tag{4.2.8}$$

Summation over all elements in $S_{T,\text{lin}}$ and $S_{T,\text{qu}}$, respectively, and a global trace inequality for the interface terms yields (4.2.6). To show (4.2.7), we use a Hölder inequality for $p \in [2,\infty]$

$$\|u\|_{S_{h,lin}} \leq |S_{h,lin}|^{\frac{1}{2}-\frac{1}{p}}\|u\|_{L^p(S_{h,lin})}. \tag{4.2.9}$$

Due to $|S_{h,lin}| \leq cn_l h_P^3$ and the Sobolev imbedding (4.2.1) for $\Omega = \Omega_i$ we have for arbitrary $p \in [2,\infty)$

$$\|u\|_{S_{h,lin}} \leq cp^{\frac{1}{2}} n_l^{\frac{1}{2}} h_P^{\frac{3}{2}-\frac{3}{p}}\|u\|_{H^1(\Omega_1\cup\Omega_2)}. \tag{4.2.10}$$

Using Lemma 4.2.1, we obtain the first estimate in (4.2.7).
If $v \in H^2(\Omega_1 \cup \Omega_2)$ we can use (4.2.9) for $p = \infty$ due to the Sobolev imbedding $H^2(\Omega_i) \subset L^\infty(\Omega_i)$ and we obtain

$$\|u\|_{S_{h,lin}} \leq cn_l^{\frac{1}{2}} h_P^{\frac{3}{2}}\|u\|_{H^2(\Omega_1\cup\Omega_2)}. \tag{4.2.11}$$

Finally, the norms on the right-hand side can be substituted by the H^1-seminorm for $u \in H^1_0(\Omega)$ by means of the Poincaré inequality. □

The continuous solution u is regular in Ω_i, $i = 1, 2$, but its normal derivative has a jump across the interface. Discrete functions have non-regularities only at the boundaries of cells ∂T. This means that a discrete function can only resemble a similar discontinuity across the discrete interface. Therefore, we need some technicalities in the estimates.

We consider a map $\pi : H^3(\Omega_1 \cup \Omega_2) \to H^3(\Omega_h^1 \cup \Omega_h^2)$. Let $u \in H^3(\Omega_1 \cup \Omega_2)$ and $u_i := u|_{\Omega_i} \in H^3(\Omega_i)$. Due to smooth interface Γ we can use smooth extensions $\tilde{u}_i \in H^3(\Omega)$ $(i = 1, 2)$ to the full domain Ω, e.g. see the textbook of Wloka [99], such that

$$\|\tilde{u}_i - u\|_{H^m(\Omega_i)} = 0, \quad \|\tilde{u}_i\|_{H^m(\Omega)} \leq C\|u\|_{H^m(\Omega_i)}, \quad i = 1, 2, \quad m = 2, 3, \tag{4.2.12}$$

By using these extensions we define a function $\pi u \in H^3(\Omega_h^1 \cup \Omega_h^2)$:

$$\pi u = \begin{cases} \tilde{u}_1, & x \in \Omega_h^1, \\ \tilde{u}_2, & x \in \Omega_h^2. \end{cases} \tag{4.2.13}$$

We note that that πu can be discontinuous across Γ_h.

Lemma 4.2.3. *Let $u \in H^3(\Omega_1 \cup \Omega_2)$ and $\pi u \in H^3(\Omega_h^1 \cup \Omega_h^2)$ the function defined by (4.2.13). It holds that*

$$\|\nabla(u - \pi u)\|_\Omega \leq c h_P \left(n_l^{1/2} + 1\right) \|u\|_{H^2(\Omega_1 \cup \Omega_2)} \tag{4.2.14}$$

$$\|\nabla(u - \pi u)\|_\Omega \leq c h_P^{3/2} \left(n_l^{1/2} + 1\right) \|u\|_{H^3(\Omega_1 \cup \Omega_2)}. \tag{4.2.15}$$

where n_l is the maximum number of elements with a linear interface approximation.

Proof. In the small strip S_h around the interface u and πu are defined differently. Using the Sobolev embedding $H^3(\Omega_i) \subset W^{1,\infty}(\Omega_i)$ and the continuity of the extensions (4.2.12) it holds for $u \in H^3(\Omega_i)$:

$$\begin{aligned}\|\nabla(u - \pi u)\|_\Omega = \|\nabla(u - \pi u)\|_{S_h} &\leq |S_h|^{\frac{1}{2}} \left(\|\nabla u\|_{L^\infty(\Omega)} + \|\nabla \pi u\|_{L^\infty(\Omega)}\right) \\ &\leq c|S_h|^{\frac{1}{2}} \|u\|_{H^3(\Omega_1 \cup \Omega_2)}.\end{aligned}$$

Then by applying (4.2.3) we get (4.2.15).

To show (4.2.14), we note that $u - \pi u$ vanishes in cells $T \in \mathcal{T}_h \setminus S_T$. Thus, let $T \in S_T$ and let $s \in \{1, 2\}$ be the local approximation order of the interface in T. We use (4.2.5) and the fact that $s \geq 1$ to get

$$\begin{aligned}\|\nabla(u - \pi u)\|_T = \|\nabla(u - \pi u)\|_{S_h \cap T} &\leq c h_P^{\frac{1+s}{2}} \|\nabla(u - \pi u)\|_{\Gamma \cap T} + c h_P^{1+s} \|\nabla^2(u - \pi u)\|_{S_h \cap T} \\ &\leq c h_P \left(\|\nabla u\|_{\Gamma \cap T} + \|\nabla \pi u\|_{\Gamma \cap T}\right) + c h_P^2 \left(\|\nabla^2 u\|_{S_h \cap T} + \|\nabla^2 \pi u\|_{S_h \cap T}\right),\end{aligned}$$

where the derivatives on Γ need to be seen from S_h.

After summation over all cells $T \in \Omega_h$ a global trace inequality and (4.2.12) yield

$$\|\nabla(u - \pi u)\|_\Omega \leq c h_P \left(\|u\|_{H^2(\Omega_1 \cup \Omega_2)} + \|\pi u\|_{H^2(\Omega_1 \cup \Omega_2)}\right) \leq c h_P \|u\|_{H^2(\Omega_1 \cup \Omega_2)}.$$

□

4.2.2 Interpolation

In this subsection, we will derive interpolation estimates for a Lagrangian interpolant I_h. Let $\mathcal{L}_T$ be the set of Lagrange points that belong to a cell $T \in \Omega_h$. In the case of a linear interface approximation, it can happen that some of these lie on Γ_h, but not on Γ. This means that there are elements with Lagrange points $x_i \in \mathcal{L}_T$, that lie in different sub-domains Ω_1 and Ω_2, see Figure 4.2. Defining the interpolant as $I_h u = \sum_{i \in \mathcal{L}_T} u(x_i)$ would lead to a poor approximation order ($\mathcal{O}(h_P)$ in the H^1-norm), due to the discontinuity of ∇u across Γ. Each such point x_i lies, however, on a line between two points x_1^* and

x_2^* on Γ. We use a linear interpolation of the values $u(x_1^*)$ and $u(x_2^*)$ in order to define $I_h u(x_i) := \frac{1}{2}(u(x_1^*) + u(x_2^*))$, see also [44] and Fig. 4.2 (right). We have the following

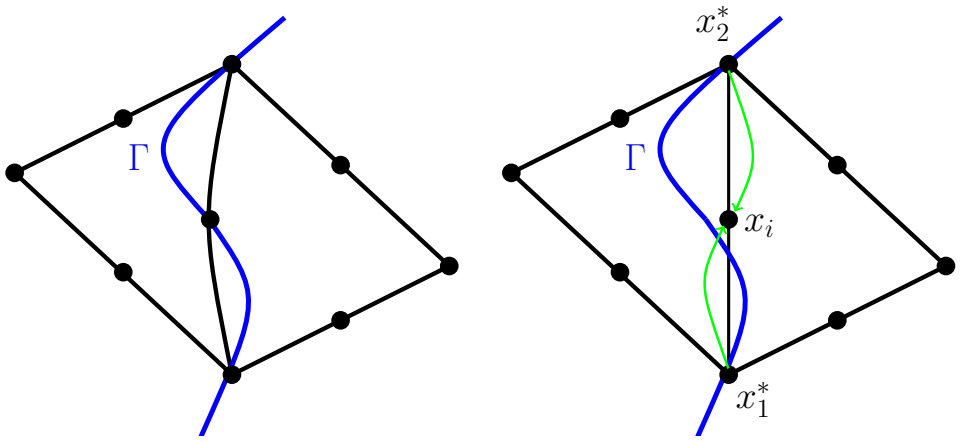

Figure 4.2: Interpolation operator at the interface Γ. Left: For second order interface approximations we use the standard nodal interpolation for the interface. Right: For linear interface approximations we replace the node x_i in the middle of the interface edge by the mean of the two adjacent corner nodes x_1^* and x_2^*.

approximation properties for this modified Lagrangian interpolant.

Lemma 4.2.4 (Interpolation)**.** *Let $u \in \mathcal{U} := \left[H_0^1(\Omega) \cap H^3(\Omega_1 \cup \Omega_2)\right]$ and $\tilde{u} = \pi u \in H^3(\Omega_h^1 \cup \Omega_h^2)$ the function resulting from the map π defined in* (4.2.13)*. Moreover, we assume that Γ is a smooth interface with C^3-parametrization and that the interface is approximated with second order in all elements $T \in \Omega_h$, except for at most n_l elements, where the interface approximation is linear. It holds for the Lagrangian interpolation operator $I_h : \mathcal{U} \to V_h$ that*

$$\|\nabla^m(u - I_h u)\|_\Omega \leq c h_P^{2-m} \|u\|_{H^2(\Omega_1 \cup \Omega_2)}, \quad m = 0, 1 \tag{4.2.16}$$

$$\|\nabla(\tilde{u} - I_h u)\|_\Omega \leq \left(c_l n_l^{1/2} |\ln(h)|^{1/2} + c_q\right) h_P^2 \|u\|_{H^3(\Omega_1 \cup \Omega_2)}. \tag{4.2.17}$$

where c_l and c_q are generic constants that correspond to patches with a linear and a quadratic interface approximation, respectively. For $u \in W^{2,\infty}(\Omega_1 \cup \Omega_2)$ we have further

$$\|\nabla(\tilde{u} - I_h u)\|_\Omega \leq \left(c_l n_l^{1/2} + c_q\right) h_P^2 \|u\|_{W^{2,\infty}(\Omega_1 \cup \Omega_2)}. \tag{4.2.18}$$

Proof. For the prove of this Lemma see [46]. □

4.2.3 A priori error estimate

We are now ready to prove the main result of this section. To this end, we introduce the discrete energy norm as follows:

$$|||u - u_h||| := \left(\|\nu_1 \nabla(\tilde{u}_1 - u_h^1)\|^2_{\Omega_h^1} + \|\nu_2 \nabla(\tilde{u}_2 - u_h^2)\|^2_{\Omega_h^2} \right)^{1/2},$$

where $\tilde{u}_i$ are smooth extensions of $u_i = u|_{\Omega_i}$ to Ω_h^i and $u_h^i := u_h|_{\Omega_h^i}$ for $i = 1, 2$.

Theorem 4.2.5 (A priori estimate)**.** *Let $\Omega \subset \mathbb{R}^2$ be a convex domain with polygonal boundary, which is resolved (exactly) by the family of triangulations Ω_h. We assume a splitting $\Omega = \Omega_1 \cup \Gamma \cup \Omega_2$, where Γ is a smooth interface with C^3-parametrization and that the solution u to (2.1.2) belongs to $H^3(\Omega_1 \cup \Omega_2)$. Moreover, we denote by n_l the maximum number of elements $K \in \Omega_h$, where the interface is approximated linearly. For the locally modified finite element solution $u_h \in V_h$ to (4.1.1) it holds*

$$|||u - u_h||| \leq \left(c_l n_l^{\frac{1}{2}} |\ln(h)|^{1/2} + c_q \right) h_P^2 \|u\|_{H^3(\Omega_1 \cup \Omega_2)}, \tag{4.2.19}$$

$$\|u - u_h\|_\Omega \leq \left(c_l n_l |\ln(h)|^{1/2} + c_q \right) h_P^3 \|u\|_{H^3(\Omega_1 \cup \Omega_2)}. \tag{4.2.20}$$

where c_l and c_q are generic constants that correspond to patches with a linear and a quadratic interface approximation, respectively. If additionally $u \in W^{2,\infty}(\Omega_1 \cup \Omega_2)$ we have further

$$|||u - u_h||| \leq \left(c_l n_l^{\frac{1}{2}} + c_q \right) h_P^2 \left(\|u\|_{H^3(\Omega_1 \cup \Omega_2)} + \|u\|_{W^{2,\infty}(\Omega_1 \cup \Omega_2)} \right). \tag{4.2.21}$$

Proof. (i) First, we have the following perturbed Galerkin orthogonality by subtracting (4.1.1) from (2.1.2)

$$a(u, \phi_h) - a_h(u_h, \phi_h) = (f - f_h, \phi_h)_\Omega \quad \forall \phi_h \in V_h. \tag{4.2.22}$$

We estimate the right-hand side in (4.2.22). The difference $f - f_h$ vanishes everywhere besides on S_h. We have

$$(f - f_h, \phi_h)_\Omega = (f - f_h, \phi_h)_{S_h} \leq \left(\|f_1\|_{S_h} + \|f_2\|_{S_h} \right) \|\phi_h\|_{S_h},$$

where f_i denotes a smooth extension of $f|_{\Omega_i}$ to $\Omega, i = 1, 2$.

We split the region S_h into parts with a quadratic interface approximation $S_{h,qu}$ and

parts with a linear approximation $S_{h,lin}$. (4.2.6) and (4.2.7) yield

$$\begin{aligned} \|f_i\|_{S_{h,qu}} + \|f_i\|_{S_{h,lin}} &\leq ch_P \|f\|_{H^1(\Omega_1\cup\Omega_2)} \leq ch_P \|u\|_{H^3(\Omega_1\cup\Omega_2)} \\ &\text{and} \\ \|f_i\|_{S_{h,qu}} + \|f_i\|_{S_{h,lin}} &\leq \left(ch_P^{\frac{3}{2}} + cn_l^{\frac{1}{2}} h_P^{\frac{3}{2}} |\ln(h)|^{1/2} \right) \|f\|_{H^1(\Omega_1\cup\Omega_2)} \\ &\leq \left(ch_P^{\frac{3}{2}} + cn_l^{\frac{1}{2}} h_P^{\frac{3}{2}} |\ln(h)|^{1/2} \right) \|u\|_{H^3(\Omega_1\cup\Omega_2)}. \end{aligned} \tag{4.2.23}$$

The second estimate yields

$$(f - f_h, \phi_h)_\Omega \leq ch_P^{\frac{3}{2}} \left(1 + n_l^{\frac{1}{2}} |\ln(h)|^{1/2} \right) \|u\|_{H^3(\Omega_1\cup\Omega_2)} \|\phi_h\|_{S_h}.$$

(ii) For the energy norm estimate, we start by splitting into an interpolatory and a discrete part

$$|||u - u_h||| \leq \|\nu_h^{1/2} \nabla(\tilde{u} - I_h u)\|_\Omega + \|\nu_h^{1/2} \nabla(I_h u - u_h)\|_\Omega. \tag{4.2.24}$$

The interpolatory part has already been estimated in Lemma 4.2.4. For the second term in (4.2.24), we use the perturbed Galerkin orthogonality (4.2.22) with $\varphi_h := I_h u - u_h$

$$\begin{aligned} \|\nu_h^{1/2} \nabla(I_h u - u_h)\|_\Omega^2 &= (\nu_h \nabla(I_h u - u_h), \nabla(I_h u - u_h))_\Omega \\ &= (\nu_h \nabla I_h u - \nu \nabla u, \nabla(I_h u - u_h))_\Omega + (f - f_h, I_h u - u_h)_\Omega. \end{aligned} \tag{4.2.25}$$

We split the first part in (4.2.25) further

$$\begin{aligned} (\nu_h \nabla I_h u - \nu \nabla u, \nabla(I_h u - u_h))_\Omega &= (\nu_h \nabla(I_h u - \tilde{u}), \nabla(I_h u - u_h))_\Omega \\ &\quad + (\nu_h \nabla \tilde{u} - \nu \nabla u, \nabla(I_h u - u_h))_\Omega . \end{aligned} \tag{4.2.26}$$

For the first part, we use (4.2.17) to get

$$(\nu_h \nabla(I_h u - \tilde{u}), \nabla(I_h u - u_h))_\Omega \leq ch_P^2 \left(n_l^{\frac{1}{2}} |\ln(h)|^{1/2} + 1 \right) \|u\|_{H^3(\Omega_1\cup\Omega_2)} \|\nu_h^{1/2} \nabla(I_h u - u_h)\|_\Omega. \tag{4.2.27}$$

The integrand in the second term on the right-hand side of (4.2.26) vanishes everywhere besides on S_h. We obtain by the Sobolev imbedding $H^3(\Omega_i) \subset W^{1,\infty}(\Omega_i)$, the continuity

of the extension (4.2.12) and (4.2.4) and (4.2.3) from Lemma 4.2.2

$$\begin{aligned}(\nu_h\nabla\tilde{u}-\nu\nabla u,\nabla(I_hu-u_h))_\Omega &= (\nu_h\nabla\tilde{u}-\nu\nabla u,\nabla(I_hu-u_h))_{S_h}\\ &\le c\left(\|\nabla\tilde{u}\|_{S_h}+\|\nabla u\|_{S_h}\right)\|\nu_h^{1/2}\nabla(I_hu-u_h)\|_{S_h}\\ &\le c|S_h|^{1/2}\|u\|_{W^{1,\infty}}(\Omega_1\cup\Omega_2)h_P^{1/2}\|\nu_h^{1/2}\nabla(I_hu-u_h)\|_{S_h}\\ &\le ch_P^2\left(n_l^{1/2}+1\right)\|u\|_{H^3(\Omega_1\cup\Omega_2)}\|\nu_h^{1/2}\nabla(I_hu-u_h)\|_\Omega\end{aligned} \tag{4.2.28}$$

For the second term in (4.2.25), we use (4.2.23) and (4.2.6)

$$\begin{aligned}(f-f_h,I_hu-u_h)_\Omega &\le ch_P\|u\|_{H^3(\Omega_1\cup\Omega_2)}\|I_hu-u_h\|_{S_h}\\ &\le ch_P^2\|u\|_{H^3(\Omega_1\cup\Omega_2)}\|\nu_h^{1/2}\nabla(I_hu-u_h)\|_{\Omega_1\cup\Omega_2}.\end{aligned}$$

Combining the estimates, we obtain

$$\left\|\nu_h^{\frac{1}{2}}\nabla(I_hu-u_h)\right\|_{\Omega_1\cup\Omega_2}\le ch_P^2\|u\|_{H^3(\Omega_1\cup\Omega_2)}$$

This completes the proof of (4.2.19). The proof of (4.2.21) follows exactly the same lines, with the only difference that we use (4.2.18) instead of (4.2.17) in (4.2.27) to get

$$(\nu_h\nabla(I_hu-\tilde{u}),\nabla(I_hu-u_h))_\Omega\le\ ch_P^2\left(n_l^{\frac{1}{2}}+1\right)\|u\|_{W^{2,\infty}(\Omega_1\cup\Omega_2)}\|\nu_h^{1/2}\nabla(I_hu-u_h)\|_\Omega. \tag{4.2.29}$$

(iii) To estimate the L^2 - norm error, we define the following adjoint problem. Let $z\in H_0^1(\Omega)$ be the solution of

$$(\nu\nabla\varphi,\nabla z)=\|e_h\|^{-1}(e_h,\varphi)_\Omega\quad\forall\varphi\in H_0^1(\Omega).$$

The solution z lies in in $H_0^1(\Omega)\cap H^2(\Omega_1\cup\Omega_2)$ and satisfies

$$\|z\|_{H^2(\Omega_1\cup\Omega_2)}\le c_s.$$

By choosing $\varphi=u-u_h=e_h$ and adding and subtracting $\nu_h\nabla u_h$, we have

$$\|e_h\|=(\nu\nabla e_h,\nabla z)_\Omega=(\nu\nabla u-\nu_h\nabla u_h,\nabla z)_\Omega+((\nu_h-\nu)\nabla u_h,\nabla z)_\Omega. \tag{4.2.30}$$

For the second term in (4.2.30), we have

$$((\nu_h-\nu)\nabla u_h,\nabla z)_\Omega=((\nu_h-\nu)\nabla u_h,\nabla z)_{S_h}\le C\left(\|\nu_h\nabla u_h\|_{S_h}\|\nabla z\|_{S_h}\right) \tag{4.2.31}$$

We split the first term on the right-hand side further and use the bound for the energy

norm error as well as (4.2.7) (Lemma 4.2.2)

$$\begin{aligned}\|\nu_h \nabla u_h\|_{S_h} &\leq \|\nu_h \nabla (u_h - u)\|_{S_h} + \|\nu \nabla u\|_{S_h} \\ &\leq c \left(n_l^{\frac{1}{2}} + 1 \right) h_P^{3/2} \|u\|_{H^3(\Omega_1 \cup \Omega_2)}.\end{aligned}$$

For the last term in (4.2.31), we obtain from (4.2.6) and (4.2.7)

$$\begin{aligned}\|\nabla z\|_{S_{h,lin}} &\leq c h_P^{\frac{3}{2}} \left(n_l^{\frac{1}{2}} |\ln(h)|^{1/2} + 1 \right) \|z\|_{H^2(\Omega_1 \cup \Omega_2)} \leq c h_P^{\frac{3}{2}} \left(n_l^{\frac{1}{2}} |\ln(h)|^{1/2} + 1 \right), \\ \|\nabla z\|_{S_{h,qu}} &\leq c h_P^{\frac{3}{2}} \|z\|_{H^2(\Omega_1 \cup \Omega_2)} \leq c h_P^{\frac{3}{2}}.\end{aligned}$$

Altogether, we obtain for the second term in (4.2.30)

$$((\nu_h - \nu) \nabla u_h, \nabla z)_\Omega \leq c h_P^3 \left(n_l |\ln(h)|^{1/2} + 1 \right) \|u\|_{H^3(\Omega_1 \cup \Omega_2)}. \tag{4.2.32}$$

Concerning the first term in (4.2.30), we add and subtract the interpolant $\nabla I_h z$, as well as $\pm \nu_h \tilde{u}$

$$\begin{aligned}(\nu \nabla u - \nu_h \nabla u_h, \nabla z)_\Omega = (\nu \nabla u - \nu_h \nabla \tilde{u}, \nabla (z - I_h z))_\Omega + (\nu_h \nabla (\tilde{u} - u_h), \nabla (z - I_h z))_\Omega \\ + (\nu \nabla u - \nu_h \nabla u_h, \nabla I_h z)_\Omega.\end{aligned} \tag{4.2.33}$$

For the first term on the right-hand side, we obtain as in (4.2.28)

$$(\nu \nabla u - \nu_h \nabla \tilde{u}, \nabla (z - I_h z))_\Omega \leq c h_P^{3/2} \left(n_l^{1/2} + 1 \right) \|u\|_{H^3(\Omega_1 \cup \Omega_2)} \|\nu_h^{1/2} \nabla (z - I_h z)\|_{S_h}$$

We estimate the latter norm using (4.2.6), (4.2.7) and (4.2.16)

$$\begin{aligned}\|\nu_h^{1/2} \nabla (z - I_h z)\|_{S_h} &\leq c h_P^{3/2} \left(n_l^{1/2} |\ln(h)|^{1/2} + 1 \right) \|z - I_h z\|_{H^2(\Omega_1 \cup \Omega_2)} \\ &\leq c h_P^{3/2} \left(n_l^{1/2} |\ln(h)|^{1/2} + 1 \right).\end{aligned}$$

The second term in (4.2.31) is easily estimated with the bound for the energy norm and the interpolation error (4.2.16)

$$(\nu_h \nabla (\tilde{u} - u_h), \nabla (z - I_h z))_\Omega \leq c \left(n_l^{\frac{1}{2}} + 1 \right) h_P^3 \|u\|_{H^3(\Omega_1 \cup \Omega_2)}.$$

For the third term in (4.2.33), we use the perturbed Galerkin orthogonality (4.2.22)

$$\begin{aligned}(\nu \nabla u - \nu_h \nabla u_h, \nabla I_h z)_\Omega &= (f - f_h, I_h z)_{S_h} \\ &\leq \|f_1 - f_2\|_{S_{h,lin}} \|I_h z\|_{S_{h,lin}} + \|f_1 - f_2\|_{S_{h,qu}} \|I_h z\|_{S_{h,qu}}.\end{aligned} \tag{4.2.34}$$

For the first part in both terms, we use (4.2.6) and (4.2.7), respectively

$$\begin{aligned}\|f_1 - f_2\|_{S_{h,lin}} + \|f_1 - f_2\|_{S_{h,qu}} &\leq ch_P^{\frac{3}{2}}\Big(n_l^{\frac{1}{2}}|\ln(h)|^{1/2} + 1\Big)\|f\|_{H^1(\Omega_1\cup\Omega_2)} \\ &\leq ch_P^{\frac{3}{2}}\Big(n_l^{\frac{1}{2}}|\ln(h)|^{1/2} + 1\Big)\|u\|_{H^3(\Omega_1\cup\Omega_2)}.\end{aligned}$$

For the remaining terms in (4.2.34), it is sufficient to consider the smallness of $|S_h|$, a Sobolev imbedding and the continuity of the extension (4.2.12)

$$\begin{aligned}&\|I_h z\|_{S_{h,lin}} \leq |S_{h,lin}|^{\frac{1}{2}}\|I_h z\|_{L^\infty(\Omega)} \leq cn_l^{\frac{1}{2}}h_P^{\frac{3}{2}}\|z\|_{L^\infty(\Omega)} \leq cn_l^{\frac{1}{2}}h_P^{\frac{3}{2}}\|z\|_{H^2(\Omega_1\cup\Omega_2)} \leq cn_l^{\frac{1}{2}}h_P^{\frac{3}{2}} \\ &\|I_h z\|_{S_{h,qu}} \leq |S_{h,qu}|^{\frac{1}{2}}\|I_h z\|_{L^\infty(\Omega)} \leq ch_P^{\frac{3}{2}}.\end{aligned}$$

Altogether this yields the following estimate for the term in (4.2.33), which completes the proof of the L^2-norm estimate

$$(\nu\nabla u - \nu_h\nabla u_h, \nabla z)_\Omega \leq ch_P^3\left(n_l|\ln(h)|^{1/2} + 1\right)\|u\|_{H^3(\Omega_1\cup\Omega_2)}.$$

□

Remark 4.2.1. *(Energy norm) There are different possibilities to choose the energy norm in Theorem 4.2.5. The result* (4.2.19) *could also be shown in the corresponding norm defined on the continuous sub-domains* Ω_1 *and* Ω_2

$$|||u - u_h|||_2 := \left(\|\nu_1\nabla(u_1 - \tilde{u}_h^1)\|_{\Omega_1}^2 + \|\nu_2\nabla(u_2 - \tilde{u}_h^2)\|_{\Omega_2}^2\right)^{1/2}, \tag{4.2.35}$$

where $u_i = u|_{\Omega_i}$ *and* $\tilde{u}_h^i$ *denote the canonical extensions of* $u_h^i := u_h|_{\Omega_h^i}$ *to* Ω_i*. If one would consider the norm*

$$|||u - u_h|||_3 := \|\nu_h^{1/2}\nabla(u - u_h)\|_\Omega \tag{4.2.36}$$

a reduced order of convergence, namely $\mathcal{O}(h_P^{\frac{3}{2}})$ *would result, even for a fully quadratic interface approximation (*$n_l = 0$*). The reason is that* ∇u *shows a discontinuity across* Γ*, while* ∇u_h *is discontinuous across the discrete interface* Γ_h*. Hence, the error in the gradient is* $\mathcal{O}(1)$ *in the strip* S_h *between the interfaces, which is of size* $|S_h|^{1/2} = \mathcal{O}(h_P^{3/2})$*. This bound is already optimal in the estimate for* $\|\nabla(u - \pi u)\|_\Omega$ *in* (4.2.15)*.*

We have chosen the discrete energy norm $|||u - u_h|||$ *in Theorem 4.2.5, as this is the only norm, which can be easily evaluated by numerical quadrature. A quadrature formula that evaluates the norms* (4.2.35) *or* (4.2.36) *accurately would need to resolve the strip* S_h*, which is non-trivial. Any standard approximation, such as a summed midpoint rule would lead to an additional quadrature error of* $\mathcal{O}(h_P^{3/2})$*, which would dominate the overall error.*

Remark 4.2.2. *(Regularity) We have assumed the regularity $u \in H^3(\Omega_1 \cup \Omega_2)$ (resp. $u \in W^{2,\infty}(\Omega_1 \cup \Omega_2)$) in Theorem 4.2.5. This is guaranteed if both sub-domains Ω_1 and Ω_2 are smooth (precisely $W^{3,\infty}$) and the right-hand side has regularity $f \in H^1(\Omega_1 \cup \Omega_2)$ (resp. $f \in L^\infty(\Omega_1 \cup \Omega_2)$). In this work, the overall domain Ω is assumed polygonal in order to avoid additional technicalities associated with the approximation of exterior curved boundaries. For the latter, we refer to the literature, for example [21].*

4.3 Numerical examples

The second order parametric finite element method is based on the finite element framework *Gascoigne 3d* [18]. The source code is freely available at `https://www.gascoigne.de` and published as zenodo repository [24]. For reproducibility of the numerical results, the following two configurations are implemented and described in a separate zenodo repository [84].

Example 1

We consider a square domain $\Omega = (0, 2)^2$. The domain is split into two domains Ω_1 and Ω_2 by the interface Γ. The interface is defined as $\Gamma\{(x, y) \in \Omega \,|\, l(x, y) = 0\}$ with the level-set function $l(x, y) = y - 2(x + \delta h)^2 + 0.5$, where $\delta \in [0, 1]$ and h is the mesh size. We take $\nu_1 = 4$ and $\nu_2 = 1$ and choose the exact solution as follows

$$u(x, y) = \begin{cases} \frac{1}{\nu_1} \sin(l), & \text{in } \Omega_1, \\ \frac{1}{\nu_2} \sin(l), & \text{in } \Omega_2, \end{cases}$$

and define a right-hand side $f_i = -\nu_i \Delta u$ and Dirichlet boundary data. We vary $\delta \in [0, 1]$, such that this example includes different configurations with arbitrary anisotropies. The configuration and the exact solution for this example are shown in Figure 4.3. In this

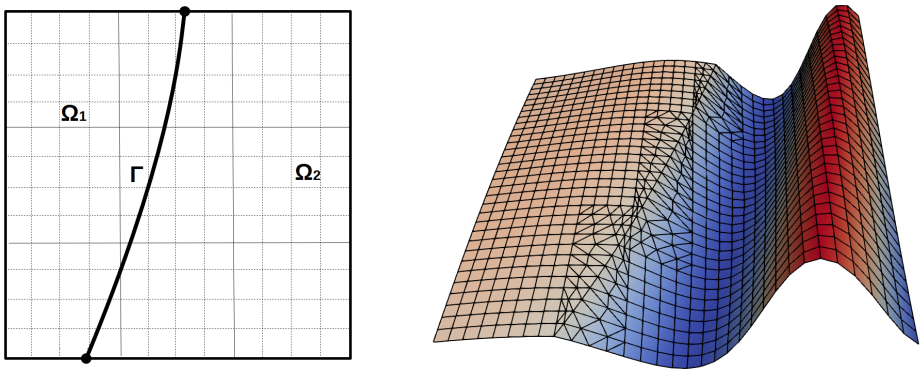

Figure 4.3: Left: Configuration of the test problem. Right: Sketch of the exact solution

example the interface could be resolved with second order on all refinement levels and for all $\delta \in [0, 1]$ ($n_l = 0$). Table 4.1 shows the discrete energy norm error $|||u - u_h|||$ and the

L^2-norm error as well as estimated convergence orders on several levels of global mesh refinement for the fixed parameter $\delta = 0$. According to the a priori error estimate in Theorem 4.2.5, we observe fully quadratic convergence in the discrete energy norm and fully cubic convergence in the L^2 - norm. In Figure 4.4, we plot the L^2-norm error for

h	L^2 - error	EOC	energy error	EOC
1/32	$3.43 \cdot 10^{-4}$	-	$4.19 \cdot 10^{-2}$	-
1/64	$4.24 \cdot 10^{-5}$	3.014	$1.04 \cdot 10^{-2}$	2.002
1/128	$5.28 \cdot 10^{-6}$	3.005	$2.61 \cdot 10^{-3}$	2.001
1/256	$6.59 \cdot 10^{-7}$	3.003	$6.52 \cdot 10^{-4}$	2.001

Table 4.1: Example 1. Errors in the L^2 - norm and the discrete energy - norm, including an estimated order of convergence which is computed from two consecutive values in each row for Example 1 and $\delta = 0$.

$\delta \in [0, 1]$ and the discrete energy norm error on several levels of global mesh refinement and observe that the error is bounded independently of δ.

In Figure 4.5, we show how the condition number depends on the parameter $\delta \in [0, 1]$ by moving the interface. We get the largest condition numbers at $\delta \approx 0.84$. Furthermore, we show a zoom-in of the numbers for $\delta \in [0.83; 0.85]$ in Figure 4.5, right. We see that the condition number is reduced by a factor of 100 using a scaled hierarchical basis, but that is not necessarily bounded for arbitrary anisotropies.

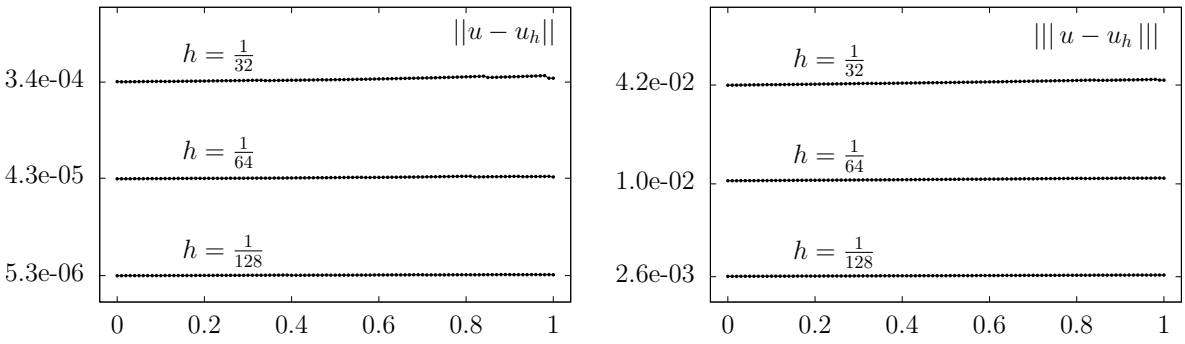

Figure 4.4: Example 1. L^2 - norm and discrete energy - norm errors for Example 1 with $x = 1.0 + \delta h$ and $\delta \in [0, 1]$.

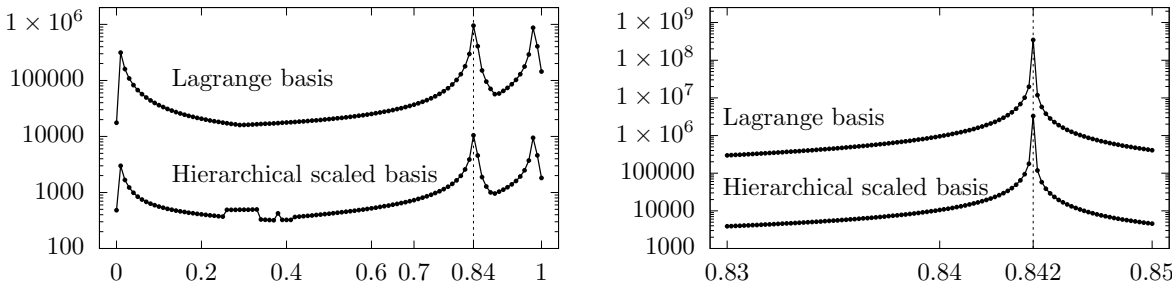

Figure 4.5: Condition number of the stiffness matrix depending on the position of the interface δ. Comparison of the standard Lagrangian basis and a scaled hierarchical basis for $h = 1/32$. *Left*: $\delta \in [0, 1]$. *Right*: Zoom-in for $\delta \in [0.83, 0.85]$.

Example 2

We consider a square domain $\Omega = (0, 2)^2$ that is split into a ball $\Omega_1 = B_r(x_0, y_0)$ with $r = 0.3$ and $(x_0, y_0) = (1 + \delta h, 1.2)$, where $\delta \in [0, 1]$, and $\Omega_2 = \Omega \setminus \bar{\Omega}_1$. We take the exact solution as in example 1, with the level set function replaced by $l(x, y) = (x - x_0)^2 + (y - y_0)^2 - r^2$. In Figure 5.14 we show the configuration and the exact solution for this example. For different $\delta \in [0, 1]$, this example includes all configurations A-E with different anisotropies. The L^2-norm and the discrete energy norm errors are shown in Figure 4.7 and Figure 4.8,

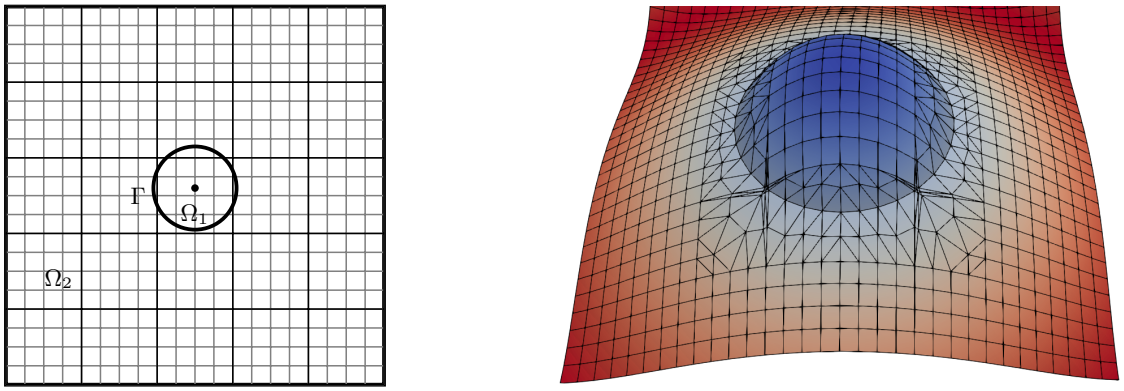

Figure 4.6: *Left*: Configuration of the test problem. *Right*: Sketch of the exact solution

respectively, for $\delta \in [0, 1]$ on several levels of global mesh refinement. We observe convergence in both norms for all $\delta \in [0, 1]$. The errors vary slightly depending on δ. Its magnitude depends mainly on the number of linearly approximated elements (n_l): We have $n_l = 0$ for $\delta = 0$ on all mesh levels, while $n_l > 0$ for all other values of δ. The errors increase from $\delta = 0$ to $\delta = 0.01$, as n_l increases from 0 to 8. Moreover, the number of linearly approximated elements increases once more from $n_l = 8$ to $n_l = 16$ for $h = 1/64$ and $h = 1/256$ in the range $\delta \in [0.74, 0.81]$ resp. $\delta \in [0.8, 0.81]$. Again, we observe a slight increase in the magnitude of the error within this range. This indicates that the constant $c_l n_l^{1/2}$ corresponding to the linearly approximated part in (4.2.21) is larger than the constant c_q arising from the quadratically approximated elements. Table 4.2, Table 4.3 and Table 4.4 show the L^2-norm and the discrete energy norm errors obtained

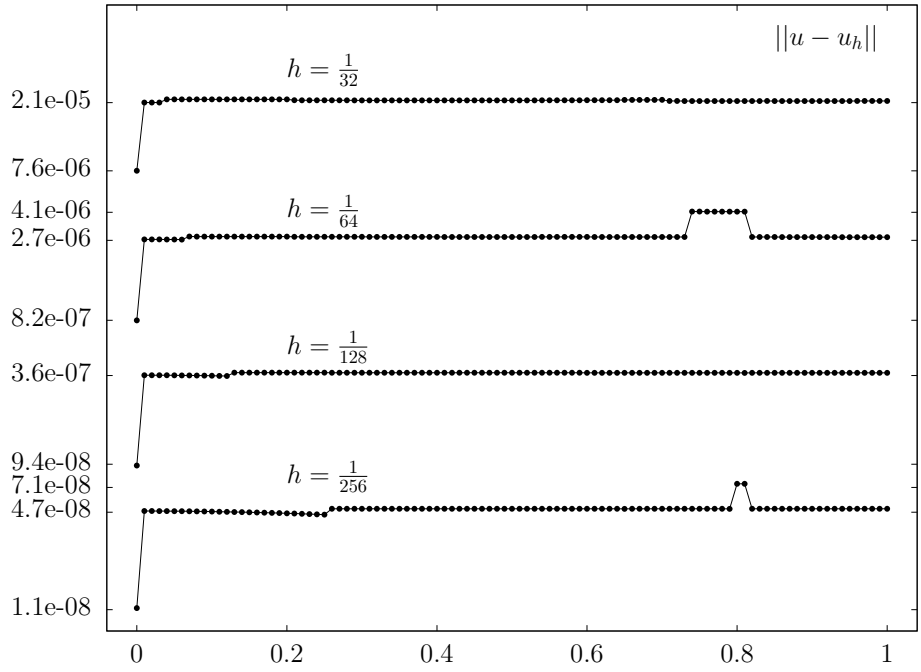

Figure 4.7: Example 2: L^2-norm error depending on $x = 1.0 + \delta h$ with $\delta \in [0, 1]$.

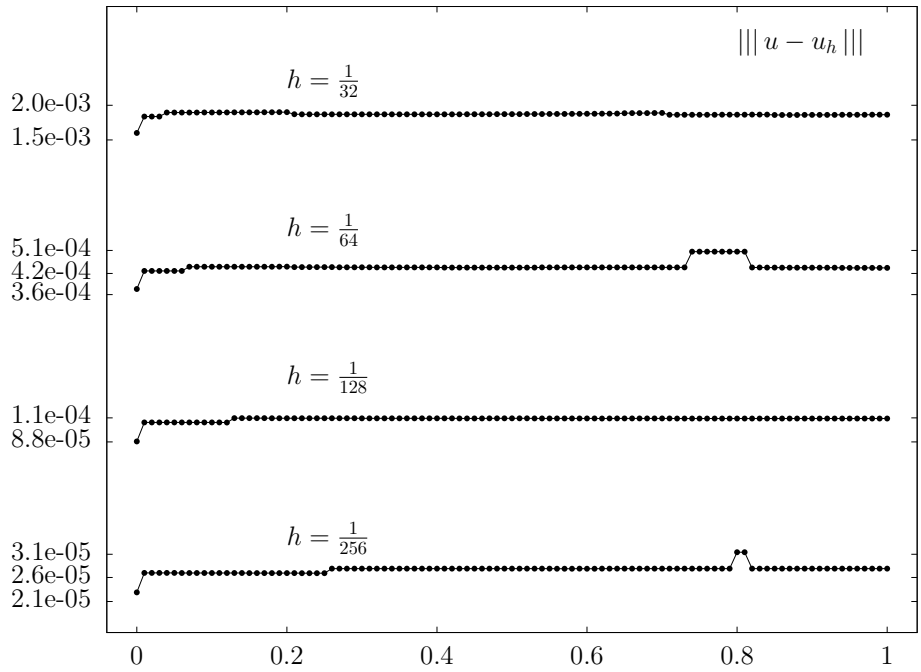

Figure 4.8: Example 2: Discrete energy-norm error depending on $x = 1.0 + \delta h$ with $\delta \in [0, 1]$.

on several levels of global mesh refinement for the fixed positions $x_0 = 1.0 + \frac{\delta_0}{64}$ of the midpoint, with $\delta_0 \in \{0,\ 0.01,\ 0.8\}$, which results in three different cases ($n_l = 0, n_l = 8$ and $n_l = 16$) for $h = 1/64$. In Table 4.2 ($\delta_0 = 0$) we observe fully quadratic (resp. cubic) convergence in the discrete energy norm (resp. the L^2-norm) as shown in Theorem 4.2.5, as no linearly approximated elements are present. This changes slightly for the other values of δ_0, see Table 4.3 and Table 4.4. In Table 4.3 ($\delta_0 = 0.01$), we see that 8 linearly

h	L^2 - error	EOC	energy error	EOC
1/32	$7.61 \cdot 10^{-6}$	-	$1.54 \cdot 10^{-3}$	-
1/64	$8.18 \cdot 10^{-7}$	3.217	$3.63 \cdot 10^{-4}$	2.089
1/128	$9.41 \cdot 10^{-8}$	3.119	$8.83 \cdot 10^{-5}$	2.039
1/256	$1.12 \cdot 10^{-8}$	3.064	$2.17 \cdot 10^{-5}$	2.021

Table 4.2: Example 2. L^2 - norm and discrete energy - norm errors, and convergence order for $\delta_0 = 0$ ($n_l = 0$).

approximated elements were required on all mesh levels. The convergence order in the discrete energy norm seems to be fully quadratic (according to (4.2.21)), while in the L^2-norm error the logarithmic factor $\ln(|h|)^{1/2}$ leads to a slightly reduced convergence, as predicted in Theorem 4.2.5. For $\delta_0 = 0.8$, the number n_l varies between 8 and 16, see

h	L^2 - error	EOC	energy error	EOC	PN	n_l
1/32	$2.10 \cdot 10^{-5}$	-	$1.80 \cdot 10^{-3}$	-	18	8
1/64	$2.73 \cdot 10^{-6}$	2.942	$4.29 \cdot 10^{-4}$	2.066	36	8
1/128	$3.61 \cdot 10^{-7}$	2.919	$1.05 \cdot 10^{-4}$	2.028	76	8
1/256	$4.78 \cdot 10^{-8}$	2.919	$2.60 \cdot 10^{-5}$	2.015	154	8

Table 4.3: Example 2. L^2- and discrete energy - norm errors for $\delta_0 = 0.01$, including estimated convergence orders obtained from two consecutive values. PN denotes the number of patches which are cut by the interface and n_l the number of linearly approximated elements.

Table 4.4. This is again reflected in the magnitude of the error: The reduction factor lies below 4 in the energy norm, and below 8 in the L^2-norm error when n_l increases and above 4 resp. 8 when n_l decreases. This shows again that the term $c_l n_l^{1/2} \ln(|h|)^{1/2}$ in front of the linearly approximated part is larger than the constant c_q in front of the quadratic counterpart. For $\delta_0 = 0.8$ and $h_P = \frac{1}{32}$, we show the resulting finite element mesh in Figure

h	L^2 - error	EOC	energy error	EOC	PN	n_l
1/32	$2.15 \cdot 10^{-5}$	-	$1.83 \cdot 10^{-3}$	-	18	8
1/64	$4.14 \cdot 10^{-6}$	2.377	$5.14 \cdot 10^{-4}$	1.833	36	16
1/128	$3.74 \cdot 10^{-7}$	3.465	$1.09 \cdot 10^{-4}$	2.233	76	8
1/256	$7.17 \cdot 10^{-8}$	2.384	$3.16 \cdot 10^{-5}$	1.790	152	16

Table 4.4: Example 2. L^2 and discrete energy - norm errors, including an estimated convergence order for $\delta = 0.8$.

4.9, where in 8 of the 18 patches, which are cut by the interface, a linear approximation was required, including a zoom around one linearly approximated patch on the right. In

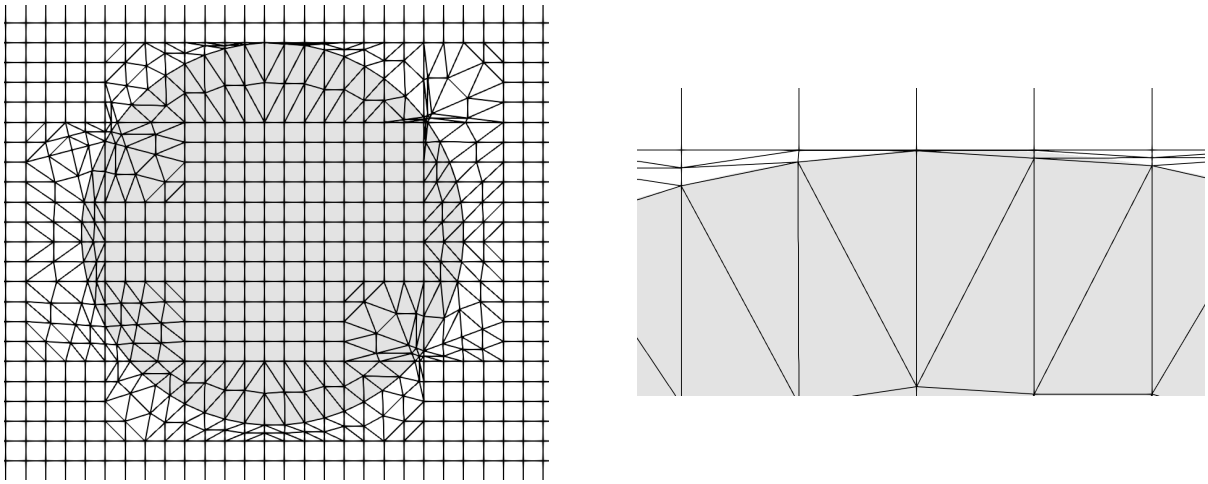

Figure 4.9: Example 2. *Left*: Illustration of the sub-elements for $h = 1/32$ and $\delta = 0.8$. *Right*: Zoom of the upper part with linearly approximated elements (top right).

Figure 4.10 we show how the condition numbers depend on the parameter $\delta \in [0, 1]$ when moving the interface. We get the largest condition numbers at $\delta \approx 0.04$ for $h = 1/32$ and at $\delta \approx 0.07$ for $h = 1/64$, respectively. The condition numbers are again reduced by a factor of approx. 100 for the scaled hierarchical basis compared to the standard Lagrangian basis.

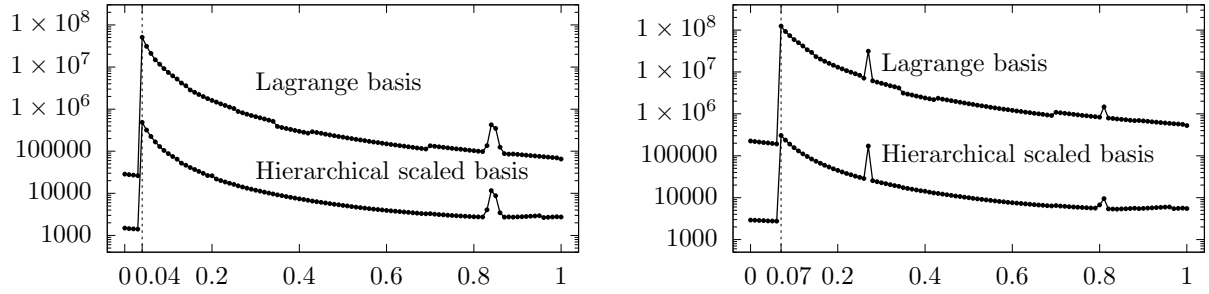

Figure 4.10: Example 2. Condition number of the stiffness matrix depending on the displacement of the circle. Comparison of the Lagrange and hierarchical scaled basis for $h = 1/32$ (left) and $h = 1/64$ (right).

Chapter 5: Discretization of two-phase flow problems

5.1 Stokes interface problem and stability analysis

In this section, we analyze a stationary Stokes interface problem (2.3.1) without surface tension. We consider the following linear Stokes model problem

$$\begin{aligned} -\nabla\cdot(\nu_i\,\nabla\boldsymbol{u}) + \nabla p = \boldsymbol{f}, \qquad \nabla\cdot\boldsymbol{u} = \mathbf{0} \qquad &\text{in} \quad \Omega_i, \quad i=1,2, \\ [\![\boldsymbol{u}]\!] = \mathbf{0}, \qquad [\![(\nu\,\nabla\boldsymbol{u} - p\,\mathbb{I})\;\boldsymbol{n}]\!] = 0 \qquad &\text{on} \quad \Gamma, \\ \boldsymbol{u} = \mathbf{0} \qquad &\text{on} \quad \partial\Omega, \end{aligned} \tag{5.1.1}$$

where $[\![w]\!] := (w|_{\Omega_2})|_\Gamma - (w|_{\Omega_1})|_\Gamma$ and a discontinuous viscosity coefficient ν is defined as follows:

$$\nu = \begin{cases} \nu_1, & \text{in } \Omega_1 \\ \nu_2, & \text{in } \Omega_2. \end{cases}$$

For the velocity field we use the space $\boldsymbol{V} = H_0^1(\Omega)^2$ and for the pressure, we define the space

$$L := \left\{ q \in L^2(\Omega) : \quad \int_\Omega \nu^{-1} q \,\mathrm{d}x = 0 \right\}.$$

The corresponding norms for any $\boldsymbol{u} \in \boldsymbol{V}$ and $p \in L$ as follows:

$$\|\nabla\boldsymbol{u}\|_\nu := (\nu\nabla\boldsymbol{u}, \nabla\boldsymbol{u})^{\frac{1}{2}}, \quad \|p\|_\nu := (\nu^{-1}p, p)^{\frac{1}{2}}.$$

The weak form of the Stokes interface problem (5.1.1) reads:
Find $(\boldsymbol{u}, p) \in \boldsymbol{V} \times L$ such that

$$\begin{aligned} A(\boldsymbol{u},p)(\boldsymbol{\varphi}) = (\boldsymbol{f},\boldsymbol{\varphi}) \qquad &\forall\,\boldsymbol{\varphi} \in \boldsymbol{V} \\ (\nabla\cdot\boldsymbol{u},\phi) = 0 \qquad &\forall\,\phi \in L \end{aligned} \tag{5.1.2}$$

where

$$A(\boldsymbol{u},p)(\boldsymbol{\varphi}) := (\nu\nabla\boldsymbol{u},\nabla\boldsymbol{\varphi}) - (\nabla\cdot\boldsymbol{\varphi}, p)\,.$$

For the discretization, we apply *locally modified second order finite elements* for velocity, which are introduced in chapter 3 and *piecewise constant finite elements* for pressure. First, we prove the stability of the locally modified finite element pair $\mathcal{P}_2 - \mathcal{P}_0$ for the Stokes interface problem. The technique used to check the stability is a macroelement technique. In other words, the stability is tested by checking local stability and a relatively

simple global stability. Furthermore, we prove optimal error estimates in the L^2-norm and sub-optimal estimations in an energy norm for the Stokes interface problems. Also, we present numerical examples to substantiate the analytical results.

Literature review

Finite element pairs, which satisfy the discrete *inf-sup* condition for the discrete Stokes problem are known for isotropic meshes, see, e.g., [40] and [93]. Reusken and Olshanskii in [79] analyzed a Stokes interface problem and showed the *inf-sup* result for the discrete problem that is uniform with respect to the jump in the viscosity coefficient. Moreover, the authors derived a robust estimate for the discretization error. Lehrenfeld in [73] presented a higher order unfitted finite element method, which is based on a Taylor-Hood $\mathcal{P}_2 - \mathcal{P}_1$ velocity-pressure pair for the Stokes interface problem and used a ghost penalty stabilization to obtain the *inf-sup* stability. Hansbo and others in [62] used a cut FEM for the Stokes interface problems and they proposed to use a Nitsche formulation to allow discontinuities along the interface.

The stability of the mixed finite element method for incompressible flow on meshes containing anisotropically refined elements has attracted considerable attention in the literature. Many authors intensively discussed such kind of problems with non-conforming and conforming methods. Some results on stability of velocity-pressure pairs on anisotropic meshes for non-conforming methods are given by Apel et al. in [4, 6, 7] and by Rannacher and Turek in [82]. The stability proof for the element pair $\mathcal{P}_k^+ - \mathcal{P}_{k-1}$ is given by Apel and Matthies in [6].

Some of the first results for conforming methods start with Becker and Rannacher in [19]. In this paper, the authors introduced stabilized $\mathcal{Q}_1 - \mathcal{P}_0$ and $\mathcal{Q}_1 - \mathcal{Q}_1$ elements on anisotropic meshes and proved the *inf-sup* condition with a constant independent of the aspect ratio. Schötzau, Schwab and Stenberg in [85] consider $\mathcal{Q}_k - \mathcal{Q}_{k-2}$ and $\mathcal{P}_k - \mathcal{P}_{k-2}$, $k \geq 2$ elements for the *hp*-version of the finite element method, in particular $\mathcal{Q}_2 - \mathcal{P}_0$ rectangular element. They showed that for boundary layer patches the *inf-sup* constant does not depend on aspect ratio, but only on a polynomial order. The case for the corner patch has to be treated carefully. Therefore, in this case, the authors advised to use geometric tensor product meshes near corners and proved the stability for this. Another related study is presented by Apel and Nicaise in [90], where they proved the *inf-sup* condition for Bernardi/Raugel elements on anisotropic meshes. Furthermore, a pressure stabilization on anisotropic meshes has been studied for the pressure-stabilized Petrov-Galerkin method by Apel et al. [5]. In [14], Barrenechea and Wachtel proved a uniform *inf-sup* condition for the lowest-order Taylor–Hood pairs $\mathcal{Q}_2 - \mathcal{Q}_1$ and $\mathcal{P}_2 - \mathcal{P}_1$ on a family of affine anisotropic meshes.

These results were refined in a paper [2] by Ainsworth and Coggings. They considered the finite element pair with smaller velocity space such that $\mathcal{Q}_{k+\max\{\mu k,1\},k} - \mathcal{P}_{k-1}$, with

a fixed constant $\mu \in [0, 1]$. It was shown that the stability constant depends only of the polynomial order and μ. They did not consider a geometric tensor product mesh in the corner patch. The mesh is constructed by using layer and corner macroelements for a general polygonal domain Ω. Moreover, Ainsworth and others in [1] presented $\mathcal{Q}_{k+1} - \mathcal{P}_{k-1}$ mixed finite elements and showed how to suppress the spurious pressure modes in order to restore the stability and presented two results. In the first result it was shown that the approximation properties of the constrained pressure space and the unconstrained pressure space are essentially identical. Thus, it gave the minimal constraints on the pressure space needed to restore stability with respect to aspect ratio. The second result showed that the stabilized finite element scheme is robust with respect to the aspect ratio of the elements.

5.1.1 Locally modified finite element spaces and discrete weak form

Let $\mathcal{T}_P$ be a fully structured quadrilateral patch mesh. Each patch $P \subset \mathcal{T}_P$ is split into either 4 smaller quadrilaterals (when P is not cut by the interface) or into 8 triangles, according to the type of the cut, see Figure 5.1. We call $P \in \mathcal{T}_P$ the patches, $K \in P$ the elements of $\mathcal{T}_h$ which is the mesh consisting of all triangles. For each $K \in \mathcal{T}_h$ we denote by $\Lambda_K : \hat{K} \to K$ the reference map, where $\hat{K}$ is the unit triangle.

On $\mathcal{T}_h$ we define $\boldsymbol{V}_h \subset \boldsymbol{V}$ for the discrete velocities, $L_h \subset L^2(\Omega)$ for the discrete pressure as follows:

$$\begin{aligned} \boldsymbol{V}_h &:= \{\boldsymbol{\varphi} \in [C(\Omega)]^2 \,|\, (\boldsymbol{\varphi} \circ \Lambda_K^{-1}) \in [\mathcal{P}_K^2(\hat{K})]^2 \text{ for } K \in \mathcal{T}_h,\ \boldsymbol{\varphi} = \mathbf{0} \text{ on } \partial\Omega\}, \\ L_h &:= \{\phi \in L_0^2(\Omega) \,|\, \phi \in \mathcal{P}_K^0(K) \text{ for } K \in \mathcal{T}_h\}. \end{aligned} \tag{5.1.3}$$

Moreover, we define

$$\boldsymbol{V}_h^1 := \{\boldsymbol{\varphi} \in \boldsymbol{C}(\Omega) \,|\, (\boldsymbol{\varphi} \circ \Lambda^{-1}) \in [\mathcal{P}_K^1(\hat{K})]^2 \text{ for } K \in \mathcal{T}_h,\ \boldsymbol{\varphi} = \mathbf{0} \text{ on } \partial\Omega\}, \tag{5.1.4}$$

a space that will also be used later. We distinguish five configurations for the patches which are cut by the interface, see Figure 5.1. Note that depending on the parameters $r, s \in (0, h_P)$ the patches can include highly anisotropic triangles.

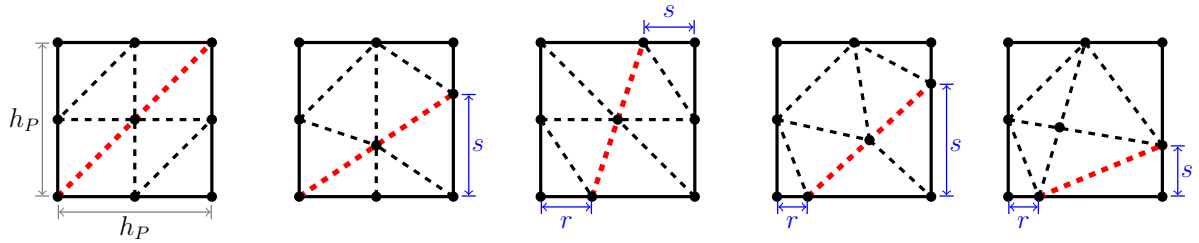

Figure 5.1: Illustration of patches P cut by interface. The red dashed line is the interface. The parameters r and s can take all values between 0 and h_P.

Lemma 5.1.1 (Maximum-angle condition)**.** *We assume that the patch grid $\mathcal{T}_P$ is Cartesian, consisting of patches with size $h_P \times h_P$. For all types of the interface cuts, the interior angles of all subelements are bounded by* 127° *independently of the parameters $r, s \in (0, h_P)$.*

Proof. The proof is given in Chapter 3, see Theorem 3.1.2. □

This maximum angle condition allows us to define robust Lagrangian interpolation operators $I_h \boldsymbol{u} : H^2(K) \cap C(\bar{K}) \to \boldsymbol{V}_h$ with accurate error estimates

$$\|\boldsymbol{u} - I_h \boldsymbol{u}\|_K \leq c_1 \, h_{K,\max}^2 \, \|\nabla^2 \boldsymbol{u}\|_K, \tag{5.1.5}$$

$$\|\nabla(\boldsymbol{u} - I_h \boldsymbol{u})\|_K \leq c_2 \, h_{K,\max} \, \|\nabla^2 \boldsymbol{u}\|_K. \tag{5.1.6}$$

where c_1, c_2 are positive constants and $h_{K,\max}$ is the maximum diameter of a triangle $K \in P$ (see e.g. [3]). The interpolation error estimates are robust with respect to the maximum diameter $h_{K,\max} \approx h_P$ that is of the same order as the diameter of the patches P.

Discrete weak form

The discrete formulation reads: Find $(\boldsymbol{u}_h, p_h) \in \boldsymbol{V_h} \times L_h \subset \boldsymbol{V} \times L$ such that

$$\begin{aligned} A_h(\boldsymbol{u}_h, p_h)(\boldsymbol{\varphi}_h) &= (\boldsymbol{f}_h, \boldsymbol{\varphi}_h) \qquad && \forall\, \boldsymbol{\varphi}_h \in \boldsymbol{V}_h \\ (\nabla \cdot \boldsymbol{u}_h, \phi_h) &= 0 && \forall\, \phi_h \in L_h \end{aligned} \tag{5.1.7}$$

where $\boldsymbol{f}_h|_{\Omega_h^i} := \boldsymbol{f}_i, i = 1, 2$ and $\boldsymbol{f}_i$ is a smooth extension of $\boldsymbol{f}|_{\Omega_i}$ to Ω_h^i.

The bilinear form is given by

$$A_h(\boldsymbol{u}_h, p_h)(\boldsymbol{\varphi}_h) := (\nu \nabla \boldsymbol{u}_h, \nabla \boldsymbol{\varphi}_h) \, + \, \delta\nu \, (\nabla \boldsymbol{u}_h, \nabla \boldsymbol{\varphi}_h)_{S_h} \, - \, (\nabla \cdot \boldsymbol{\varphi}_h, p_h)$$

where $S_h = S_h^1 \cup S_h^2$, S_h^i is the mismatch between Ω_h^i and Ω^i $i = 1, 2$ (see Figure 4.1)

$$\begin{aligned} S_h^1 &:= \Omega_h^1 \setminus \Omega_1 = \Omega_2 \setminus \Omega_h^2, \\ S_h^2 &:= \Omega_h^2 \setminus \Omega_2 = \Omega_1 \setminus \Omega_h^1. \end{aligned}$$

and $\delta\nu$ defined as follows

$$\delta\nu = \begin{cases} \nu_1 - \nu_2, & x \in S_h^1 \\ \nu_2 - \nu_1, & x \in S_h^2. \end{cases}$$

5.1.2 Macroelement technique

The aim of the macroelement approach consists in reducing the global proof of the discrete *inf-sup* condition to the proof of a local version of it. The idea behind localizing the

discrete stability condition was introduced by Boland and Nicolaides [22] and Stenberg [89]. In this work, we use the approach of Boland and Nicolaides and follow [90] and [85]. For that we use a two-level family of meshes, i.e. micro- and macrotriangulation. The macrotriangulation $\mathcal{T}_{\mathcal{M}}$ is a splitting of the domain into quadrilateral macroelements. Further, we assume that macroelements are isotropic. The microtriangulation $\mathcal{T}_h$ is the splitting of the domain into triangular elements that has been introduced above. Each macroelement $M \in \mathcal{T}_{\mathcal{M}}$ is a collection of triangles $K \subset \mathcal{T}_{\mathcal{M}}$ such that M is isotropic. We define a two-level family of meshes as shown in Figure 5.2.

- The micro-triangulation $\mathcal{T}_h$:
$$\bar{\Omega} = \bigcup_{T \in \mathcal{T}_h} \bar{T}$$
- The macro-triangulation $\mathcal{T}_M$:
$$\bar{\Omega} = \bigcup_{M \in \mathcal{T}_M} \bar{M}$$

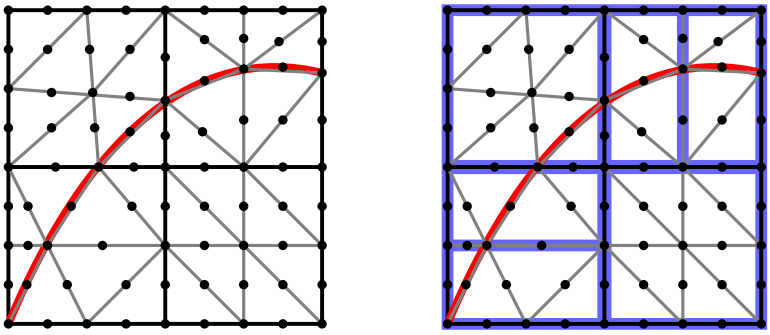

Figure 5.2: Left (microtriangulation): Mesh consisting of four patches, three of which are cut by the interface (red line). Right (macrotriangulation): Macroelement partitions of the patches which are cut or not cut by the interface.

For each macroelement $M \in \mathcal{T}_M$ we define the spaces

$$\begin{aligned} \boldsymbol{V}_h(M) &:= \{\boldsymbol{u}_h \in \boldsymbol{V}_h \,:\, \boldsymbol{u}_h = \boldsymbol{0} \quad \text{in} \quad \Omega \setminus M\}, \\ L_h(M) &:= \{p_h \in L_h \,:\, \int_M p_h \,\mathrm{d}x = 0,\, p_h = 0 \quad \text{in} \quad \Omega \setminus M\}. \end{aligned} \tag{5.1.8}$$

5.1.3 Types of the macroelements

We distinguish seven configurations **A - G** for the patches and corresponding types of macroelements. We note that depending on the interface-cut, the patches can include highly anisotropic triangles.
Depending on the configuration we determine two different ways for splitting a patch $P \in \mathcal{T}_P$ into macroelements $M \in \mathcal{T}_M$:

- **Macroelements: A, B, F, G.** The patch P is not split, therefore the macroelement is the entire patch $M = P$. In the configurations **A** and **B** the macroelement consists

of isotropic triangles $T \in \mathcal{T}_h$ only, see Figure 5.3. But in cases **F** and **G**, the macroelement might contain anisotropic triangles.

- **Macroelements: C, D, E.** The patch P is split into two or three isotropic quadrilaterals. In cases **C** and **D** from Figure 5.3 we split the patch P into two rectangular macroelements M_1, M_2 so that the new inner edge $e_m = \partial M_1 \cap \partial M_2$ meets the boundary of P only in P's edges that are not intersected by the interface, see Figure 5.3 (bottom). The case **E** is split into three isotropic macroelements as shown in Figure 5.3 (bottom).

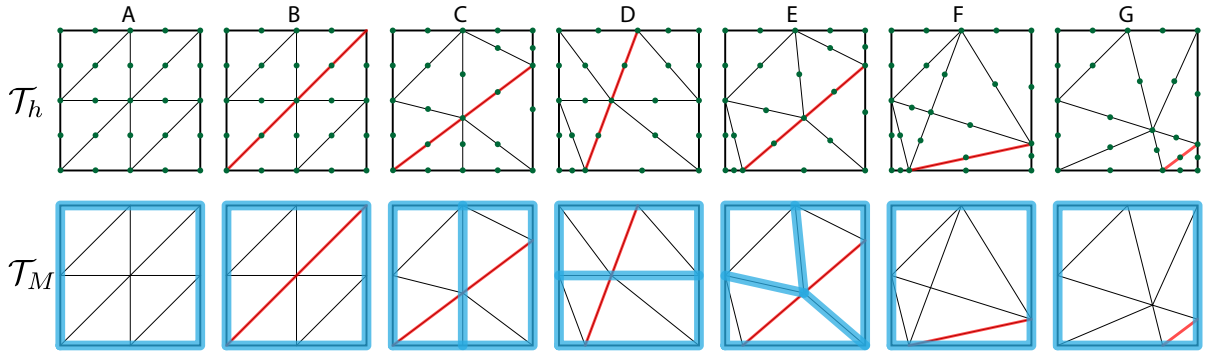

Figure 5.3: Illustration of configurations **A - G**. The upper row shows the microtriangulation $\mathcal{T}_h$ depending on the interface location and the lower row the splitting into macroelements used for inf-sup stability. The red line is the interface.

Depending on the configuration, the macroelements can include isotropic and anisotropic triangular elements, see Figures 5.1 and 5.3.

Macroelements of isotropic elements. In the following two cases we observe macroelements with isotropic elements only:

- All macroelements which are not cut by interface, configuration **A** in Figure 5.3, see also Figure 5.2.
- Configuration **B** from the Figure 5.3.

Macroelements of anisotropic elements. The configurations **C - G** in Figure 5.3 which depend on the parameters r and s can include anisotropic elements, see Figures 5.4 and 5.5. Hence, we need to be carefully by defining the macroelements.

Lemma 5.1.2 (Macroelement)**.** *The macroelements mesh $\mathcal{T}_M$ has the following properties: For each $M \in \mathcal{T}_M$ of type A–F*

- *M is an union of at least two triangles $T \in \mathcal{T}_h$ that share a common edge*
- *If M contains an anisotropic triangle $T \in M$, its shortest edge is on the boundary of M*

- *If $T \in M$ is anisotropic with dimensions $h_{min} \times h_{max}$, where $h_{min} < h_{max}$, the complete triangle is close, $\mathcal{O}(h_{min})$, to the boundary of the macroelement.*

Proof. We present in Figure 5.4 the macroelements **C - F** which contain the anisotropic elements depending on the interface. As we see, all shortest edges of the anisotropic triangles lie on the boundary of the macroelement. Moreover, as shown in the first and third macroelements in Figure 5.4, there are some anisotropic triangles with two long edges which are not on the boundary of the macroelement. However, these anisotropic triangles lie close to the boundary of the macroelement. □

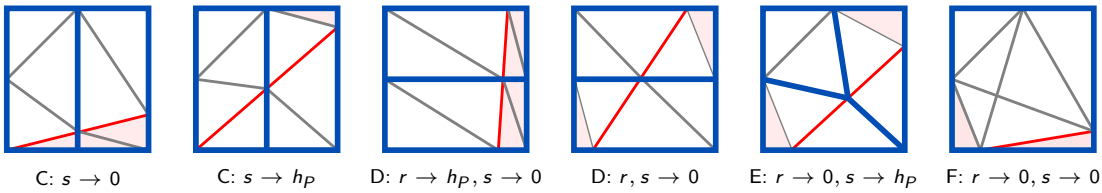

Figure 5.4: Illustration of macroelements **C - F** which are included the anisotropic elements (red filled).

Remark 5.1.1 (A special case for macroelement G)**.** *In Figure 5.5, we see the macroelement **G** which is the entire patch. The macroelement **G** contains one anisotropic triangle whose shortest edge lies on the boundary of the macroelement. However, there are two anisotropic triangles whose shortest edges γ_1 and γ_2 do not lie on the boundary of the macroelement. In this case we use an edge stabilisation on these edges. For further details see also Remark 5.1.3 and Lemma 5.1.5.*

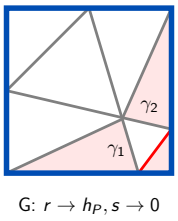

Figure 5.5: Illustration of macroelement **G** which is included the anisotropic elements (red filled).

5.1.4 Local stability

We show the stability locally for each macroelement. We denote a local parametrization of the interface on the patch by γ and its linear approximation by γ_h. Furthermore, α and δ are the angle and maximum distance between the interface and linear approximation of the interface, respectively. For the notations see Figure 5.6. As we mentioned in Section 3.2.2, the maximum distance δ between the interface and the linear interface approximation is bounded by $\mathcal{O}(h_P^2)$.

Remark 5.1.2. *As the interface satisfies $\gamma \in C^2$ and $\delta = \mathcal{O}(h_P^2)$, we observe that $\delta \to 0$ and $\alpha \to 0$ when $h \to 0$. It holds*

$$|\gamma'(0)| \leq h \max |\gamma''| \leq h\, C_\gamma,$$

where C_γ is the constant. Thus, we can use for the stability proof the illustration from Figure 5.1 where the patch is cut by the straight line as an interface.

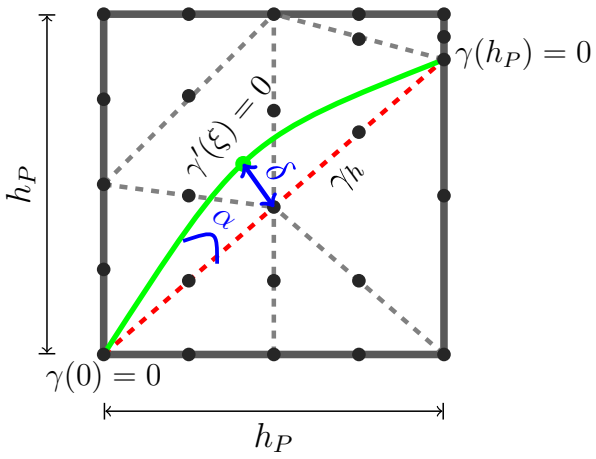

Figure 5.6: Illustration of the patch with the size $h_P \times h_P$. The local parametrization of the interface γ (green line) and its linear approximation γ_h (dashed red line).

On the macroelement $M \in \mathcal{T}_M$ we consider the local spaces $\boldsymbol{V}_h(M)$ and $L_h(M)$, see (5.1.8). Furthermore, we define on $M \in \mathcal{T}_M$ the local space of piecewise linear functions as follows

$$\boldsymbol{V}_h^1(M) := \{\boldsymbol{u} \in \boldsymbol{V}_h^1 \,:\, \boldsymbol{u} = \boldsymbol{0} \quad \text{in} \quad \Omega \setminus M\},$$

where $\boldsymbol{V}_h^1$ is the space of linear velocities, see (5.1.4). To show the stability in the macroelements **A - F**, we construct for each macroelement a Fortin operator. For each macroelement M we define $\boldsymbol{V}(M) = H_0^1(M)^2$.

Definition 5.1.1 (A possible construction of a Fortin Operator)**.** *We construct a linear Fortin operator $\Pi_M : \boldsymbol{V}(M) \to \boldsymbol{V}_h(M)$ with help of two linear operators*

$C_M : \boldsymbol{V}(M) \to \boldsymbol{V^1}_h(M)$ which maps into the space of piecewise linear functions, and $E_M : \boldsymbol{V}(M) \to \boldsymbol{V}_h(M)$ satisfying the following conditions:

$$\|\nabla C_M \boldsymbol{u}\|_M \leq c_1 \|\nabla \boldsymbol{u}\|_M \quad \forall\, \boldsymbol{u} \in \boldsymbol{V}(M) \tag{5.1.9}$$

$$\|E_M(\boldsymbol{u} - C_M \boldsymbol{u})\|_M \leq c_2 \|\nabla \boldsymbol{u}\|_M \quad \forall\, \boldsymbol{u} \in \boldsymbol{V}(M) \tag{5.1.10}$$

$$(\nabla \cdot (\boldsymbol{u} - E_M \boldsymbol{u}),\, p_h)_M = 0 \quad \forall p_h \in L_h(M),\ \forall\, \boldsymbol{u} \in \boldsymbol{V}(M), \tag{5.1.11}$$

where $c_1, c_2 > 0$ are constants independent of the mesh size. Then the Fortin operator is defined by

$$\Pi_M \boldsymbol{u} := C_M \boldsymbol{u} + E_M(\boldsymbol{u} - C_M \boldsymbol{u}). \tag{5.1.12}$$

The construction of the operators C_M and E_M will be given in the following. First, we show that Π_M is indeed a Fortin operator.

Lemma 5.1.3 (A Property of the Operator (5.1.12))**.** *The operator $\Pi_M : \boldsymbol{V}(M) \to \boldsymbol{V}_h(M)$ defined in* (5.1.12) *satisfies the Fortin criterion*

$$\|\nabla\, \Pi_M\, \boldsymbol{u}\|_M \leq c\, \|\nabla \boldsymbol{u}\|_M \quad \forall\, \boldsymbol{u} \in \boldsymbol{V}(M), \tag{5.1.13}$$

$$(\nabla \cdot \Pi_M \boldsymbol{u},\, p_h)_M = (\nabla \cdot \boldsymbol{u}, p_h)_M \quad \forall p_h \in L_h(M),\ \forall\, \boldsymbol{u} \in \boldsymbol{V}(M). \tag{5.1.14}$$

Thus, the local set of spaces $\boldsymbol{V}_h(M) - \boldsymbol{L}_h(M)$ is stable.

Proof. (i) The estimation (5.1.13) is obtained by applying the triangle inequality and using (5.1.9) and (5.1.10)

$$\|\nabla\, \Pi_M\, \boldsymbol{u}\|_M \leq \|\nabla\, C_M\, \boldsymbol{u}\|_M + \|E_M(\boldsymbol{u} - C_M \boldsymbol{u})\|_M \leq c_1\, \|\nabla \boldsymbol{u}\|_M + c_2\, \|\nabla \boldsymbol{u}\|_M = c\, \|\nabla \boldsymbol{u}\|_M,$$

with $c = c_1 + c_2$.
(ii) It is easy to check that (5.1.14) holds. Using (5.1.11) we have

$$\begin{aligned}(\nabla \cdot \Pi_M \boldsymbol{u},\, p_h)_M &= (\nabla \cdot C_M \boldsymbol{u},\, p_h)_M + (\nabla \cdot E_M(\boldsymbol{u} - C_M \boldsymbol{u}),\, p_h)_M \\ &= (\nabla \cdot C_M \boldsymbol{u},\, p_h)_M + (\nabla \cdot (\boldsymbol{u} - C_M \boldsymbol{u}),\, p_h)_M \\ &= (\nabla \cdot \boldsymbol{u},\, p_h)_M\,.\end{aligned}$$

□

Only the macroelements **A, B, F** and **G** have one inner corner point of a triangle. Hence, for types **C, D, E** it holds

$$C_M \boldsymbol{u} = 0$$

for all $\boldsymbol{u} \in \boldsymbol{V}(M)$ as $C_M \boldsymbol{u} \in \boldsymbol{V}^1(M)$ is linear.

The remaining case **A, B, F** and **G** have one inner node only. In the following we will call it $x_m \in M$ and $\omega := \{K \in M \mid x_m \in \partial K\}$ is the patch of elements containing this point.

Definition 5.1.2 (Construction of the Clément Interpolation)**.** *Let $\boldsymbol{u} \in \boldsymbol{V}(M)$. We define the Clément type operator $C_M : \boldsymbol{V}(M) \to \boldsymbol{V}_h^1(M)$*

$$C_M \boldsymbol{u} := \pi_\omega(\boldsymbol{u})\, \varphi_\omega, \quad \pi_\omega(\boldsymbol{u}) := |\omega|^{-1} \int_\omega \boldsymbol{u} dx, \tag{5.1.15}$$

where φ_ω is the basis function of the degree of freedom x_m, for the notations see Figure 5.7.

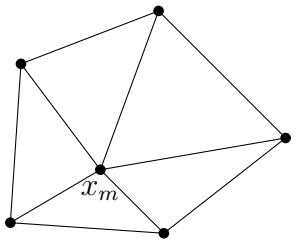

Figure 5.7: Illustration of the notation for the patch ω.

Definition 5.1.3 (Construction of the operator E_M)**.** *Let $\boldsymbol{u} \in \boldsymbol{V}(M)$. We define the linear operator $E_M : \boldsymbol{V}(M) \to \boldsymbol{V}_h(M)$ by the conditions*

$$E_M \boldsymbol{u}|_T(x_i) = 0, \quad \int_{\sigma_i} E_M\, \boldsymbol{u} \cdot \boldsymbol{n}_i\, ds = \int_{\sigma_i} \boldsymbol{u} \cdot \boldsymbol{n}_i\, ds, \quad \forall T \in M, \tag{5.1.16}$$

where x_i and σ_i for $i = 1, 2, 3$ are the vertices and the edges of the triangle T, respectively. For the notations see Figure 5.8. Then we can construct the operator E_M as follows

$$E_M \boldsymbol{u} = \sum_{i=1}^{3} \chi_i(\boldsymbol{u})\, \varphi_i \boldsymbol{n}_i, \quad \chi_i(\boldsymbol{u}) = \frac{1}{\int_{\sigma_i} \varphi_i\, ds} \int_{\sigma_i} \boldsymbol{u} \cdot \boldsymbol{n}_i\, ds, \tag{5.1.17}$$

with the Lagrange basis functions φ_i attached to the three edges σ_i.

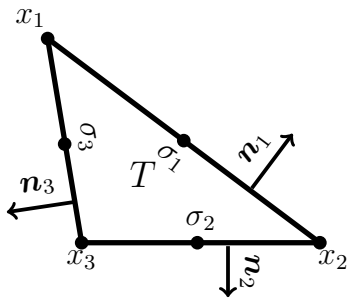

Figure 5.8: Illustration of the notation for one triangle $T \in M$

Stability of Macroelements

We show the stability for the different types of macroelements from Figure 5.3 separately.

Macroelements (A, B). In this case, the patch P is not split. The macroelement of type **A, B** is the entire patch $M = P$.

Lemma 5.1.4 (Local inf-sup stability in macroelements of type **A, B**)**.** *Let M be any macroelement of configurations **(A, B)**. Then the operator Π_M is the Fortin type operator and well defined for $\boldsymbol{u} \in \boldsymbol{V}(M)$, we have*

$$\|\nabla \Pi_M \boldsymbol{u}\|_M \leq c \|\nabla \boldsymbol{u}\|_M \quad \forall \boldsymbol{u} \in \boldsymbol{V}(M), \tag{5.1.18}$$

$$(\nabla \cdot (\boldsymbol{u} - \Pi_M \boldsymbol{u}), p_h)_M = 0 \quad \forall p_h \in L_h(M), \forall \boldsymbol{u} \in \boldsymbol{V}(M). \tag{5.1.19}$$

*Thus, the local set of spaces $\boldsymbol{V}_h(M) - \boldsymbol{L}_h(M)$ for all M of the configurations **(A, B)** is stable.*

Proof. Since all elements of the macroelement types **A, B** are isotropic, the stability results in this case are well known, see, e.g. [93]. The idea is to construct a Fortin operator by using the Clément interpolation to treat nodal values. □

Macroelements (C, D, E). We denote by $M \in \mathcal{T}_M$ one of the macroelements corresponding to the configurations **C**, **D** or **E** in Figure 5.3. We note that all non-vanishing velocity degrees of feedom of a function $\boldsymbol{u}_h \in \boldsymbol{V}_h(M)$ are on inner edges σ that belong to triangles $\sigma \in \partial T$ making up the macroelement M. All corner points lie on the boundary of the macroelement where $\boldsymbol{u} = \boldsymbol{0}$ and thus $C_M \boldsymbol{u} = 0$. Then we construct an interpolation operator Π_M from definition 5.1.1 only with the E_M operator in 5.1.12 as follows:

$$\Pi_M \boldsymbol{u} = E_M \boldsymbol{u}, \tag{5.1.20}$$

where the operator E_M is defined in definition 5.1.3.

Lemma 5.1.5 (Local inf-sup stability in macroelements of type **C, D, E**)**.** *Let M be any macroelement of the configurations **(C, D, E)**. Then the operator E_M is the Fortin type operator and well defined for $\boldsymbol{u} \in \boldsymbol{V}(M)$, we have*

$$\|\nabla E_M \boldsymbol{u}\|_M \leq c \|\nabla \boldsymbol{u}\|_M \quad \forall \boldsymbol{u} \in \boldsymbol{V}(M), \tag{5.1.21}$$

$$(\nabla \cdot (\boldsymbol{u} - E_M \boldsymbol{u}), p_h)_M = 0 \quad \forall p_h \in L_h(M), \forall \boldsymbol{u} \in \boldsymbol{V}(M). \tag{5.1.22}$$

*Thus, the local set of spaces $\boldsymbol{V}_h(M) - \boldsymbol{L}_h(M)$ for all M of the configurations **(C, D, E)** is stable.*

Proof. (i) By noting that p_h is the pieceweise constant and using the construction of E_M

in (5.1.16), we can easily show the orthogonality condition:

$$(\nabla \cdot (\boldsymbol{u} - E_M \boldsymbol{u}),\, p_h)_M = \sum_{T \in M} \left[-(\boldsymbol{u} - E_M \boldsymbol{u},\, \underbrace{\nabla p_h}_{=0})_T + \langle \underbrace{\boldsymbol{n} \cdot (\boldsymbol{u} - E_M \boldsymbol{u})}_{=0},\, p_h \rangle_{\partial T} \right] = 0$$

for all $\boldsymbol{u} \in \boldsymbol{V}(M)$ and $p_h \in L_h(M)$.

(ii) It remains to show the stability estimate (5.1.21). For this, we use the interpolation operator E_M from Definition 5.1.3 such that

$$E_M\, \boldsymbol{u} = \sum_{i=1}^{3} \left(\frac{1}{\int_{\sigma_i} \varphi_i \,\mathrm{d}s} \int_{\sigma_i} \boldsymbol{u} \cdot \boldsymbol{n}_i \,\mathrm{d}s \right) \varphi_i \boldsymbol{n}_i.$$

Here, we only discuss the case of anisotropic triangles, they are filled in red in Figure 5.4. For the isotropic triangles it can be shown with standard technique from the literature, i.e. [93].

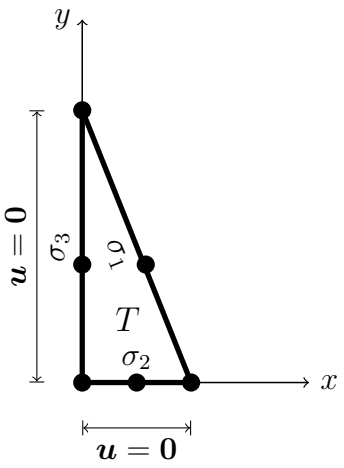

Figure 5.9: Illustration of the notation for the anisotropic triangle T, with two edges σ_2, σ_3 that lie on the boundary of the macroelement.

We denote the smallest edge of the anisotropic triangle by $|\sigma_2| = h_{min}$ and observe

$$\|\nabla \varphi_i\|_T \leq h_{min}^{-1} \sqrt{|T|}.$$

First, we only consider the anisotropic triangles, where σ_2 and σ_3 lie on ∂M with $\boldsymbol{u} = \boldsymbol{0}$, see Figure 5.9. The remaining case, appearing in configurations **C** and **D** is discussed

below. It holds

$$\begin{aligned}\|\nabla E_M \boldsymbol{u}\|_T &\leq h_{min}^{-1}\sqrt{|T|}\left|\sum_{i=1}^{3}\frac{1}{|\sigma_i|}\int_{\sigma_i}\boldsymbol{u}\cdot\boldsymbol{n}_i\,\mathrm{d}s\right| = h_{min}^{-1}\sqrt{|T|}\,\frac{1}{|\sigma_1|}\left|\int_{\sigma_1}\boldsymbol{u}\cdot\boldsymbol{n}_1\,\mathrm{d}s\right| \\ &\leq h_{min}^{-1}\sqrt{|T|}\,|\sigma_1|^{-1}\left|\int_{\sigma_1}\boldsymbol{u}\cdot\boldsymbol{n}_1\,\mathrm{d}s+\int_{\sigma_2}\underbrace{\boldsymbol{u}\cdot\boldsymbol{n}_2}_{=\mathbf{0}}\,\mathrm{d}s+\int_{\sigma_3}\underbrace{\boldsymbol{u}\cdot\boldsymbol{n}_3}_{=\mathbf{0}}\,\mathrm{d}s\right| \\ &\leq h_{min}^{-1}\sqrt{|T|}\,|\sigma_1|^{-1}\left|\int_{\partial T}\boldsymbol{u}\cdot\boldsymbol{n}\,\mathrm{d}s\right| \leq h_{min}^{-1}\sqrt{|T|}\,|\sigma_1|^{-1}\left|\int_T\nabla\cdot\boldsymbol{u}\,\mathrm{d}x\right|\end{aligned}$$

Then with $|T| = \mathcal{O}(|\sigma_1|\cdot h_{min})$ we obtain

$$\|\nabla E_M \boldsymbol{u}\|_T \leq \frac{1}{|\sigma_1|}\cdot\frac{\sqrt{|T|}}{h_{min}}\cdot\sqrt{|T|}\,||\nabla\boldsymbol{u}||_T \leq c\,||\nabla\boldsymbol{u}||_T. \tag{5.1.23}$$

As shown in Figure 5.10, the macroelement belonging to configurations **C** or **D** can contain two anisotropic elements T_1 and T_2. The anisotropic triangle T_1 is treated as above. We note that the anisotropic triangle T_2 consists of two long edges σ_1 and σ_3 which do not lie on the boundary of the macroelement, see Figure 5.10, the triangle T_2. In this case, we can still use the above estimate by noting that the shortest edge σ_2 of the anisotropic triangle T_2 lies on ∂M where $\boldsymbol{u} = \mathbf{0}$.

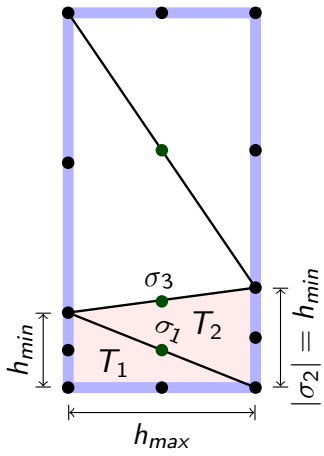

Figure 5.10: Macroelement with two anisotropic elements T_1 and T_2.

It holds

$$
\begin{aligned}
\|\nabla E_M \boldsymbol{u}\|_{T_2} &\leq h_{min}^{-1}\sqrt{|T_2|}\ \left|\sum_{i=1}^{3}\frac{1}{|\sigma_i|}\int_{\sigma_i}\boldsymbol{u}\cdot\boldsymbol{n}_i\,\mathrm{d}s\right| \\
&\leq h_{min}^{-1}\sqrt{|T_2|}\ \frac{1}{\min\{|\sigma_1|,|\sigma_3|\}}\ \left(\left|\int_{\sigma_1}\boldsymbol{u}\cdot\boldsymbol{n}_1\,\mathrm{d}s\right|+\left|\int_{\sigma_3}\boldsymbol{u}\cdot\boldsymbol{n}_3\,\mathrm{d}s\right|\right) \\
&\leq h_{min}^{-1}\sqrt{|T_2|}\ \frac{1}{\min\{|\sigma_1|,|\sigma_3|\}}\ \left|\int_{\sigma_1}\boldsymbol{u}\cdot\boldsymbol{n}_1\,\mathrm{d}s\right| + h_{min}^{-1}\sqrt{|T_2|}\ \frac{1}{\min\{|\sigma_1|,|\sigma_3|\}} \\
&\times\left|\int_{\sigma_1}\boldsymbol{u}\cdot\boldsymbol{n}_1\,\mathrm{d}s+\int_{\sigma_2}\underbrace{\boldsymbol{u}\cdot\boldsymbol{n}_2}_{=\mathbf{0}}\,\mathrm{d}s+\int_{\sigma_3}\boldsymbol{u}\cdot\boldsymbol{n}_3\,\mathrm{d}s-\int_{\sigma_1}\boldsymbol{u}\cdot\boldsymbol{n}_1\,\mathrm{d}s\right| \\
&\leq h_{min}^{-1}\sqrt{|T_2|}\ \frac{1}{\min\{|\sigma_1|,|\sigma_3|\}}\ \left|\int_{\sigma_1}\boldsymbol{u}\cdot\boldsymbol{n}_1\,\mathrm{d}s\right| \\
&+ h_{min}^{-1}\sqrt{|T_2|}\ \frac{1}{\min\{|\sigma_1|,|\sigma_3|\}}\ \left(\left|\int_{\partial T_2}\boldsymbol{u}\cdot\boldsymbol{n}\,\mathrm{d}s\right|+\left|\int_{\sigma_1}\boldsymbol{u}\cdot\boldsymbol{n}_1\,\mathrm{d}s\right|\right) \\
&\leq h_{min}^{-1}\sqrt{|T_2|}\ \frac{1}{\min\{|\sigma_1|,|\sigma_3|\}}\ \left(\left|\int_{T_2}\nabla\cdot\boldsymbol{u}\,\mathrm{d}x\right|+2\left|\int_{\sigma_1}\boldsymbol{u}\cdot\boldsymbol{n}_1\,\mathrm{d}s\right|\right) \\
&\leq h_{min}^{-1}\sqrt{|T_2|}\ \frac{1}{\min\{|\sigma_1|,|\sigma_3|\}}\ \left(\left|\int_{T_2}\nabla\cdot\boldsymbol{u}\,\mathrm{d}x\right|+2\left|\int_{T_1}\nabla\cdot\boldsymbol{u}\,\mathrm{d}x\right|\right) \\
&\leq h_{min}^{-1}\sqrt{|T_2|}\ \frac{1}{\min\{|\sigma_1|,|\sigma_3|\}}\ \left(\sqrt{|T_2|}\ ||\nabla\boldsymbol{u}||_{T_2}+2\sqrt{|T_1|}\ ||\nabla\boldsymbol{u}||_{T_1}\right).
\end{aligned}
$$

It holds with $|T_2| = \mathcal{O}(h_{min}\cdot h_{max}) = |T_1|$ and $\min\{|\sigma_1|,|\sigma_3|\} = \mathcal{O}(h_{max})$

$$
\|\nabla E_M \boldsymbol{u}\|_{T_2} \leq \frac{\sqrt{|T_2|}}{h_{min}\cdot h_{max}}\ \cdot 2\sqrt{|T_2|}\ \left(\,||\nabla\boldsymbol{u}||_{T_2}+||\nabla\boldsymbol{u}||_{T_1}\,\right) \leq c\,||\nabla\boldsymbol{u}||_{T_2}. \tag{5.1.24}
$$

With estimates (5.1.23) and (5.1.24) the *inf-sup* stability of cases **C, D, E** follows. □

Macroelement (F). For patches of type **F** a splitting into isotropic macroelements is not possible such that the complete patch $P \in \mathcal{T}_P$ is considered as macroelement M. In constrast to cases **C, D, E**, this macroelement has an inner degree of freedom x_m where $\boldsymbol{u}(x_m) \neq \mathbf{0}$, see Figure 5.11. Thus, we use the Definition 5.1.1 for defining the interpolation operator Π_M such that

$$
\Pi_M\boldsymbol{u} = C_M\boldsymbol{u} + E_M(\boldsymbol{u} - C_M\boldsymbol{u}).
$$

The interpolation operators C_M and E_M are defined in the Definitions 5.1.2 and 5.1.3, respectively. First, we show the interpolation estimations for the Clément operator.

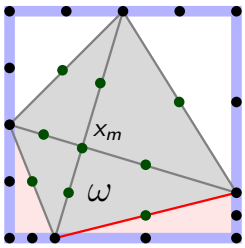

Figure 5.11: Macroelement of the configuration **F** for the case $r, s \to 0$. The red line is the interface. The red filled elements are anisotropic elements. The black points are the nodes which are contained on the boundary of the macroelement and the green points are the nodes which are located inside of the macroelements. x_m is the vertex of the element. ω is a isotropic support of x_m.

Lemma 5.1.6. *Let $T \in M$, then it holds for all $\boldsymbol{u} \in \boldsymbol{V}(M)$*

$$\|\boldsymbol{u} - C_M\boldsymbol{u}\|_T \leq c\, h_T\, \|\nabla \boldsymbol{u}\|_M, \tag{5.1.25}$$

$$\|\nabla(\boldsymbol{u} - C_M\boldsymbol{u})\|_T \leq c\, \|\nabla \boldsymbol{u}\|_M, \tag{5.1.26}$$

with $h_T = \operatorname{diam}(T)$. Further,

$$\|\nabla C_M\boldsymbol{u}\|_T \leq c\, \|\nabla \boldsymbol{u}\|_M. \tag{5.1.27}$$

Proof. (i) First, we consider $T \in M$ with $T \in M \setminus \omega$ here it holds

$$C_M\boldsymbol{u}|_T = 0.$$

With Poincarés inequality

$$\|\boldsymbol{u} - C_M\boldsymbol{u}\|_T = \|\boldsymbol{u}\|_T \leq h_T \|\nabla \boldsymbol{u}\|_T \leq h_T \|\nabla \boldsymbol{u}\|_M,$$

and, naturally,

$$\|\nabla C_M\boldsymbol{u}\|_T = 0 \leq c\, \|\nabla \boldsymbol{u}\|_M.$$

(ii) Next, $T \in \omega \subset M$. Two nodes of T are on the boundary ∂M and only one inner node x_m exists, such that

$$C_M\boldsymbol{u}|_T = \varphi_m \cdot \pi_\omega(\boldsymbol{u}).$$

All $T \in \omega$ are isotropic and it holds

$$h_M \leq c_1\, h_T, \quad \operatorname{diam}(\omega) \leq c_2\, h_T \tag{5.1.28}$$

with a constants $c_1, c_2 > 0$ independent of M, ω and T and $h_M = \mathit{diam}(M)$. Further, with

Poincaré inequality (the version for average-zero functions)

$$\|\boldsymbol{u} - \pi_\omega(\boldsymbol{u})\|_T \leq \|\boldsymbol{u} - \pi_\omega(\boldsymbol{u})\|_\omega \leq c\,\mathrm{diam}(\omega)\,\|\nabla\left(\boldsymbol{u} - \pi_\omega(\boldsymbol{u})\right)\|_\omega \leq c\,h_T\|\nabla\boldsymbol{u}\|_M, \quad (5.1.29)$$

and

$$\begin{aligned} |\pi_\omega(\boldsymbol{u})| &\leq |\omega|^{-1}\int_\omega |\pi_\omega(\boldsymbol{u})|\,\mathrm{d}x \leq |\omega|^{-\frac{1}{2}}\,\|\boldsymbol{u}\|_{L^2(\omega)} \leq |\omega|^{-\frac{1}{2}}\,\|\boldsymbol{u}\|_{L^2(M)} \\ &\leq |\omega|^{-\frac{1}{2}}\,h_M\,\|\nabla\boldsymbol{u}\|_M \leq c\,\|\nabla\boldsymbol{u}\|_M. \end{aligned} \quad (5.1.30)$$

(iii) As $\varphi_1 + \varphi_2 + \varphi_m = 1$ it holds with $|\varphi_i| \leq 1$ for $i = 1, 2, m$

$$\begin{aligned} \|\boldsymbol{u} - C_M\boldsymbol{u}\|_T \;&\leq\; \sum_{i=1}^{2}\|\varphi_i\boldsymbol{u}\|_T + \|\varphi_m(\boldsymbol{u} - \pi_\omega(\boldsymbol{u}))\|_T \;\leq\; \sum_{i=1}^{2}\|\boldsymbol{u}\|_T + \|\boldsymbol{u} - \pi_\omega(\boldsymbol{u})\|_T \\ &\leq\; 2\,\|\boldsymbol{u}\|_M + \|\boldsymbol{u} - \pi_\omega(\boldsymbol{u})\|_\omega \end{aligned}$$

with (5.1.29) we obtain

$$\|\boldsymbol{u} - C_M\boldsymbol{u}\|_T \;\leq\; 3\,c\,h_T\,\|\nabla\boldsymbol{u}\|_M.$$

(iv) Now, we show (5.1.27). It holds

$$\|\nabla C_M\boldsymbol{u}\|_T \leq \|\nabla(\pi_\omega(\boldsymbol{u})\varphi_m)\|_T \leq |\pi_\omega(\boldsymbol{u})|\,\|\nabla\varphi_m\|_T.$$

Using $\|\nabla\varphi_m\|_T \leq c$ (since $T \in \omega$ is isotropic triangle) and (5.1.30) we get

$$\|\nabla C_M\boldsymbol{u}\|_T \leq c\,\|\nabla\boldsymbol{u}\|_M.$$

(v) Next, we show the estimation (5.1.26). It holds by triangle inequality and (5.1.27)

$$\|\nabla(\boldsymbol{u} - C_T\boldsymbol{u})\|_T \leq \|\nabla\boldsymbol{u}\|_T + \|\nabla C_M\boldsymbol{u}\|_T \leq c\,\|\nabla\boldsymbol{u}\|_M.$$

□

Lemma 5.1.7 (Local inf-sup stability in macroelement of type **F**)**.** *Let M be any macroelement of configuration **(F)**. Then the operator Π_M defined as in* (5.1.12) *is the Fortin type operator and well defined for $\boldsymbol{u} \in \boldsymbol{V}(M)$, since the operators $C_M : \boldsymbol{V}(M) \to \boldsymbol{V}_h^1(M)$ and $E_M : \boldsymbol{V}(M) \to \boldsymbol{V}_h(M)$ satisfy the following conditions:*

$$\|\nabla C_M\boldsymbol{u}\|_M \leq c_1\,\|\nabla\boldsymbol{u}\|_M \quad \forall\,\boldsymbol{u} \in \boldsymbol{V}(M) \quad (5.1.31)$$

$$\|E_M(\boldsymbol{u} - C_M\boldsymbol{u})\|_M \leq c_2\,\|\nabla\boldsymbol{u}\|_M \quad \forall\,\boldsymbol{u} \in \boldsymbol{V}(M) \quad (5.1.32)$$

$$(\nabla\cdot(\boldsymbol{u} - E_M\boldsymbol{u}),\,p_h)_M = 0 \quad \forall p_h \in L_h(M),\ \forall\,\boldsymbol{u} \in \boldsymbol{V}(M), \quad (5.1.33)$$

where c_1, c_2 are the constants independent of the mesh size.
*Thus, the local set of spaces $\boldsymbol{V}_h(M) - \boldsymbol{L}_h(M)$ for all M of the configuration **(F)** is stable.*

Proof. *(i)* The stability estimate (5.1.31) follows from Lemma 5.1.6.
(ii) We show the stability estimate (5.1.32). For this by denoting $\boldsymbol{w} := \boldsymbol{u} - C_T\,\boldsymbol{u}$ we show the stability of the $E_M\boldsymbol{w}$. As shown in Figure 5.11, the macroelement of configuration **F** contains isotropic and anisotropic triangles. For the isotropic triangles $E_M\boldsymbol{w}$ can be estimate by standard techniques from the literature, i.e. [93]. For the anisotropic triangles (filled in red in Figure 5.11), the stability of $E_M\boldsymbol{w}$ is treated as in the proof of the Lemma 5.1.5. Then with estimate (5.1.26), we get the assertion.

(iii) The orthogonality condition (5.1.33) is shown in Lemma 5.1.5. □

Remark 5.1.3 (Instability of macroelement **G**)**.** *The configuration* **G** *can contain one small triangle T_s where all three sides are short and two anisotropic triangles T_1 and T_2, see Figure 5.12. We will demonstrate numerically that this configuration is not inf-sup stable, when the triangle T_s is getting smaller. We observe the instability of the pressure in Example 1 from section 5.1.8, see Figure 5.15. If the triangle T_s from Figure 5.12 is getting smaller, the spurious discrete pressure is growing. This is shown in Table 5.1 (Left) via the maximum norm of the pressure error.*

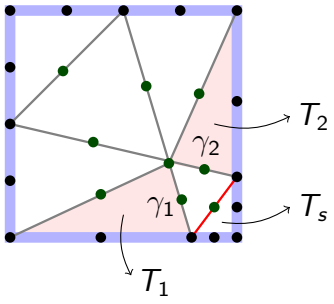

Figure 5.12: Macroelement of the configuration **G**. The smallest edges of the anisotropic elements T_1 and T_2 are denoted by γ_1 and γ_2, respectively. The black points are the nodes which are contained on the boundary of the macroelement and the green points are the inner nodes of the macroelement.

Remark 5.1.4. *We have omitted the case* ***G*** *with anisotropic triangles. Here, the element is not stable and we must add further stabilization terms. This is described in [1] and we refer also to Example 1 in section 5.1.8.*

Remark 5.1.5 (*Inf-sup* stability of the stabilized macroelement **G**)**.** *As mentioned in Remark 5.1.4, the instability from Remark 5.1.3 was corrected numerically by using the following stabilzation term:*

$$A_s(p,\xi) = \alpha\,|\gamma_i| \int_{\gamma_i} [\![p]\!]\,[\![\xi]\!]\,ds \quad i = 1,2, \tag{5.1.34}$$

where $\alpha > 0$ is the stabilization parameter, γ_1 and γ_2 are the small edges of the anisotropic triangles T_1 and T_2 from Figure 5.12 (red filled triangles). We get local inf-sup stability for the macroelement $\mathbf{G}$*, if we enrich the variational formulation with an additional pressure stabilization term* (5.1.34)*. For further details, see [1].*

Finally, by combining Lemma 5.1.4, Lemma 5.1.5, Lemma 5.1.7 and Remark 5.1.5, we obtain local *inf-sup* stability in all macroelements from Figure 5.3.

Corollary 5.1.1 (Local *inf-sup* condition)**.** *Let M be any macroelement from Figure 5.3 except type* $\boldsymbol{G}$*, then there exists a constant $\gamma_M > 0$, independent of the mesh size, such that*

$$\inf_{p_h \in L_h(M)} \sup_{\boldsymbol{u}_h \in \boldsymbol{V}_h(M)} \frac{(p_h, \nabla \cdot \boldsymbol{u}_h)_M}{\|\nabla \boldsymbol{u}_h\|_M \|p_h\|_M} \geq \gamma_M, \tag{5.1.35}$$

for all $M \in \mathcal{T}_M$.

Remark 5.1.6. *The* inf-sup *condition* (5.1.35) *can be written in another useful way, namely for each $p_h \in L_h(M)$ there exists a $\boldsymbol{u}_h \in \boldsymbol{V}_h(M)$ such that:*

$$(p_h, \nabla \cdot \boldsymbol{u}_h)_M = \|p_h\|_M^2, \quad \|\nabla \boldsymbol{u}_h\|_M \leq \gamma_M^{-1} \|p_h\|_M.$$

5.1.5 Stability of subspace

In this section, we show the stability of the subspace. For that we have to define a subspace $\bar{V}_h$ by using an appropriate projection, see [90]. First, we define the global velocity and pressure spaces for micro- and macrotriangulations. For the microtriangulation $\mathcal{T}_h$ we use the standard finite element spaces

$$\begin{aligned} \boldsymbol{V}_h &:= \{\boldsymbol{u} \in \boldsymbol{V} \,:\, \boldsymbol{u}|_T \in \mathcal{P}^2 \quad \forall\, T \in \mathcal{T}_h\} \\ L_h &:= \{p \in L_0^2(\Omega) \,:\, p|_T \in \mathcal{P}^0 \quad \forall\, T \in \mathcal{T}_h\} \end{aligned} \tag{5.1.36}$$

and for the macrotriangulation $\mathcal{T}_M$

$$\begin{aligned} \boldsymbol{V}_M &:= \{\boldsymbol{u} \in \boldsymbol{V} \,:\, \boldsymbol{u}|_M \in \mathcal{Q}^2 \quad \forall\, M \in \mathcal{T}_M\} \\ L_M &:= \{p \in L_0^2(\Omega) \,:\, p|_M \in \mathcal{P}^0 \quad \forall\, M \in \mathcal{T}_M\} \end{aligned} \tag{5.1.37}$$

where $\mathcal{Q}^2$ is the standard space of piecewise biquadratic functions.

The macrotriangulation is isotropic and therefore the pair $(\boldsymbol{V}_M, L_M)$ satisfies the *inf-sup* condition with a constant independent of the diameter h_M of the patch M. But in our case $\boldsymbol{V}_M$ is not a subset of $\boldsymbol{V}_h$.

For the definition of the subspace we follow closely Apel and Nicaise [90]. For that we define the space of the Bernardi-Fortin-Raugel elements which is introduced in [93] as

follows:

$$\boldsymbol{V}_h^{BFR} := \{\boldsymbol{u} \in \boldsymbol{V} \,:\, \boldsymbol{u}|_T \in [\mathcal{P}_1]^2 \oplus span\{\boldsymbol{n}^1\lambda_2\lambda_3, \boldsymbol{n}^2\lambda_3\lambda_1, \boldsymbol{n}^3\lambda_1\lambda_2\} \quad \forall\, T \in \mathcal{T}_h\},$$

where $\boldsymbol{n}^i = (n_1^i, n_2^i)^T, i = 1, 2, 3$ are the corresponding outward unit normals and λ_i are the affine nodal basis functions in barycentric coordinates, for illustration see Figure 5.13. To

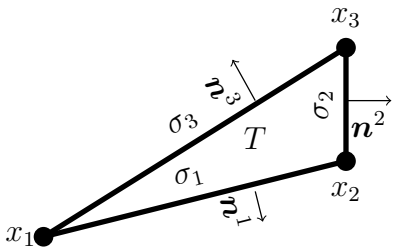

Figure 5.13: Illustration of the notation for triangular element T.

define a subspace, we introduce a projection $P_M^h : \boldsymbol{V}_M \to \boldsymbol{V}_h^{BFR} \subset \boldsymbol{V}_h$. This projection operator is defined locally on each triangle T of each macroelement

$$P_M^h\,|_T := P_T,$$

where

$$P_T\boldsymbol{u}(x_i) := \boldsymbol{u}(x_i), \quad \int_{\sigma_i} (P_T\boldsymbol{u} - \boldsymbol{u}) \cdot \boldsymbol{n}^i = 0, \quad i = 1, 2, 3.$$

Then, we can define the subspace $\bar{\boldsymbol{V}}_h \subset \boldsymbol{V}_h$ as follows:

$$\bar{\boldsymbol{V}}_h := P_M^h\, \boldsymbol{V}_M.$$

To show the stability of the subspace, first, we need to prove two Lemmas. We start with the stability estimate for P_T. For that we can use the interpolation results for anisotropic elements from Lemma 2.1 in [3]

$$\|\nabla^i(\boldsymbol{u}_M - N_T\,\boldsymbol{u}_M)\|_T \leq h_T^{2-i}\|\nabla^2\boldsymbol{u}_M\|_T \quad i = 0, 1, 2, \tag{5.1.38}$$

where $h_T = diam(T)$.

Lemma 5.1.8 (Stability of P_T)**.** *Let $M \in \mathcal{T}_M$ is an arbitrary macroelement. For any function $\boldsymbol{u}_M \in \boldsymbol{V}_M$, the following stability estimate holds*

$$\|\nabla P_T\,\boldsymbol{u}_M\|_T \leq c\,\left(\|\nabla\,\boldsymbol{u}_M\|_T + h_T\,\|\nabla^2\boldsymbol{u}_M\|_T\right) \quad \forall\, T \in M, \tag{5.1.39}$$

where h_T is the diameter of the triangle.

The Lemma 5.1.8 corresponds to the Lemma 3 in [90]. For the proof see Section 5 in [90]. We project on $\boldsymbol{V}_h^{BFR}$, which is a subspace of $\boldsymbol{V}_h$.

Lemma 5.1.9 (Stability of P_M^h). *The operator P_M^h is the Fortin type operator for any $\boldsymbol{u}_M \in \boldsymbol{V}_M$, such that*

$$\|\nabla P_M^h \boldsymbol{u}_M\| \leq C \|\nabla \boldsymbol{u}_M\| \tag{5.1.40}$$

$$(\nabla \cdot (\boldsymbol{u}_M - P_M^h \boldsymbol{u}_M), p_M) = 0 \quad \forall p_M \in L_M. \tag{5.1.41}$$

Proof. The stability estimate (5.1.40) follows using Lemma 5.1.8 and the inverse inequality on the patch M. Here, we use the fact that the function $\boldsymbol{u}_M$ is from the finite dimensional space. Moreover, if $h_M < C$ is small enough, it holds

$$\|\nabla P_M^h \boldsymbol{u}_M\|_M \leq c \left(\|\nabla \boldsymbol{u}_M\|_M + h_M \|\nabla^2 \boldsymbol{u}_M\|_M \right) \leq C \|\nabla \boldsymbol{u}_M\|_M.$$

The orthogonality condition (5.1.41) is obtained easily by using the fact that p_M is constant in each M. By choosing $p_M = 1$ on M and $p_M = 0$ elsewhere we get

$$\begin{aligned}(\nabla \cdot (\boldsymbol{u}_M - P_M^h \boldsymbol{u}_M), p_M) &= \int_M \nabla \cdot (\boldsymbol{u}_M - P_M^h \boldsymbol{u}_M) \,\mathrm{d}x = \sum_{T \in M} \int_T \nabla \cdot (\boldsymbol{u}_M - P_T \boldsymbol{u}_M) \,\mathrm{d}x \\ &= \sum_{T \in M} \int_{\partial T} \boldsymbol{n} \cdot (\boldsymbol{u}_M - E_T \boldsymbol{u}_M) \,\mathrm{d}s = 0.\end{aligned}$$

□

We note that the pair $(\boldsymbol{V}_M, L_M)$ is stable, since the macrotriangulation is an isotropic mesh. Therefore, there exists a Fortin type operator $\Pi_M : \boldsymbol{V} \to \boldsymbol{V}_M$ with the following properties:

$$\|\nabla \Pi_M \boldsymbol{u}\| \leq c \|\nabla \boldsymbol{u}\| \quad \forall \boldsymbol{u} \in \boldsymbol{V}, \tag{5.1.42}$$

$$(\nabla \cdot (\boldsymbol{u} - \Pi_M \boldsymbol{u}), p_M) = 0 \quad \forall p_M \in L_M, \forall \boldsymbol{u} \in \boldsymbol{V}. \tag{5.1.43}$$

Now, we define the operator $\Pi_h : \boldsymbol{V} \to \bar{\boldsymbol{V}}_h$ by

$$\Pi_h := P_M^h \Pi_M \tag{5.1.44}$$

Lemma 5.1.10 (Stability of subspace $\bar{\boldsymbol{V}}_h$). *The pair of subspaces $(\bar{\boldsymbol{V}}_h, L_M) \subset (\boldsymbol{V}_h, L_h)$ is stable. Then by Fortin lemma there exists an operator $\Pi_h : \boldsymbol{V} \to \bar{\boldsymbol{V}}_h$ with*

$$\|\nabla \Pi_h \boldsymbol{u}\| \leq c \|\nabla \boldsymbol{u}\| \quad \forall \boldsymbol{u} \in \boldsymbol{V}, \tag{5.1.45}$$

$$(\nabla \cdot (\boldsymbol{u} - \Pi_h \boldsymbol{u}), p_M) = 0 \quad \forall p_M \in L_M, \forall \boldsymbol{u} \in \boldsymbol{V}. \tag{5.1.46}$$

Proof. Using the stability estimates (5.1.40) and (5.1.42) we get easily (5.1.45), it holds

$$\|\nabla \Pi_h \boldsymbol{u}\| \leq \|\nabla (P_M^h \Pi_M \boldsymbol{u})\| \leq c \|\nabla \Pi_M \boldsymbol{u}\| \leq c \|\nabla \boldsymbol{u}\|.$$

For all piecewise constant functions $p_M \in L_M$ and for all $\boldsymbol{u} \in \boldsymbol{V}$ using the orthogonality

estimations (5.1.41) and (5.1.43) we easily get the orthogonality estimate (5.1.46), it holds

$$\begin{aligned}(\nabla \cdot (\boldsymbol{u} - \Pi_h \boldsymbol{u}),\, p_M) &= (\nabla \cdot (\boldsymbol{u} - P_M^h \Pi_M \boldsymbol{u}),\, p_M) \\ &= (\nabla \cdot (\boldsymbol{u} - \Pi_M \boldsymbol{u}),\, p_M) \,+\, (\nabla \cdot (\Pi_M \boldsymbol{u} - P_M^h \Pi_M \boldsymbol{u}),\, p_M) = 0.\end{aligned}$$

□

Now we are able to prove the stability of the pair $(\boldsymbol{V}_h, L_h)$ by using the macroelement technique [93].

5.1.6 Main result

Theorem 5.1.11. *Let the local* inf-sup *condition (5.1.35) be satisfied with a positive constant γ_M independent of the mesh size. If there exists a subspace $\bar{\boldsymbol{V}}_h$ of $\boldsymbol{V}_h$ such that the element pair $(\bar{\boldsymbol{V}}_h, L_M)$ is* inf-sup *stable with a positive constant $\bar{\gamma}_h$ independent of the mesh size, then there exists a constant $\gamma_h > 0$ such that the discrete* inf-sup *condition*

$$\inf_{p_h \in L_h(\Omega)} \sup_{\boldsymbol{u}_h \in \boldsymbol{V}_h(\Omega)} \frac{(p_h, \nabla \cdot \boldsymbol{u}_h)}{\|\nabla \boldsymbol{u}_h\| \, \|p_h\|} \geq \gamma_h \tag{5.1.47}$$

is satisfied for $(\boldsymbol{V}_h, L_h)$ independently of the mesh size.

Proof. For the proof we follow [22], see also [93]. We start with the derivation of the orthogonal decomposition of $Q_h(M)$ from the definitions (5.1.8) such that

$$Q_h(M) = L_h(M) \oplus \mathbb{R}.$$

Let $p_h \in L_h$ be arbitrary but fixed. Then we can split $p_h \in L_h$ as

$$p_h = \tilde{p}_h + \bar{p}_h, \tag{5.1.48}$$

where $\bar{p}_h \in L_M$ is the $L^2(\Omega)$-projection of p_h into L_M, i.e.

$$\bar{p}_h \mid_M = |M|^{-1} \int_M p_h \mathrm{d}x.$$

It holds

$$\tilde{p}_h|_M = p_h|_M - \bar{p}_h|_M \in L_h(M) \qquad \forall M \in \mathcal{T}_{\mathcal{M}},$$

and

$$\|p_h\|_\Omega^2 = \|\tilde{p}_h\|_\Omega^2 + \|\bar{p}_h\|_\Omega^2. \tag{5.1.49}$$

Using Lemma 5.1.1 and Remark 5.1.6 for each $\tilde{p}_M := \tilde{p}_h|_M \in L_h(M)$ there exists a function $\tilde{\boldsymbol{u}}_M := \tilde{\boldsymbol{v}}_h \mid_M \in \boldsymbol{V}_h(M)$ such that

$$(\tilde{p}_M, \nabla \cdot \tilde{\boldsymbol{u}}_M)_M = \|\tilde{p}_M\|_M^2, \quad \|\nabla \tilde{\boldsymbol{u}}_M\|_M \leq \gamma_M^{-1} \|\tilde{p}_M\|_M. \tag{5.1.50}$$

Since the pair $(\bar{\boldsymbol{V}}_h, L_M)$ satisfies (5.1.47) there exists a function $\bar{\boldsymbol{u}}_h \in \bar{\boldsymbol{V}}_h$ such that

$$(\bar{p}_h, \nabla \cdot \bar{\boldsymbol{u}}_h)_\Omega = \|\bar{p}_h\|_\Omega^2, \quad \|\nabla \bar{\boldsymbol{u}}_h\|_\Omega \leq \beta_h^{-1} \|\bar{p}_h\|_\Omega. \tag{5.1.51}$$

Now, we propose to associate with p_h in (5.1.48) the function $\boldsymbol{u}_h^\lambda \in \boldsymbol{V}_h$ by defining

$$\boldsymbol{u}_h^\lambda = \tilde{\boldsymbol{u}}_h + \lambda\, \bar{\boldsymbol{u}}_h \tag{5.1.52}$$

with some constant $\lambda > 0$. Then with (5.1.48) and (5.1.52) we have

$$\left(p_h, \nabla \cdot \boldsymbol{u}_h^\lambda\right) = (\tilde{p}_h, \nabla \cdot \tilde{\boldsymbol{u}}_h) + (\bar{p}_h, \nabla \cdot \tilde{\boldsymbol{u}}_h) + \lambda\, (\tilde{p}_h, \nabla \cdot \bar{\boldsymbol{u}}_h) + \lambda\, (\bar{p}_h, \nabla \cdot \bar{\boldsymbol{u}}_h)\,.$$

We estimate each component on the right hand side separately. Using (5.1.50) and (5.1.51) we have

- $(\tilde{p}_h, \nabla \cdot \tilde{\boldsymbol{u}}_h) = \|\tilde{p}_h\|_\Omega^2$,
- $(\bar{p}_h, \nabla \cdot \tilde{\boldsymbol{u}}_h) = 0$ since $\tilde{\boldsymbol{u}}_M$ vanishes on ∂M,
- $(\tilde{p}_h, \nabla \cdot \bar{\boldsymbol{u}}_h) \leq \sqrt{d}\, \|\tilde{p}_h\|_\Omega \|\nabla \bar{\boldsymbol{u}}_h\|_\Omega \leq \dfrac{\sqrt{d}}{\beta_h}\, \|\tilde{p}_h\|_\Omega\, \|\bar{p}_h\|_\Omega$,
- $(\bar{p}_h, \nabla \cdot \bar{\boldsymbol{u}}_h) = \|\bar{p}_h\|_\Omega^2$.

Then we obtain

$$\left(p_h, \nabla \cdot \boldsymbol{u}_h^\lambda\right) \geq \|\tilde{p}_h\|_\Omega^2 + \lambda\, \|\bar{p}_h\|_\Omega^2 - \lambda\, \frac{\sqrt{d}}{\beta_h}\, \|\tilde{p}_h\|_\Omega\, \|\bar{p}_h\|_\Omega.$$

By Young's inequality with arbitrary $\epsilon > 0$ we get

$$\|\tilde{p}_h\|_\Omega\, \|\bar{p}_h\|_\Omega \leq \epsilon\, \|\tilde{p}_h\|_\Omega^2 + \frac{1}{4\epsilon} \|\bar{p}_h\|_\Omega^2.$$

It holds

$$\left(p_h, \nabla \cdot \boldsymbol{u}_h^\lambda\right) \geq \left(1 - \frac{\epsilon\, \lambda \sqrt{d}}{\beta_h}\right)\, \|\tilde{p}_h\|_\Omega^2 + \lambda\, \left(1 - \frac{\sqrt{d}}{4\epsilon\, \beta_h}\right)\, \|\bar{p}_h\|_\Omega^2.$$

By choosing $\epsilon = \dfrac{\beta_h}{2\lambda\sqrt{d}}$ and $\lambda = \dfrac{\beta_h^2}{d}$ we have

$$\left(p_h, \nabla \cdot \boldsymbol{u}_h^\lambda\right) \geq \min\left(\frac{1}{2}, \frac{\lambda}{2}\right)\, \|p_h\|_\Omega^2. \tag{5.1.53}$$

Finally, applying (5.1.49), (5.1.50) and (5.1.51) we have

$$\|\nabla \boldsymbol{u}_h^\lambda\|_\Omega \leq \|\nabla \tilde{\boldsymbol{u}}_h\|_\Omega + \lambda\, \|\nabla \bar{\boldsymbol{u}}_h\|_\Omega \leq \gamma_M^{-1} \|\tilde{p}_h\|_\Omega + \lambda\, \beta_h^{-1} \|\bar{p}_h\|_\Omega \leq c\, \|p_h\|_\Omega, \tag{5.1.54}$$

where $c = \sqrt{\gamma_M^{-2} + \lambda^2\,\beta_h^{-2}}$.
Last two inequalities (5.1.53) and (5.1.54) give us the stability of the space $(\boldsymbol{V}_h, L_h)$. □

5.1.7 Error estimations

Lemma 5.1.12. *Let $\boldsymbol{u} \in \boldsymbol{V}$ and $S_h = S_h^1 \cup S_h^2$, where $S_h^i := \Omega_h^i \setminus \Omega_i$ is the mismatch between Ω_h^i and Ω^i, $i = 1, 2$ (see Figure 4.1). It holds*

$$\|\boldsymbol{u}\|_{S_h} \leq c\,h^{\frac{3}{2}}\,\|\boldsymbol{u}\|_{H^1(\Omega)}.$$

Further, let $\boldsymbol{u}_h \in \boldsymbol{V}_h$. It holds

$$\|\boldsymbol{u}_h\|_{H^k(S_h)} \leq c\,h\,\|\boldsymbol{u}_h\|_{H^k(\Omega)}, \quad k = 0, 1.$$

Moreover, let $I_h\boldsymbol{u} \in \boldsymbol{V}_h$ be the interpolation and $\boldsymbol{u} \in H^3(\Omega)^2$. It holds

$$\|\nabla(\boldsymbol{u} - I_h\boldsymbol{u})\|_{S_h} \leq c\,h^{\frac{3}{2}}\,\|\boldsymbol{u}\|_{H^3(\Omega)}.$$

Proof. The proofs are given in [83], see Sections 4.2.3 and 4.5.1, where this argument is given for first order. □

Now, we are ready to prove the best approximation error estimate.

Lemma 5.1.13 (Best approximation)**.** *Let $\Omega \in C^1$ and $\boldsymbol{f} \in H^1(\Omega)^2$. Let the mesh be such that no elements of type $\boldsymbol{G}$ exist. Then it holds for $(\boldsymbol{u}, p) \in H^3(\Omega)^2 \times H^1(\Omega)$ and $(\boldsymbol{u}_h, p_h) \in \boldsymbol{V_h} \times L_h$, where $\boldsymbol{V_h} \times L_h \subset \boldsymbol{V} \times L$ is an inf-sup stable finite element spaces.*

$$\|\nu^{1/2}\,\nabla(\boldsymbol{u} - \boldsymbol{u}_h)\| + \|p - p_h\| \leq c\left(\min_{\boldsymbol{\varphi}_h \in \boldsymbol{V}_h} \|\nabla(\boldsymbol{u} - \boldsymbol{\varphi}_h)\| + \min_{\phi_h \in L_h} \|p - \phi_h)\|\right) + c\,h^2\,\|\nabla^3\boldsymbol{u}\|, \tag{5.1.55}$$

where $c > 0$ is the constant depending only on the diffusion coefficient ν and on the discrete inf-sup *constant γ_h.*
Furthermore,

$$\|\boldsymbol{u} - \boldsymbol{u}_h\| \leq c\,h\left(\min_{\boldsymbol{\varphi}_h \in \boldsymbol{V}_h} \|\nabla(\boldsymbol{u} - \boldsymbol{\varphi}_h)\| + \min_{\phi_h \in L_h} \|p - \phi_h)\|\right) + c\,h^3\,\|\nabla^3\boldsymbol{u}\|. \tag{5.1.56}$$

Proof. We define $\boldsymbol{e}_u = \boldsymbol{u} - \boldsymbol{u}_h \in \boldsymbol{V}$ and $e_p = p - p_h \in L$. By subtracting (5.1.7) from (5.1.2) we have the perturbed Galerkin orthogonality

$$\begin{aligned} (\nu\nabla\boldsymbol{e}_u, \nabla\boldsymbol{\varphi}_h) - (\nabla\cdot\boldsymbol{\varphi}_h, e_p) &= \delta\nu\,(\nabla\boldsymbol{u}_h, \nabla\boldsymbol{\varphi}_h)_{S_h} + (\boldsymbol{f} - \boldsymbol{f}_h, \boldsymbol{\varphi}_h) && \forall\,\boldsymbol{\varphi}_h \in \boldsymbol{V_h} \\ (\nabla\cdot\boldsymbol{e}_u, \xi_h) &= 0 && \forall\,\xi_h \in L_h \end{aligned} \tag{5.1.57}$$

(i) First, we show the energy norm estimate for the velocity:

$$\|\nu^{1/2}\,\nabla \boldsymbol{e}_u\|^2 = (\nu\,\nabla \boldsymbol{e}_u, \nabla \boldsymbol{e}_u) - (\nabla\cdot \boldsymbol{e}_u, e_p) + (\nabla\cdot \boldsymbol{e}_u, e_p).$$

By the perturbed Galerkin orthogonality (5.1.57), we get for arbitrary $\boldsymbol{\varphi}_h \in \boldsymbol{V}_h, \quad \xi_h \in L_h$

$$\begin{aligned}\|\nu^{1/2}\,\nabla \boldsymbol{e}_u\|^2 =&(\nu\,\nabla \boldsymbol{e}_u, \nabla(\boldsymbol{u}-\boldsymbol{\varphi}_h)) - (\nabla\cdot(\boldsymbol{u}-\boldsymbol{\varphi}_h), e_p) + (\nabla\cdot \boldsymbol{e}_u, p-\xi_h)\\ &+ \delta\nu\,(\nabla \boldsymbol{u}_h, \nabla(\boldsymbol{\varphi}_h-\boldsymbol{u}_h))_{S_h} + (\boldsymbol{f}-\boldsymbol{f}_h, \boldsymbol{\varphi}_h-\boldsymbol{u}_h)\,.\end{aligned}$$

The difference $\boldsymbol{f}-\boldsymbol{f}_h$ vanishes everywhere besides on S_h:

$$(\boldsymbol{f}-\boldsymbol{f}_h, \boldsymbol{\varphi}_h-\boldsymbol{u}_h)_\Omega = (\boldsymbol{f}-\boldsymbol{f}_h, \boldsymbol{\varphi}_h-\boldsymbol{u}_h)_{S_h}.$$

It holds

$$\begin{aligned}\|\nu^{1/2}\,\nabla \boldsymbol{e}_u\|^2 \le& \|\nu^{1/2}\,\nabla \boldsymbol{e}_u\|\,\|\nu^{1/2}\,\nabla(\boldsymbol{u}-\boldsymbol{\varphi}_h)\| + \|\nabla(\boldsymbol{u}-\boldsymbol{\varphi}_h)\|\,\|e_p\|\\ &+ c(\nu)\|\nu^{1/2}\,\nabla \boldsymbol{e}_u\|\,\|p-\xi_h\|\\ &+ \delta\nu\,\|\nabla \boldsymbol{u}_h\|_{S_h}\,\|\nabla(\boldsymbol{\varphi}_h-\boldsymbol{u}_h)\|_{S_h} + \|\boldsymbol{f}-\boldsymbol{f}_h\|_{S_h}\|\boldsymbol{\varphi}_h-\boldsymbol{u}_h\|_{S_h},\end{aligned}$$

where $c(\nu)$ is the constant depending on ν. Using Lemma 5.1.12 and Poincaré inequality we get

$$\begin{aligned}\|\boldsymbol{\varphi}_h-\boldsymbol{u}_h\|_{S_h} &\le c\,h\,\|\boldsymbol{\varphi}_h-\boldsymbol{u}_h\|_\Omega \le c\,h\,\|\nabla(\boldsymbol{\varphi}_h-\boldsymbol{u}_h)\|_\Omega,\\ \|\nabla(\boldsymbol{\varphi}_h-\boldsymbol{u}_h)\|_{S_h} &\le c\,h\,\|\nabla(\boldsymbol{\varphi}_h-\boldsymbol{u}_h)\|_\Omega.\end{aligned} \tag{5.1.58}$$

By picking $\boldsymbol{\varphi}_h = I_h\boldsymbol{u}$ and inserting $\pm\boldsymbol{u}$ we obtain

$$\begin{aligned}\|\nabla(I_h\boldsymbol{u}-\boldsymbol{u}_h)\| &\le \|\nabla(\boldsymbol{u}-\boldsymbol{u}_h)\| + \|\nabla(\boldsymbol{u}-I_h\boldsymbol{u})\|\\ &\le c(\nu)\,\|\nu^{1/2}\,\nabla \boldsymbol{e}_u\| + c\,h^2\,\|\nabla^3\boldsymbol{u}\|.\end{aligned} \tag{5.1.59}$$

Similar to the discussions in Section 4 (the proof of the Theorem 4.2.5), we have

$$\|\boldsymbol{f}-\boldsymbol{f}_h\|_{S_h} \le c\,h\,\|\boldsymbol{u}\|_{H^3(\Omega_1\cup\Omega_2)}. \tag{5.1.60}$$

By inserting the solution $\pm\boldsymbol{u}$ and $\pm I_h\boldsymbol{u}$ and then using Lemma 5.1.12 and with (5.1.59) we obtain

$$\begin{aligned}\|\nabla \boldsymbol{u}_h\|_{S_h} &\le \|\nabla \boldsymbol{u}\|_{S_h} + \|\nabla(\boldsymbol{u}-I_h\boldsymbol{u})\|_{S_h} + \|\nabla(I_h\boldsymbol{u}-\boldsymbol{u}_h)\|_{S_h}\\ &\le c\,h^{3/2}\,\|\boldsymbol{u}\|_{H^2(\Omega)} + c\,h^{3/2}\,\|\boldsymbol{u}\|_{H^3(\Omega)} + c\,h\,\|\nabla(I_h\boldsymbol{u}-\boldsymbol{u}_h)\|_\Omega\\ &\le c\,h^{3/2}\,\|\boldsymbol{u}\|_{H^3(\Omega)} + c(\nu)\,h\,\|\nu^{1/2}\,\nabla \boldsymbol{e}_u\| + c\,h^3\,\|\nabla^3\boldsymbol{u}\|\\ &\le c(\nu)\,h\,\|\nu^{1/2}\,\nabla \boldsymbol{e}_u\| + c\,h^{3/2}\,\|\nabla^3\boldsymbol{u}\|.\end{aligned} \tag{5.1.61}$$

It holds with estimations (5.1.58)-(5.1.61) and Young's inequality

$$\begin{aligned}2\|\nu^{1/2}\,\nabla \boldsymbol{e}_u\|^2 \leq \frac{1}{2}\,\|\nu^{1/2}\,\nabla \boldsymbol{e}_u\|^2 + 2\,\|\nu^{1/2}\,\nabla(\boldsymbol{u}-\boldsymbol{\varphi}_h)\|^2 \\ + \epsilon^2\,\|e_p\|^2 + \frac{1}{\epsilon^2}\,\|\nabla(\boldsymbol{u}-\boldsymbol{\varphi}_h)\|^2 \\ + 2\,c(\nu)^2\,\|p-\xi_h\|^2 + \frac{1}{2}\,\|\nu^{1/2}\,\nabla \boldsymbol{e}_u\|^2 \\ + c\,(h+\tilde{\epsilon})\,\|\nu^{1/2}\,\nabla \boldsymbol{e}_u\|^2 + (c+\frac{1}{\tilde{\epsilon}})\,h^4\,\|\nabla^3\boldsymbol{u}\|^2,\end{aligned}$$

where the constants $\epsilon > 0$ and $\tilde{\epsilon} > 0$ come from Young's inequality. Then we obtain

$$\begin{aligned}\|\nu^{1/2}\,\nabla \boldsymbol{e}_u\| \leq c(\nu,\epsilon)\,\|\nabla(\boldsymbol{u}-\boldsymbol{\varphi}_h)\| + \tilde{c}_\nu\,\|p-\xi_h\| + \epsilon\,\|e_p\| \\ + c(\nu,\tilde{\epsilon})\,h^2\,\|\nabla^3\boldsymbol{u}\|.\end{aligned} \tag{5.1.62}$$

(ii) Next, we estimate the pressure error. Let $\xi_h \in L_h$ be arbitrary and $p-\xi_h \in L$, then we get

$$\|p-p_h\| \leq \|p-\xi_h\| + \|p_h-\xi_h\|. \tag{5.1.63}$$

For $p_h-\xi_h \in L_h$ we use the discrete *inf-sup* inequality and we get

$$\begin{aligned}\gamma_h\|p_h-\xi_h\| &\leq \sup_{\boldsymbol{\varphi}_h\in\boldsymbol{V}_h}\frac{(p_h-\xi_h,\nabla\cdot\boldsymbol{\varphi}_h)}{\|\nabla\boldsymbol{\varphi}_h\|} \\ &\leq \sup_{\boldsymbol{\varphi}_h\in\boldsymbol{V}_h}\frac{(e_p,\nabla\cdot\boldsymbol{\varphi}_h)}{\|\nabla\boldsymbol{\varphi}_h\|} + \sup_{\boldsymbol{\varphi}_h\in\boldsymbol{V}_h}\frac{(p-\xi_h,\nabla\cdot\boldsymbol{\varphi}_h)}{\|\nabla\boldsymbol{\varphi}_h\|}.\end{aligned} \tag{5.1.64}$$

On the first part we use (5.1.57) to replace the pressure error by the velocity error. It holds with Lemma 5.1.12

$$\begin{aligned}\sup_{\boldsymbol{\varphi}_h\in\boldsymbol{V}_h}\frac{(e_p,\nabla\cdot\boldsymbol{\varphi}_h)}{\|\nabla\boldsymbol{\varphi}_h\|} &= \sup_{\boldsymbol{\varphi}_h\in\boldsymbol{V}_h}\frac{\nu\,(\nabla\boldsymbol{e}_u,\nabla\boldsymbol{\varphi}_h) - \delta\nu\,(\nabla\boldsymbol{u}_h,\nabla\boldsymbol{\varphi}_h)_{S_h} - (\boldsymbol{f}-\boldsymbol{f}_h,\boldsymbol{\varphi}_h)}{\|\nabla\boldsymbol{\varphi}_h\|} \\ &\leq \sqrt{\nu}\sup_{\boldsymbol{\varphi}_h\in\boldsymbol{V}_h}\frac{\|\nu^{1/2}\,\nabla\boldsymbol{e}_u\|\,\|\nabla\boldsymbol{\varphi}_h\|}{\|\nabla\boldsymbol{\varphi}_h\|} \\ &\quad + \sup_{\boldsymbol{\varphi}_h\in\boldsymbol{V}_h}\frac{c\,h\,(\delta\nu\,\|\nabla\boldsymbol{u}_h\|_{S_h} + \|\boldsymbol{f}-\boldsymbol{f}_h\|_{S_h})\,\|\nabla\boldsymbol{\varphi}_h\|}{\|\nabla\boldsymbol{\varphi}_h\|} \\ &\leq \sqrt{\nu}\|\nu^{1/2}\,\nabla\boldsymbol{e}_u\| + c(\nu)h^2\|\nu^{1/2}\,\nabla\boldsymbol{e}_u\| + c_1\,h^{5/2}\|\nabla^3\boldsymbol{u}\| + c_2\,h^2\|\nabla^3\boldsymbol{u}\| \\ &\leq \bar{c}(\nu)\|\nu^{1/2}\,\nabla\boldsymbol{e}_u\| + \tilde{c}(\nu)\,h^2\|\nabla^3\boldsymbol{u}\|.\end{aligned}$$

Then we get together with the second part of (5.1.64)

$$\gamma_h\,\|p_h-\xi_h\| \leq \bar{c}(\nu)\|\nu^{1/2}\,\nabla\boldsymbol{e}_u\| + \tilde{c}(\nu)\,h^2\|\nabla^3\boldsymbol{u}\| + \|p-\xi_h\|.$$

With (5.1.63), we get the estimate for $\|e_p\|$

$$\|e_p\| \leq \gamma_h^{-1}\bar{c}(\nu)\,\|\nu^{1/2}\,\nabla \boldsymbol{e}_u\| + \left(1+\gamma_h^{-1}\right)\|p-\xi_h\| + c(\gamma_h,\nu)\,h^2\,\|\nabla^3\boldsymbol{u}\|. \tag{5.1.65}$$

(iii) By inserting estimate (5.1.65) into (5.1.62), using $\epsilon = \frac{\gamma_h}{2\bar{c}(\nu)}$, we obtain

$$\|\nu^{1/2}\,\nabla \boldsymbol{e}_u\| \leq\, c\left(\|\nabla(\boldsymbol{u}-\boldsymbol{\varphi}_h)\| + \|p-\xi_h\|\right) + c\,h^2\,\|\nabla^3\boldsymbol{u}\|,$$

which is the best-approximation estimate (5.1.55) since $\boldsymbol{\varphi}_h$ and ξ_h are arbitrary.
(iv) Now we derive the L_2 estimation for velocity. We define an adjoint problem

$$(\nu\nabla\boldsymbol{\varphi},\nabla\boldsymbol{z}) - (\nabla\cdot\boldsymbol{z},\xi) + (\nabla\cdot\boldsymbol{\varphi},q) = \|\boldsymbol{e}_u\|^{-1}\,(\boldsymbol{e}_u,\boldsymbol{\varphi}) \quad \forall\boldsymbol{\varphi}\in[H_0^1(\Omega)]^2, \forall\xi\in L_2(\Omega).$$

If the domain has a convex or smooth boundary then by Lemma 2.46 in [83] it holds

$$\|\boldsymbol{z}\|_{H^2(\Omega_1\cup\Omega_2)} + \|q\|_{H^1(\Omega_1\cup\Omega_2)} \leq c_s\,\|\|\boldsymbol{e}_u\|^{-1}\,\boldsymbol{e}_u\| = c_s.$$

We get

$$\|\boldsymbol{e}_u\| = \frac{(\boldsymbol{e}_u,\boldsymbol{e}_u)}{\|\boldsymbol{e}_u\|} = (\nu\nabla\boldsymbol{e}_u,\nabla\boldsymbol{z}) - (\nabla\cdot\boldsymbol{z},e_p) + (\nabla\cdot\boldsymbol{e}_u,q).$$

By using the perturbed Galerkin orthogonality and inserting the interpolants $I_h\boldsymbol{z}\in\boldsymbol{V}_h$ and $I_hq\in L_h$ and with (5.1.60) and (5.1.61) it follows

$$\begin{aligned}
\|\boldsymbol{e}_u\| =& (\nu\nabla\boldsymbol{e}_u,\nabla\boldsymbol{z}) - (\nabla\cdot\boldsymbol{z},e_p) + (\nabla\cdot\boldsymbol{e}_u,q)\\
=& (\nu\nabla\boldsymbol{e}_u,\nabla(\boldsymbol{z}-I_h\boldsymbol{z})) - (\nabla\cdot(\boldsymbol{z}-I_h\boldsymbol{z}),e_p) + (\nabla\cdot\boldsymbol{e}_u,(q-I_hq))\\
&+ \delta\nu(\nabla\boldsymbol{u}_h,\nabla I_h\boldsymbol{z})_{S_h} + (\boldsymbol{f}-\boldsymbol{f}_h,I_h\boldsymbol{z})\\
\leq& \nu^{1/2}\|\nu^{1/2}\,\nabla\boldsymbol{e}_u\|\,\|\nabla(\boldsymbol{z}-I_h\boldsymbol{z})\| + \|e_p\|\,\|\nabla(\boldsymbol{z}-I_h\boldsymbol{z})\|\\
&+ \|\nabla\boldsymbol{e}_u\|\,\|(q-I_hq)\|\\
&+ \left(c(\nu)\,h\,\|\nu^{1/2}\,\nabla\boldsymbol{e}_u\| + c\,h^{\frac{3}{2}}\,\|\nabla^3\boldsymbol{u}\|\right)\|\nabla I_h\boldsymbol{z}\|_{S_h}.
\end{aligned}$$

Using the adjoint interpolation (5.1.6) by adding and subtracting $\boldsymbol{z}$ and with Lemma 5.1.12 it follows

$$\|\nabla I_h\boldsymbol{z}\|_{S_h} \leq \|\nabla\boldsymbol{z}\|_{S_h} + \|\nabla(\boldsymbol{z}-I_h\boldsymbol{z})\|_{S_h} \leq c\,h^{\frac{3}{2}}\|\nabla^2\boldsymbol{z}\| + c\,h^{\frac{3}{2}}\|\nabla^3\boldsymbol{z}\| \leq c\,h^{\frac{3}{2}}\|\nabla^2\boldsymbol{z}\|.$$

Using (5.1.55) and the interpolation estimates (5.1.5) and (5.1.6), we obtain

$$\begin{aligned}\|\boldsymbol{e}_u\| \leq & c(\nu)\, h \left(\|\nu^{1/2}\, \nabla \boldsymbol{e}_u\| + \|e_p\| \right) \left(\|\nabla^2 \boldsymbol{z}\| + \|\nabla q\| \right) \\ & + \left(c(\nu)\, h^{\frac{5}{2}} \|\nu^{1/2}\, \nabla \boldsymbol{e}_u\| + c\, h^3 \|\nabla^3 \boldsymbol{u}\| \right) \left(\|\nabla^2 \boldsymbol{z}\| + \|\nabla q\| \right) \\ \leq & c(\nu)\, c_s\, h \left(\min_{\boldsymbol{\varphi}_h \in \boldsymbol{V}_h} \|\nabla(\boldsymbol{u} - \boldsymbol{\varphi}_h)\| + \min_{\phi_h \in Q_h} \|p - \phi_h)\| \right) + c(\nu)\, c_s\, h^3\, \|\nabla^3 \boldsymbol{u}\|.\end{aligned}$$

□

Theorem 5.1.14 (A priori estimate)**.** *Let $\boldsymbol{u} \in H^3(\Omega)^2$ and $p \in H^1(\Omega)$ be solutions of the Stokes interface problem (5.1.2). Let the mesh be such that no elements of type $\boldsymbol{G}$ exist. For the locally parametric $\mathcal{P}_2 - \mathcal{P}_0$ solution $\boldsymbol{u}_h \in \boldsymbol{V}_h$ and $p_h \in L_h$ it holds*

$$\begin{aligned}\|\nu^{1/2}\, \nabla(\boldsymbol{u} - \boldsymbol{u_h})\| + \|p - p_h\| &\leq c\, h \left(\|\nabla^3 \boldsymbol{u}\| + \|\nabla p\| \right) \\ \|\boldsymbol{u} - \boldsymbol{u_h}\| &\leq c\, h^2 \left(\|\nabla^3 \boldsymbol{u}\| + \|\nabla p\| \right),\end{aligned}$$

where $c > 0$ is the constant depending only on the diffusion coefficient ν and on the discrete inf-sup *constant γ_h.*

Proof. By Lemma 5.1.13 we have

$$\begin{aligned}\|\nu^{1/2}\, \nabla(\boldsymbol{u} - \boldsymbol{u_h})\| + \|p - p_h\| &\leq c \left(\|\nabla\left(\boldsymbol{u} - I_h \boldsymbol{u}\right)\| + \|p - I_h p\| \right) + c\, h^2\, \|\nabla^3 \boldsymbol{u}\|, \\ \|\boldsymbol{u} - \boldsymbol{u_h}\| &\leq c\, h \left(\|\nabla\left(\boldsymbol{u} - I_h \boldsymbol{u}\right)\| + \|p - I_h p\| \right) + c\, h^3\, \|\nabla^3 \boldsymbol{u}\|,\end{aligned}$$

where $I_h \boldsymbol{u} \in \boldsymbol{V}_h$ and $I_h p \in L_h$ are the nodal interpolations. By interpolation estimates (5.1.5) and (5.1.6) and with given sufficient regularity it holds

$$\|\nabla(\boldsymbol{u} - I_h \boldsymbol{u})\| \leq \tilde{c}\, h^2\, \|\nabla^3 \boldsymbol{u}\|, \quad \|p - I_h p\| \leq \tilde{c}\, h\, \|\nabla p\|.$$

The last inequalities complete the a priori error estimates. □

5.1.8 Numerical examples

We consider a square domain Ω. The domain is split into two domains Ω_1 and Ω_2 by the interface Γ. The interface is defined as $\Gamma = \{(x, y) \in \Omega \,|\, l(x, y) = 0\}$ with the level-set function $l(x, y)$. In Figure 5.14 we show the configuration for our numerical examples.

Example 1.

In this example, we show instability of type **G**. We compare the maximum-norm for pressure error in the coarse mesh before and after the stabilization.

Let $\Omega = [-1, 1]^2$ be a square domain. We consider Stokes problem with $\nu = 1$ and a

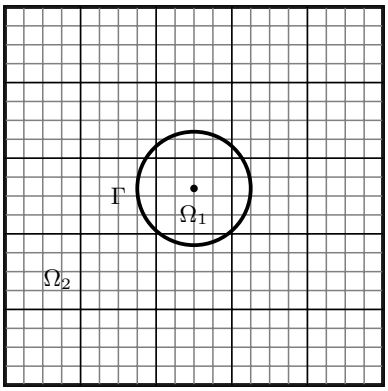

Figure 5.14: Configuration of the test problems with $\Omega = \Omega_1 \cup \Gamma \cup \Omega_2$.

do-nothing condition on the left and Dirichlet boundary condition on the right, upper and lower. An analytical solution is given by

$$\begin{aligned} u_1(x,y) &= \sin(\pi x) \cdot \cos(\pi y), \\ u_2(x,y) &= -\cos(\pi x) \cdot \sin(\pi y), \\ p(x,y) &= 2\pi \cos(\pi x) \cdot \cos(\pi y), \end{aligned}$$

and define a right-hand side as $f = -\nu\Delta u + \nabla p$ and Dirichlet boundary data. We define the the level-set function $l(x,y) = x^2 + y^2 - r^2$, with a given radius r.
Figure 5.15 shows us the discrete pressure profile in the coarse mesh with the circle radius $r = 10^{-3}$. We observe the instability of the pressure. As shown in Table 5.1 (Left) the maximum-norms of the pressure error grows very quickly when $r \leq 10^{-3}$, which means that there are some spurious pressures in the discrete solution. This is the reason for instability. This instability was corrected numerically by stabilising of the small edges γ_1 and γ_2 with (5.1.34). In the Table 5.1 we show the maximum-norms of the pressure error before and after the stabilization.

r	$\|p - p_h\|_{l^\infty}$
10^{-1}	2.40484
10^{-2}	2.40484
10^{-3}	11.5363
10^{-4}	84.3159
10^{-5}	102.416
10^{-6}	102.645
10^{-7}	102.648

r	$\|p - p_h\|_{l^\infty}$
10^{-1}	2.40484
10^{-2}	2.40484
10^{-3}	5.44222
10^{-4}	5.46533
10^{-5}	5.78036
10^{-6}	5.78100
10^{-7}	5.78101

Table 5.1: Maximum-norm for pressure error in the coarse mesh. Left: before stabilization. Right: after stabilization

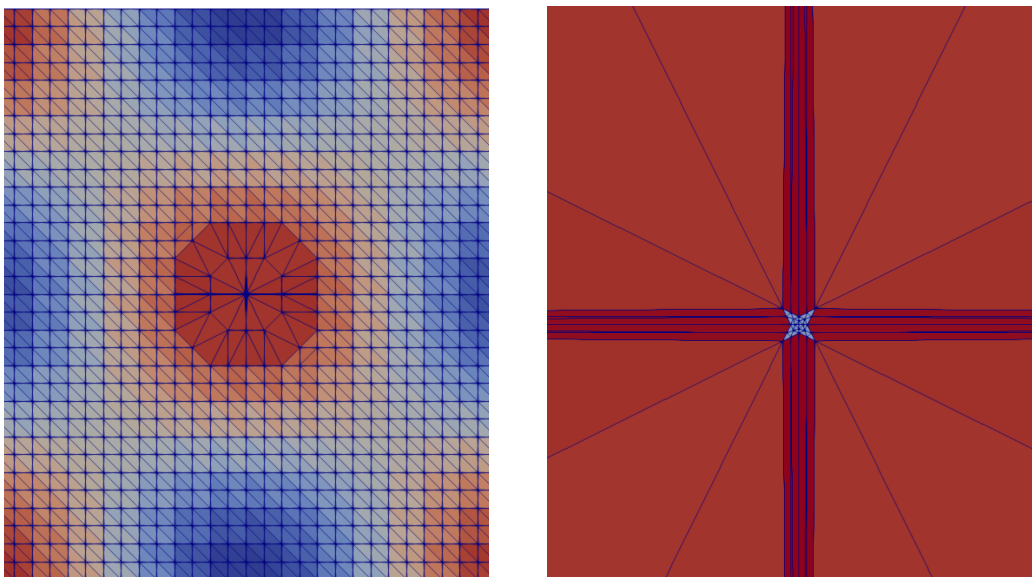

Figure 5.15: The circle with radius $r = 10^{-3}$. Left: pressure in the coarse mesh. Right: zoom of the middle cells.

Example 2.

In this example, we show the robustness of the interface discretization. Thus we consider the Stokes problem with constant viscosity coefficients in each subdomain.

Let $\Omega = [-1, 1]^2$ be a square domain. We consider the Stokes problem with $\nu_1 = \nu_2 = 1$ and a do-nothing condition on the right and Dirichlet boundary condition on the left, upper and lower boundaries. Analytical solutions are given as follows

$$\begin{aligned} u_1(x, y) &= 4l(x, y)(x - 1)^3(y - y_0), \\ u_2(x, y) &= -4l(x, y)(x - 1)^3(x - x_0) - 3l(x, y)^2(x - 1)^2, \\ p(x, y) &= 8(x - x_0)(x - 1)^3(y - y_0) + 12l(x, y)(x - 1)^2(y - y_0), \end{aligned}$$

where $l(x, y) = (x - x_0)^2 + (y - y_0)^2 - r^2$ is the level-set function. We set $(x_0, y_0) = (0, 0)$ and $r = 0.4$. We define a right-hand side $f = -\nu\Delta u + \nabla p$ and Dirichlet boundary data on the left, upper and lower.

According to the a priori error estimate in Lemma 5.1.14, we observe first order in the energy norm and quadratic convergence in the L^2-norm for velocity and first order convergence in the L^2-norm for pressure, see Table 5.2.

Example 3.

Let $\Omega = (-1, 1)^2$ be a square domain. We consider the Stokes interface problem with $\nu_1 = 0.5$ and $\nu_2 = 20$ and Dirichlet boundary condition on the boundary. The level-set

h	$\|\boldsymbol{u}-\boldsymbol{u}_h\|_{L^2}$	EOC	$\|\nabla(\boldsymbol{u}-\boldsymbol{u}_h)\|_{L^2}$	EOC	$\|p-p_h\|_{L^2}$	EOC
1/16	$8.48 \cdot 10^{-3}$	-	$4.36 \cdot 10^{-1}$	-	$1.22 \cdot 10^{0}$	-
1/32	$2.20 \cdot 10^{-3}$	1.94	$2.20 \cdot 10^{-1}$	0.98	$6.07 \cdot 10^{-1}$	1.00
1/64	$5.60 \cdot 10^{-4}$	1.97	$1.11 \cdot 10^{-1}$	0.99	$3.03 \cdot 10^{-1}$	1.00

Table 5.2: Errors in the L^2 norm of pressure and $\boldsymbol{u}$ and energy norm and order of convergence.

function defined as $l(x,y) = (x-x_0)^2 + (y-y_0)^2 - r^2$ with $(x_0, y_0) = (0,0)$ and $r = 1/\sqrt{\pi}$. We choose the exact solutions as follows:

$$\boldsymbol{u}(x,y) = \begin{cases} \frac{l(x,y)}{\nu_1} \begin{pmatrix} y \\ -x \end{pmatrix} & \text{in } \Omega_1, \\ \\ \frac{l(x,y)}{\nu_2} \begin{pmatrix} y \\ -x \end{pmatrix} & \text{in } \Omega_2, \end{cases}$$

$$p(x,y) = y^2 - x^2$$

The error norms and experimental rates are shown in Table 5.3. According to the Lemma 5.1.14, we observe first order in the energy norm and quadratic convergence in the L^2-norm for velocity and first order convergence in the L^2-norm for pressure.

h	$\|\boldsymbol{u}-\boldsymbol{u}_h\|_{L^2}$	EOC	$\|\nu^{1/2}\nabla(\boldsymbol{u}-\boldsymbol{u}_h)\|_{L^2}$	EOC	$\|p-p_h\|_{L^2}$	EOC
1/16	$1.44 \cdot 10^{-4}$	-	$7.01 \cdot 10^{-3}$	-	$4.92 \cdot 10^{-2}$	-
1/32	$5.09 \cdot 10^{-5}$	1.50	$3.78 \cdot 10^{-3}$	0.89	$2.44 \cdot 10^{-2}$	1.01
1/64	$1.05 \cdot 10^{-5}$	2.26	$1.78 \cdot 10^{-3}$	1.08	$1.21 \cdot 10^{-2}$	1.00

Table 5.3: Errors in the L^2 norm of pressure and $\boldsymbol{u}$ and energy norm. Also the order of convergence.

Furthermore, we will show that the errors $\|\boldsymbol{u}-\boldsymbol{u}_h\|_{L^2}$, $\|\nu^{1/2}\nabla(\boldsymbol{u}-\boldsymbol{u}_h)\|_{L^2}$ and $\|p-p_h\|_{L^2}$ are independent of ν. For that we compute the errors experimentally, with fixed $\nu_1 = 0.5$ and increasing values of $\nu_2 = 200, 2000, 20000$. The numerical results for the errors with fixed mesh size $h = 0.03125$ are summarized in Table 5.4. From Table 5.4, we observe that remain unchanged for a fixed mesh when ν_2 increases.

Example 4.

Let $\Omega = (-1,1)^2$ be a square domain. We consider the Stokes interface problem with $\nu_1 = 1$ and $\nu_2 = 10$ and Dirichlet boundary condition on the boundary. The level-set function is defined as $l(x,y) = (x-x_0)^4 + (y-y_0)^4 - r$ with $(x_0, y_0) = (0,0)$ and $r = 0.1$.

ν_2	$\|\boldsymbol{u}-\boldsymbol{u}_h\|_{L^2}$	$\|\nu^{1/2}\nabla(\boldsymbol{u}-\boldsymbol{u}_h)\|_{L^2}$	$\|p-p_h\|_{L^2}$
200	$5.11\cdot10^{-5}$	$3.32\cdot10^{-3}$	$2.44\cdot10^{-2}$
2000	$5.11\cdot10^{-5}$	$3.32\cdot10^{-3}$	$2.44\cdot10^{-2}$
20000	$5.11\cdot10^{-5}$	$3.32\cdot10^{-3}$	$2.44\cdot10^{-2}$

Table 5.4: Errors are shown for a fixed mesh $h = 0.03125$ and fixed value $\nu_1 = 0.5$ and increasing values of ν_2.

We choose the exact solutions as follows:

$$\boldsymbol{u}(x,y) = \begin{cases} \frac{\sin(l(x,y))}{\nu_1}\begin{pmatrix} y^3 \\ -x^3 \end{pmatrix} & \text{in } \Omega_1, \\ \\ \frac{\sin(l(x,y))}{\nu_2}\begin{pmatrix} y^3 \\ -x^3 \end{pmatrix} & \text{in } \Omega_2, \end{cases}$$

$$p(x,y) = \frac{1}{10}\cdot(x^3 - y^3)$$

As shown in Table 5.5 (top), we observe for this example almost second order in energy norm and almost third order convergence in the L^2-norm for velocity and first order convergence in the L^2-norm for pressure. Furthermore, we consider this example by setting $p = 0$. As shown in Table 5.5 (bottom), we observe in this case almost second order in energy norm and a bit more than cubic convergence in the L^2-norm for velocity.

h	$\|\boldsymbol{u}-\boldsymbol{u}_h\|_{L^2}$	EOC	$\|\nu^{1/2}\nabla(\boldsymbol{u}-\boldsymbol{u}_h)\|_{L^2}$	EOC	$\|p-p_h\|_{L^2}$	EOC
1/16	$9.60\cdot10^{-6}$	-	$2.87\cdot10^{-3}$	-	$3.15\cdot10^{-3}$	-
1/32	$3.37\cdot10^{-6}$	1.50	$8.09\cdot10^{-4}$	1.82	$1.59\cdot10^{-3}$	0.98
1/64	$4.38\cdot10^{-7}$	2.94	$2.14\cdot10^{-4}$	1.91	$7.92\cdot10^{-4}$	1.00

h	$\|\boldsymbol{u}-\boldsymbol{u}_h\|_{L^2}$	EOC	$\|\nu^{1/2}\nabla(\boldsymbol{u}-\boldsymbol{u}_h)\|_{L^2}$	EOC
1/16	$8.87\cdot10^{-6}$	-	$2.84\cdot10^{-3}$	-
1/32	$2.97\cdot10^{-6}$	1.57	$7.82\cdot10^{-4}$	1.863
1/64	$2.88\cdot10^{-7}$	3.367	$1.90\cdot10^{-5}$	2.041

Table 5.5: Top: Errors in the L^2 - and energy-norm of velocity and the errors in the L^2-norm of pressure. Bottom: Errors in the L^2 - and energy-norm errors of velocity for the case when $p = 0$. Also the order of convergence.

Example 5.

In this example, we show the robustness of the interface discretization by moving the middle point of the circle horizontally.

Let $\Omega = (-1,1)^2$ be a square domain. We consider the Stokes interface problem with

$\nu_1 = 1$ and $\nu_2 = 10$ and Dirichlet boundary condition on the boundary. The level-set function defined as $l(x,y) = r^2 - (x-x_0)^2 + (y-y_0)^2$ with $r = \sqrt{0.3}$ and $(x_0, y_0) = (\epsilon h, 0)$, where $\epsilon \in [0,1]$ and h is the mesh size. We choose the exact solutions as follows:

$$\boldsymbol{u}(x,y) = \begin{cases} \frac{l(x,y)^2}{\nu_1} \begin{pmatrix} y \\ x_0 - x \end{pmatrix} & \text{in } \Omega_1, \\ \\ \frac{l(x,y)^2}{\nu_2} \begin{pmatrix} y \\ x_0 - x \end{pmatrix} & \text{in } \Omega_2, \end{cases}$$

$$p(x,y) = \frac{1}{10} \cdot (x^3 - y^3)$$

We vary $\epsilon \in [0,1]$, such that this example includes different configurations with arbitrary anisotropies. According to the Lemma 5.1.14, we observe first order in the energy -norm and quadratic convergence in the L^2-norm for velocity and first order in the L^2-norm for pressure. We show these for the case when $\epsilon = 0$ in Table 5.6.

h	$\|\boldsymbol{u} - \boldsymbol{u}_h\|_{L^2}$	EOC	$\|\nu^{\frac{1}{2}} \nabla(\boldsymbol{u} - \boldsymbol{u}_h)\|_{L^2}$	EOC	$\|p - p_h\|_{L^2}$	EOC
1/16	$1.37 \cdot 10^{-4}$	-	$1.30 \cdot 10^{-2}$	-	$6.38 \cdot 10^{-3}$	-
1/32	$2.49 \cdot 10^{-5}$	2.46	$3.76 \cdot 10^{-3}$	1.79	$3.17 \cdot 10^{-3}$	1.00
1/64	$5.56 \cdot 10^{-6}$	2.16	$1.34 \cdot 10^{-3}$	1.48	$1.58 \cdot 10^{-3}$	1.00

Table 5.6: The errors and the convergence orders for the case when $\epsilon = 0$.

Moreover, we consider this example with the exact pressure solution as $p = 0$. In this case we observe second order in the energy norm and cubic convergence in the L^2-norm for velocity, see Table 5.7.

Furthermore, in Figures 5.16 and 5.17, we plot the L^2- and energy norm errors for

h	$\|\boldsymbol{u} - \boldsymbol{u}_h\|_{L^2}$	EOC	$\|\nu^{\frac{1}{2}} \nabla(\boldsymbol{u} - \boldsymbol{u}_h)\|_{L^2}$	EOC
1/16	$1.09 \cdot 10^{-4}$	-	$1.22 \cdot 10^{-2}$	-
1/32	$1.35 \cdot 10^{-5}$	3.019	$3.05 \cdot 10^{-3}$	2.006
1/64	$1.70 \cdot 10^{-6}$	2.992	$7.64 \cdot 10^{-4}$	1.997

Table 5.7: The errors and the convergence orders for the case when $\epsilon = 0$ and $p = 0$.

$\epsilon \in [0,1]$ on several levels of global mesh refinement and observe that the errors are bounded independently of ϵ.

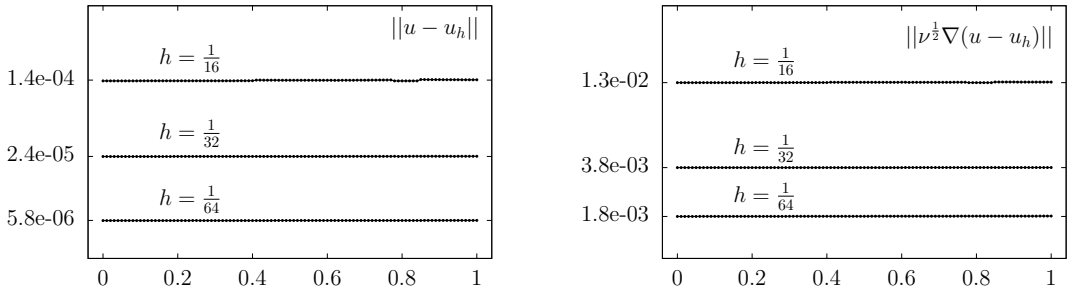

Figure 5.16: L^2 and energy - norm errors for velocity with $x = \epsilon h$ and $\epsilon \in [0, 1]$.

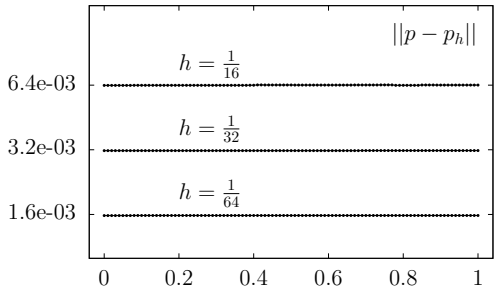

Figure 5.17: L^2 - norm error for pressure with $x = \epsilon h$ and $\epsilon \in [0, 1]$.

5.2 Stokes interface problem with surface tension

In this section, we investigate the Stokes interface problem (2.3.1) with surface tension. We consider the following model problem

$$\begin{aligned} -\nabla \cdot (\nu_i \nabla \boldsymbol{u}) + \nabla p = \boldsymbol{f}, \qquad \nabla \cdot \boldsymbol{u} = \boldsymbol{0} \qquad & \text{in} \quad \Omega_i, \quad i = 1, 2 \\ [\![\boldsymbol{u}]\!] = \boldsymbol{0}, \qquad [\![(\nu \nabla \boldsymbol{u} - p\,\mathbb{I})\ \boldsymbol{n}]\!] = \tau\, \mathcal{K}\, \boldsymbol{n} \qquad & \text{on} \quad \Gamma, \\ \boldsymbol{u} = \boldsymbol{0} \qquad & \text{on} \quad \partial\Omega, \end{aligned} \tag{5.2.1}$$

where $[\![w]\!] := (w|_{\Omega_2})|_\Gamma - (w|_{\Omega_1})|_\Gamma$ and τ is the surface tension coefficient, $\mathcal{K}$ is the curvature of Γ, and $\boldsymbol{n}$ is the unit normal at the interface Γ pointing from Ω_1 to Ω_2.
We define the spaces as follows:

$$\boldsymbol{V} = H_0^1(\Omega)^2, \quad L := \left\{ q \in L^2(\Omega) : \quad \int_\Omega \nu^{-1} q \,\mathrm{d}x = 0 \right\}.$$

The weak form is: find $(\boldsymbol{u}, p) \in \boldsymbol{V} \times L$ such that

$$\begin{aligned} (\nu \nabla \boldsymbol{u}, \nabla \boldsymbol{\varphi})_\Omega \ - \ (\nabla \cdot \boldsymbol{\varphi}, p)_\Omega \ + \ (\nabla \cdot \boldsymbol{u}, \phi)_\Omega \ = \ (\boldsymbol{f}, \boldsymbol{\varphi})_\Omega \ + \ \langle \tau\, \mathcal{K}\, \boldsymbol{n}, \boldsymbol{\varphi} \rangle_\Gamma \\ \forall\, (\boldsymbol{\varphi}, \phi) \in \boldsymbol{V} \times L. \end{aligned} \tag{5.2.2}$$

5.2.1 The effects of different curvature handling

CASE I: The curvature is known

For simplicity we take $\boldsymbol{f} = \mathbf{0}$ in (5.2.2). Then we get the following weak form:

Find $(\boldsymbol{u}, p) \in \boldsymbol{V} \times L$ such that

$$\begin{aligned}(\nu\,\nabla\boldsymbol{u}, \nabla\boldsymbol{\varphi})_\Omega \;-\; (\nabla\cdot\boldsymbol{\varphi}, p)_\Omega \;+\; (\nabla\cdot\boldsymbol{u}, \phi)_\Omega \;-\; \tau\,\langle\mathcal{K}, \boldsymbol{n}\cdot\boldsymbol{\varphi}\rangle_\Gamma = \mathbf{0} \\ \forall\,(\boldsymbol{\varphi}, \phi) \in \boldsymbol{V} \times L.\end{aligned} \tag{5.2.3}$$

For discretization, we use the locally modified finite element pair $\mathcal{P}_2 - \mathcal{P}_0$ and get the following discrete problem:

Find $(\boldsymbol{u}_h, p_h) \in \boldsymbol{V}^h \times L^h$ such that

$$\begin{aligned}(\nu\,\nabla\boldsymbol{u}_h, \nabla\boldsymbol{\varphi}_h)_{\Omega^h} \;-\; (\nabla\cdot\boldsymbol{\varphi}_h, p_h)_{\Omega^h} \;+\; (\nabla\cdot\boldsymbol{u}_h, \phi_h)_{\Omega^h} \;-\; \tau\,\langle\mathcal{K}_h, \boldsymbol{n}\cdot\boldsymbol{\varphi}_h\rangle_{\Gamma_h} = \mathbf{0} \\ \forall\,(\boldsymbol{\varphi}_h, \phi_h) \in \boldsymbol{V}^h \times L^h\end{aligned} \tag{5.2.4}$$

CASE II: The curvature is unknown

In this case, we use the technique which is introduced by Dziuk, i.e. integration by part of the Laplace-Beltrami operator. The advantage of using this approach is that there is no need to compute the curvature. We will use the identity

$$\Delta_\Gamma\,\mathrm{id}_\Gamma = \nabla_\Gamma\cdot(\nabla_\Gamma\,\mathrm{id}_\Gamma) = \mathcal{K}\,\boldsymbol{n},$$

where $\mathrm{id}_\Gamma : \Gamma \to \Gamma$ is the identity mapping on Γ. Δ_Γ is the Laplace-Beltrami operator and ∇_Γ is the tangential derivative. We note that a normal defined as follows

$$\boldsymbol{n} = \frac{\nabla\,l(x,y)}{\|\nabla\,l(x,y)\|},$$

where $l(x,y)$ is the level-set function. With an orthogonal projection

$$\mathbb{P} := \mathbb{I} - \boldsymbol{n}\boldsymbol{n}^T,$$

the tangential derivative, for a sufficiently smooth function $\eta : U \to \mathbb{R}^2$ with open subset U which containes Γ, can be written as follows:

$$\nabla_\Gamma\eta = (\mathbb{I} - \boldsymbol{n}\boldsymbol{n}^T)\,\nabla\eta = \mathbb{P}\,\nabla\eta. \tag{5.2.5}$$

Since Γ is closed, we can use the integration by parts and we get

$$\langle \tau \mathcal{K} \boldsymbol{n}, \boldsymbol{\varphi} \rangle_\Gamma = \tau \langle \nabla_\Gamma \cdot (\nabla_\Gamma \mathrm{id}_\Gamma), \boldsymbol{\varphi} \rangle_\Gamma = -\tau \langle \nabla_\Gamma \mathrm{id}_\Gamma, \nabla_\Gamma \boldsymbol{\varphi} \rangle_\Gamma .$$

Then the weak form of (5.2.1) is:
Find $(\boldsymbol{u}, p) \in \boldsymbol{V} \times L$ such that

$$\begin{aligned} (\nu \nabla \boldsymbol{u}, \nabla \boldsymbol{\varphi})_\Omega - (\nabla \cdot \boldsymbol{\varphi}, p)_\Omega + (\nabla \cdot \boldsymbol{u}, \phi)_\Omega = -\tau \langle \nabla_\Gamma \mathrm{id}_\Gamma, \nabla_\Gamma \boldsymbol{\varphi} \rangle_\Gamma \\ \forall (\boldsymbol{\varphi}, \phi) \in \boldsymbol{V} \times L. \end{aligned} \tag{5.2.6}$$

We can rewrite the right hand side by using (5.2.5) as:

$$-\tau \langle \nabla_\Gamma \mathrm{id}_\Gamma, \nabla_\Gamma \boldsymbol{\varphi} \rangle_\Gamma = -\tau \langle \mathbb{P} \nabla \mathrm{id}_\Gamma, \nabla_\Gamma \boldsymbol{\varphi} \rangle_\Gamma$$

After discretising (5.2.6) in $\boldsymbol{V}^h \times L^h$ we get a discrete problem:

Find $(\boldsymbol{u}_h, p_h) \in \boldsymbol{V}^h \times L^h$ such that

$$\begin{aligned} (\nu \nabla \boldsymbol{u}_h, \nabla \boldsymbol{\varphi}_h)_{\Omega^h} - (\nabla \cdot \boldsymbol{\varphi}_h, p_h)_{\Omega^h} + (\nabla \cdot \boldsymbol{u}_h, \phi_h)_{\Omega^h} = -\tau \langle \mathbb{P}_h \nabla \mathrm{id}_{\Gamma_h}, \nabla_{\Gamma_h} \boldsymbol{\varphi}_h \rangle_{\Gamma_h} \\ \forall (\boldsymbol{\varphi}_h, \phi_h) \in \boldsymbol{V}^h \times L^h, \end{aligned} \tag{5.2.7}$$

where the identity id_{Γ_h} is the coordinate vector on Γ_h. $\mathbb{P}_h$ is a discrete analogue of the of the orthogonal projection $\mathbb{P}$ and it is defined as

$$\mathbb{P}_h := \mathbb{I} - \boldsymbol{n}_h \boldsymbol{n}_h^T,$$

here $\boldsymbol{n}_h$ is the pieceweise constant outward unit normal on Γ_h.
In this case, the curvature term is unknown, therefore, the source for the velocity error is the approximation of the pressure and the curvature, see (5.2.8).

5.2.2 Numerical experiment

This example was taken from [55]. Let $\Omega = (-2, 2)^2 \subset \mathbb{R}^2$ and the interface $\Gamma := \{(x, y) \in \Omega : l(x, y) = 0\}$, and $\Omega_2 := \Omega \setminus (\Omega_1 \cup \Gamma)$. In the calculations we use $\tau = 1$, $\nu_1 = \nu_2 = 1$, $\boldsymbol{f} = \boldsymbol{0}$. The exact solutions of (2.3.1) are known as follows:

$$\begin{aligned} \boldsymbol{u}_{ex} &\equiv \boldsymbol{0} \quad \text{in} \quad \Omega, \\ p_{ex} &= \begin{cases} \frac{\pi}{16} - 1 & \text{in} \quad \Omega_1, \\ \frac{\pi}{16} & \text{in} \quad \Omega_2. \end{cases} \end{aligned}$$

We define the interface as follows:

$$\Gamma := \{(x, y) \in \Omega \ : \ (x - x_0)^2 + (y - y_0)^2 - r^2 = 0\}.$$

The curvature of circle is a constant function, $\mathcal{K} = \frac{1}{r}$. We take $(x_0, y_0) = (0, 0)$ and $r = 1$. For our numerical example we have the error bound

$$\|\nu^{1/2}\nabla \boldsymbol{u}_h\| + \|p - p_h\| \leq c \left(\min_{\phi_h \in Q_h} \|p - \phi_h\| + \sup_{\boldsymbol{\varphi}_h \in \boldsymbol{V}_h} \frac{|\langle \mathcal{K}_h, \boldsymbol{\varphi}_h \cdot \boldsymbol{n} \rangle - \langle \mathcal{K}, \boldsymbol{\varphi}_h \cdot \boldsymbol{n} \rangle|}{\|\nabla \boldsymbol{\varphi}_h\|} \right) \quad (5.2.8)$$

We see from 5.2.8 that the size of the non-physical or spurious velocities depends on the approximation of the pressure and the curvature.
In this case, the curvature term is handled exactly, therefore, the only source for the velocity error is the approximation of the pressure, see (5.2.8).
With the *locally modified finite element* method we observe that the numerical solution of the velocity is zero, i.e., no spurious velocities (or very small) are generated, see Figure 5.18. As shown in the Table 5.8 the pressure error is very small, i.e. our discretization gives the best result which is almost exact. Moreover, we consider l^∞-norm errors of pressure, see Table 5.8. We observe that there is no spurious pressure in numerical solution.

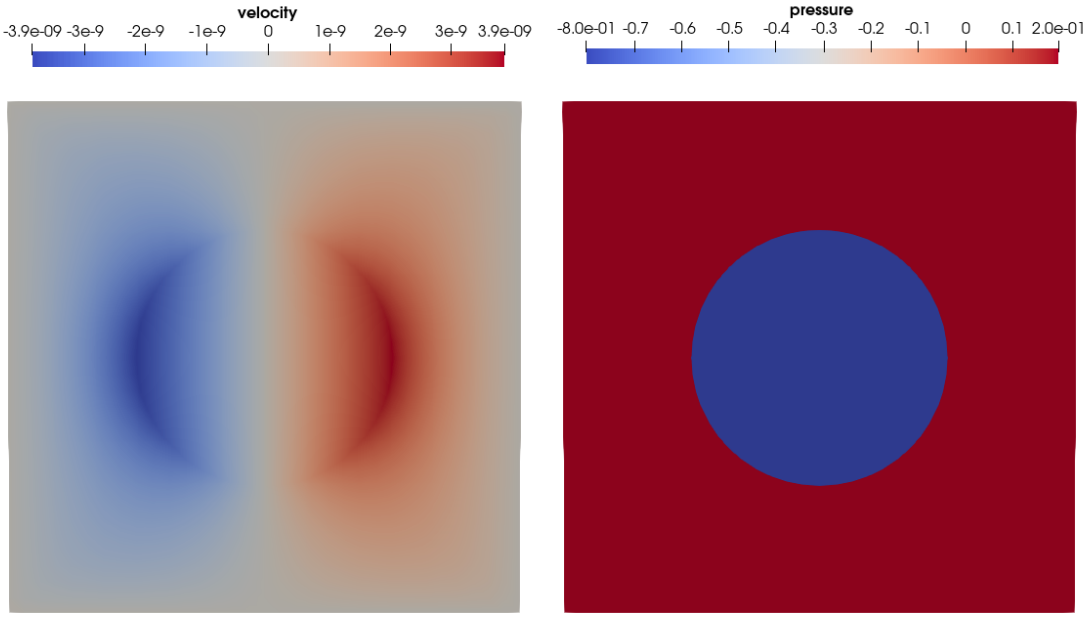

Figure 5.18: The velocity(left) and pressure(right) profiles

h	$\|p - p_h\|_{L^2}$	$\|p - p_h\|_{l^\infty}$
1/8	$3.86 \cdot 10^{-6}$	$1.94 \cdot 10^{-6}$
1/16	$5.04 \cdot 10^{-7}$	$2.67 \cdot 10^{-7}$
1/32	$4.36 \cdot 10^{-8}$	$3.80 \cdot 10^{-8}$
1/64	$1.68 \cdot 10^{-8}$	$2.14 \cdot 10^{-8}$

Table 5.8: Errors in the L^2 - and l^∞-norm errors of pressure

5.3 Two-phase Stokes problem

Compared to one-phase flows, two-phase flows with a surface tension forces have very high numerical complexity. Among them are:

- due to the unknown interface the flow problem is nonlinear;
- the surface tension force is localized at the interface which is unknown;
- the pressure and viscosity have a jump across the interface.

To handle these issues, we need a special numerical method. As mentioned above, we use the numerical method which combines an Eulerian approach with semi-implicit time integration of the surface tension force. We will use the Rothe method. Because of the third issure the pressure is discontinuous across the interface, in a finite element discretization for the Stokes problem we should use a pressure finite element space that is time dependent. Therefore, the Rothe approach is more natural than the method of lines. There is an alternative approach which is based on a space-time finite element method in literature, e.g. [13]. For time discretization, we use implicit Euler method for unsteady Stokes problem combined with a semi-implicit time integration of the surface tension force which has been developed in [12]. For space discretization, we use the locally modified finite element pair $\mathcal{P}_2 - \mathcal{P}_0$. We consider the model two phase Stokes problem on a fixed domain $\mathcal{Q} := [0, T] \times \Omega$ where only the interior interface $\Gamma(t)$ moves and the outer boundary $\partial\Omega$ is fixed, for notations see Figure 2.2

$$
\begin{aligned}
\rho_i\, \partial_t \boldsymbol{u} - \nabla \cdot (\nu_i\, \nabla \boldsymbol{u}) + \nabla p = \boldsymbol{f}, \qquad \nabla \cdot \boldsymbol{u} = \boldsymbol{0} \qquad & \text{in} \quad \mathcal{Q}_i, \quad i = 1, 2 \\
[\![\boldsymbol{u}]\!] = \boldsymbol{0}, \qquad [\![(\nu\, \nabla \boldsymbol{u} - p\, \mathbb{I})\ \boldsymbol{n}]\!] = -\tau\, \mathcal{K}\, \boldsymbol{n}, \quad \boldsymbol{u}_\Gamma = \boldsymbol{u} \cdot \boldsymbol{n} \qquad & \text{on} \quad \Gamma(t), \\
\boldsymbol{u} = \boldsymbol{0} \qquad & \text{on} \quad \partial\Omega, \\
\boldsymbol{u}(0, x) = \boldsymbol{u}_0 \qquad & \text{in} \quad \Omega,
\end{aligned}
\tag{5.3.1}
$$

where $\boldsymbol{u}_\Gamma$ is the normal velocity of the interface, and $\boldsymbol{n}$ is the unit normal at the interface which is pointing from Ω_1 into Ω_2.

5.3.1 Space-time variational vormulation

We introduce the following spaces for velocity and pressure, respectively as follows:

$$\begin{aligned} \boldsymbol{V} &:= \{\boldsymbol{v} \in H^1(\Omega)^2 \mid \boldsymbol{v} = \boldsymbol{0} \text{ on } \partial\,\Omega\}, \\ L &:= \{q \in L^2(\Omega) \mid (p,1)_\Omega = 0\}, \end{aligned}$$

and

$$\begin{aligned} \boldsymbol{X} &:= \{\boldsymbol{v} : \mathcal{Q} \mapsto \mathbb{R}^2 \mid \boldsymbol{v} \in L^2(I;\boldsymbol{V})\ ,\ \partial_t \boldsymbol{v} \in L^2(I;\boldsymbol{V'})\}, \\ Y &:= L^2(I;L), \end{aligned}$$

with a time interval I.

A variational formulation of (5.3.1) is given by:
Find $(\boldsymbol{u},p) \in \boldsymbol{X} \times Y$ such that for all $(\boldsymbol{\varphi},\phi) \in (\boldsymbol{X},Y)$ it holds

$$\begin{aligned} (\partial_t\,\boldsymbol{u},\boldsymbol{\varphi})_{\mathcal{Q}} + (\nu\,\nabla\boldsymbol{u},\nabla\boldsymbol{\varphi})_{\mathcal{Q}} - (\nabla\cdot\boldsymbol{\varphi},p)_{\mathcal{Q}} + (\boldsymbol{u}(0),\boldsymbol{\varphi}(0))_\Omega \\ = (\boldsymbol{f},\boldsymbol{\varphi})_{\mathcal{Q}} + (\boldsymbol{u}_0,\boldsymbol{\varphi}(0))_\Omega + \tau\,\langle -\mathcal{K}\boldsymbol{n},\boldsymbol{\varphi}\rangle_G \\ (\nabla\cdot\boldsymbol{u},\phi)_{\mathcal{Q}} = \boldsymbol{0} \\ \boldsymbol{u}(0) = \boldsymbol{u}_0 \\ \boldsymbol{u}_\Gamma = \boldsymbol{u}\cdot\boldsymbol{n}, \end{aligned} \tag{5.3.2}$$

where $(v,w)_{\mathcal{Q}} = \int_0^T (v(t),w(t))_\Omega\,\mathrm{d}t$ and $\langle v,w\rangle_G = \int_0^T \langle v(t),w(t)\rangle_{\Gamma(t)}\,\mathrm{d}t$.

Remark 5.3.1. *We note that the last term (a curvature term) in the right hand-side of first equation of (5.3.2) corresponds to a force that acts only on the space-time interface G. Due to this, the pressure has a jump across the evolving interface $\Gamma(t)$. To approximate the curvature term in moving interface problems we need some accurate technique.*

Now, we replace the curvature term $-\mathcal{K}\boldsymbol{n}$ by the Laplace - Beltrami operator and then integrate by parts

$$-\int_{\Gamma(t)} \mathcal{K}\boldsymbol{n}\cdot\boldsymbol{\varphi}\,\mathrm{d}s = \int_{\Gamma(t)} \Delta_\Gamma\,\mathrm{id}_{\Gamma(t)}\cdot\boldsymbol{\varphi}\,\mathrm{d}s = -\int_{\Gamma(t)} \nabla_\Gamma\,\mathrm{id}_{\Gamma(t)}\ :\ \nabla_\Gamma\,\boldsymbol{\varphi}\,\mathrm{d}s, \tag{5.3.3}$$

where the identity mapping $\mathrm{id}_{\Gamma(t)} : \mathbb{R}^2 \mapsto \mathbb{R}^2$ is the restriction onto interface $\Gamma(t)$.

5.3.2 Temporal discretization and handling the curvature term

Let $0 = t_0 < t_1 < ... < t_M = T$ be a decomposition of the time interval $I = [0,T]$ with a time-step $k_m = t_{m+1} - t_m$, $0 \le m \le M-1$. We use the notations for time dependent subdomains $\omega^{m+1} = \omega(t_{m+1})$, $i = 1,2$, and time dependent interface $\Gamma^{m+1} = \Gamma(t_{m+1})$. Note that the outer boundary $\partial\Omega(t_{m+1})$ is fixed and therefore for all times t we have that

$\Omega(t) = \Omega$. For the discretization in time, we use an implicit Euler scheme.

Find $(\boldsymbol{u}^{m+1}, p^{m+1}) \in \boldsymbol{V} \times L$ for given $\boldsymbol{u}^m \in \boldsymbol{V}$ such that for all $(\boldsymbol{\varphi}, \phi) \in \boldsymbol{V} \times L$ it holds

$$\begin{aligned} &\frac{1}{k_m}\left(\boldsymbol{u}^{m+1} - \boldsymbol{u}^m, \boldsymbol{\varphi}\right)_\Omega + \left(\nu\,\nabla \boldsymbol{u}^{m+1}, \nabla \boldsymbol{\varphi}\right)_\Omega - \left(\nabla \cdot \boldsymbol{\varphi}, p^{m+1}\right)_\Omega \\ &+ \left(\nabla \cdot \boldsymbol{u}^{m+1}, \phi\right)_\Omega = \left(\boldsymbol{f}^{m+1}, \boldsymbol{\varphi}\right)_\Omega - \tau\,\langle \nabla_\Gamma \mathrm{id}_{\Gamma^{m+1}},\, \nabla_\Gamma\, \boldsymbol{\varphi}\rangle_{\Gamma^{m+1}} \end{aligned} \tag{5.3.4}$$

As mentioned in Remark 5.3.1, we need here to handle the curvature term, which is the last term in (5.3.4). The curvature term can be treated as fully explicit, semi-implicit or fully implicit in time. Numerical experiments in [12] show us that the explicit form is only conditionally stable and the fully implicit form with unknown subdomains $\omega^{m+1} = \omega(t_{m+1})$, $i = 1, 2$, is too complicated. Therefore we use the semi-implicit time discretization as proposed in [12]. The idea of this approach based on the fact that the fifth equation in (2.3.6) can be solved directly by using implicit Euler scheme. Then we can describe the new position x^{m+1} as follows:

$$x^{m+1} = x^m + k_m\, \boldsymbol{u}^{m+1}, \tag{5.3.5}$$

where $\boldsymbol{u}^{m+1}$ is the unknown velocity at the new time step. After plugging (5.3.5) in the curvature term we obtain

$$\begin{aligned} \langle \nabla_\Gamma \mathrm{id}_{\Gamma^{m+1}},\, \nabla_\Gamma\, \boldsymbol{\varphi}\rangle_{\Gamma^{m+1}} &\approx \left\langle \nabla_\Gamma \left(\mathrm{id}_{\Gamma^m} + k_m\, \boldsymbol{u}^{m+1}\right),\, \nabla_\Gamma\, \boldsymbol{\varphi}\right\rangle_{\Gamma^m} \\ &= \langle \nabla_\Gamma \mathrm{id}_{\Gamma^m},\, \nabla_\Gamma\, \boldsymbol{\varphi}\rangle_{\Gamma^m} + k_m \left\langle \nabla_\Gamma \boldsymbol{u}^{m+1},\, \nabla_\Gamma\, \boldsymbol{\varphi}\right\rangle_{\Gamma^m}. \end{aligned}$$

The last term is unknown, but it is symmetric in the unknowns and positive semi - definite. Therefore we will shift it to the left hand side of the equation.

Find $(\boldsymbol{u}^{m+1}, p^{m+1}) \in \boldsymbol{V} \times L$ for given $\boldsymbol{u}^m \in \boldsymbol{V}$ such that for all $(\boldsymbol{\varphi}, \phi) \in \boldsymbol{V} \times L$ it holds

$$\begin{aligned} &\frac{1}{k_m}\left(\boldsymbol{u}^{m+1} - \boldsymbol{u}^m, \boldsymbol{\varphi}\right)_\Omega + \left(\nu\,\nabla \boldsymbol{u}^{m+1}, \nabla \boldsymbol{\varphi})\right)_\Omega - \left(\nabla \cdot \boldsymbol{\varphi}, p^{m+1}\right)_\Omega \\ &+ \left(\nabla \cdot \boldsymbol{u}^{m+1}, \phi\right)_\Omega + k_m \left\langle \nabla_\Gamma \boldsymbol{u}^{m+1},\, \nabla_\Gamma\, \boldsymbol{\varphi}\right\rangle_{\Gamma^m} \\ &= \left(\boldsymbol{f}^{m+1}, \boldsymbol{\varphi}\right)_\Omega - \tau\,\langle \nabla_\Gamma \mathrm{id}_{\Gamma^m},\, \nabla_\Gamma\, \boldsymbol{\varphi}\rangle_{\Gamma^m}. \end{aligned} \tag{5.3.6}$$

In [20] the unknown term defined as the known function $\boldsymbol{u}^{m+1}(x^m)$ and to get a new position we just use (5.3.5).

5.3.3 Spatial discretization

For space discretization, we use the locally modified finite element pair $\mathcal{P}_2 - \mathcal{P}_0$.

Find $(\boldsymbol{u}_h^{m+1}, p_h^{m+1}) \in \boldsymbol{V}_h \times L_h$ for given $\boldsymbol{u}_h^m \in \boldsymbol{V}_h$ such that for all $(\boldsymbol{\varphi}, \phi) \in \boldsymbol{V}_h \times L_h$ it holds

$$\begin{aligned} &\frac{1}{k_m}\left(\boldsymbol{u}_h^{m+1} - \boldsymbol{u}_h^m, \boldsymbol{\varphi}\right)_\Omega + \left(\nu\,\nabla \boldsymbol{u}_h^{m+1}, \nabla\boldsymbol{\varphi}\right)_\Omega - \left(\nabla\cdot\boldsymbol{\varphi}, p_h^{m+1}\right)_\Omega \\ &+ \left(\nabla\cdot\boldsymbol{u}_h^{m+1}, \phi\right)_\Omega + k_m \left\langle \nabla_\Gamma \boldsymbol{u}_h^{m+1},\, \nabla_\Gamma\,\boldsymbol{\varphi}\right\rangle_{\Gamma_h^m} \\ &= \left(\boldsymbol{f}_h^{m+1}, \boldsymbol{\varphi}\right)_\Omega - \tau\left\langle \nabla_\Gamma \mathrm{id}_{\Gamma_h^m},\, \nabla_\Gamma\,\boldsymbol{\varphi}\right\rangle_{\Gamma_h^m}. \end{aligned} \tag{5.3.7}$$

5.3.4 Numerical Results

In this section, we consider time dependent Stokes problem with a pressure solution that is discontinuous across a interface.

Example 1

In the first example, we present time dependent Stokes problem with a pressure solution that is discontinuous across a stationary interface Γ. We consider the problem (5.3.1) on the domain $\Omega = [-2,2]^2$ with Dirichlet boundary condition on the boundary $\partial\Omega$. On the interface we have the surface tension force with $\tau = 1$. The viscosities and densities on Ω are constant and equal to one. The analytical solutions are as follows

$$\begin{aligned} \boldsymbol{u}_{ex}(t,\boldsymbol{x}) &= \begin{pmatrix} -y\,(1-e^{-t})\,e^{-(x^2+y^2)} \\ x\,(1-e^{-t})\,e^{-(x^2+y^2)} \end{pmatrix}, \\ p_{ex}(t,\boldsymbol{x}) &= x^3\,(1-e^{-t}) + \begin{cases} \frac{\pi}{16} - 1 & \text{in} \quad \Omega_1, \\ \frac{\pi}{16} & \text{in} \quad \Omega_2, \end{cases} \end{aligned}$$

where $\Omega_1 = \{\boldsymbol{x} \in \Omega : l(\boldsymbol{x}) < 0\}$, $\Omega_2 = \Omega \setminus \overline{\Omega}_1$, $\Gamma = \{\boldsymbol{x} \in \Omega : l(\boldsymbol{x}) = 0\}$ with $l(\boldsymbol{x}) = x^2 + y^2 - 1$. The right hand-side $\boldsymbol{f}$ is adjusted to the prescribed analytical solution.

In Figures 6.2, 6.3 are shown the solutions which are compared with analytical solutions with mesh size $h = 1/128$ and time step $k = 1/10$. As shown in the diagram on the right of Figures 6.2, 6.3, the exact and numerical values for the first component of velocity and pressure agree well. We observe that our method gives the excellent results which are almost exact.

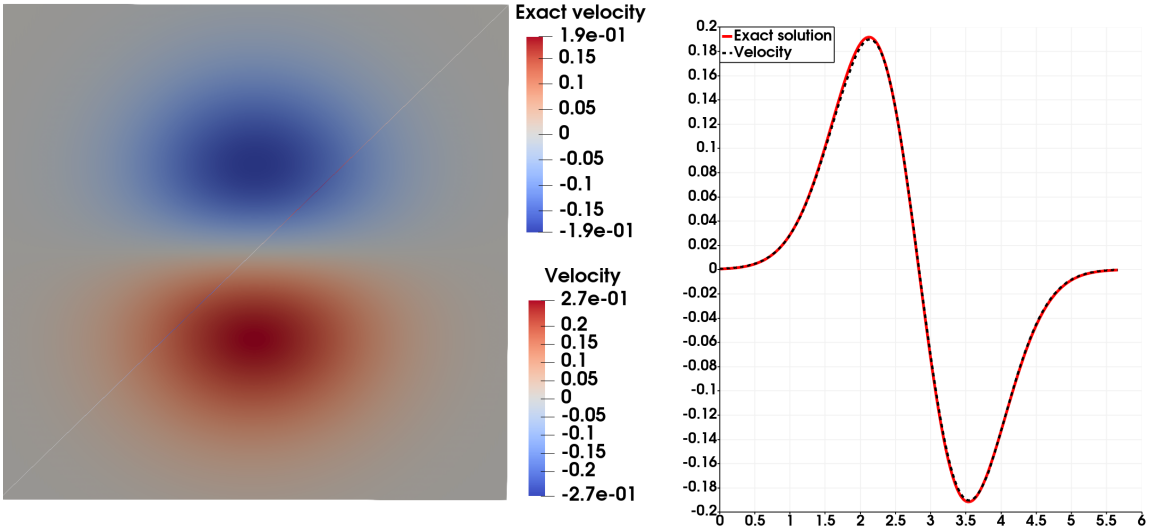

Figure 5.19: Comparison of numerical and exact solutions for the first component of velocity at $t = 1$. Left: Profile of the first component of velocity . Right: Plot over the line.

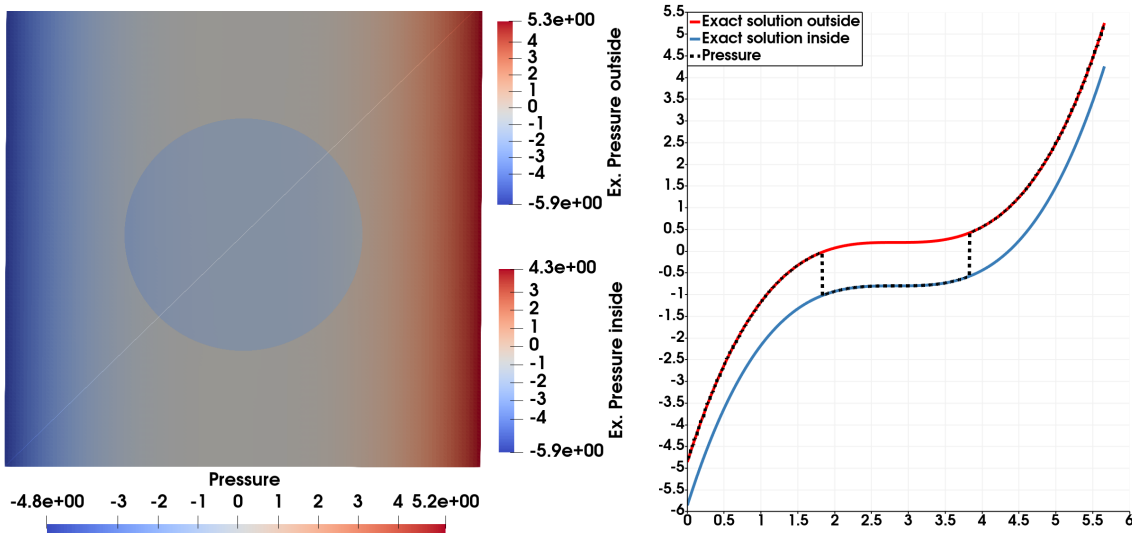

Figure 5.20: Comparison of numerical and exact solutions for pressure at $t = 1$. Left: Pressure profile. Right: Plot over the line.

Example 2

We take $\Omega = [-2, 2]^2 \subset \mathbb{R}^2$ and consider a time dependent interface $\Gamma(t)$ which is a moving circle as follows

$$\Gamma(t) := \{(x, y) \in \Omega \ : \ (x - t)^2 + y^2 - 1 = 0\}.$$

On the interface we have the surface tension force with $\tau = 1$. The viscosities and densities on Ω are equal to one. We take $\boldsymbol{f} = \mathbf{0}$ and non-homogeneous Dirichlet boundary condition with $\boldsymbol{u}_D = (1, 1)^T$ on the upper and bottom boundaries. Other boundaries have

a do-nothing condition. The analytical solutions are given as follows:

$$\boldsymbol{u} \equiv (1,1)^T \quad \text{in} \quad \Omega, \qquad p = \begin{cases} 1 & \text{in} \quad \Omega_1, \\ 0 & \text{in} \quad \Omega_2. \end{cases}$$

The computed discrete velocity magnitude and pressure for $t = \frac{i}{8}$, $i = 0, ..., 8$ are shown

h	$\|\boldsymbol{u}_h^k - \boldsymbol{u}\|_{L^\infty(\Omega)}$	$\|p_h^k - p\|_{L^\infty(\Omega_1)}$	$\|p_h^k - p\|_{L^\infty(\Omega_2)}$
1/32	0.019	0.145	0.059
1/64	0.004	0.164	0.183
1/128	0.002	0.146	0.209

Table 5.9: The maximum norm for velocity and pressure in different mesh sizes with fixed time step $t = 0.5$.

in Figure 6.2, 6.3. We observe that the first component of discrete velocity and pressure values in different time steps with fixed mesh size are close to the exact solutions.

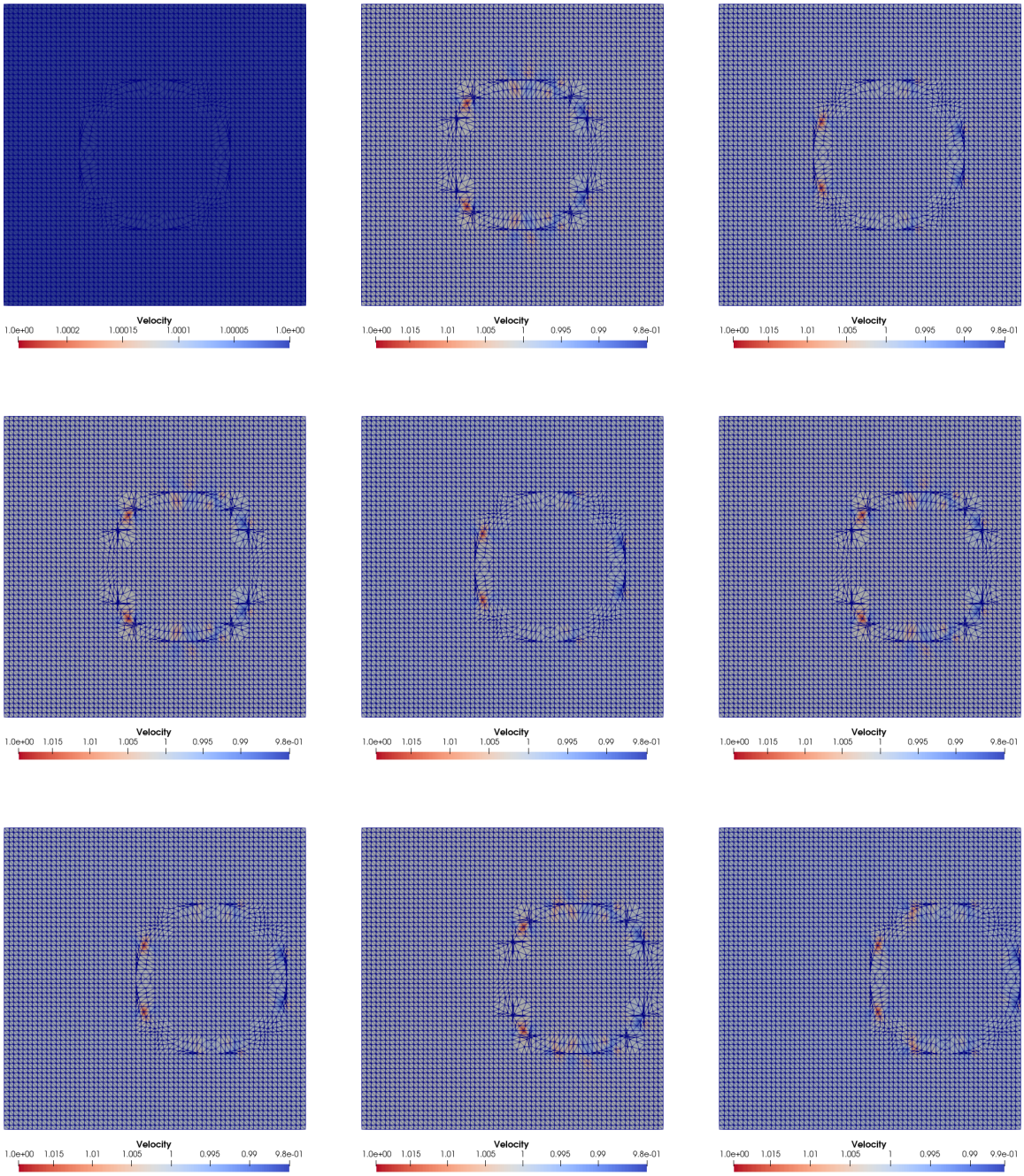

Figure 5.21: The computed the first component of velocity magnitude for $t = \frac{i}{8}$, $i = 0, ..., 8$ with mesh size 1/32. The all discrete velocities are very close to 1.

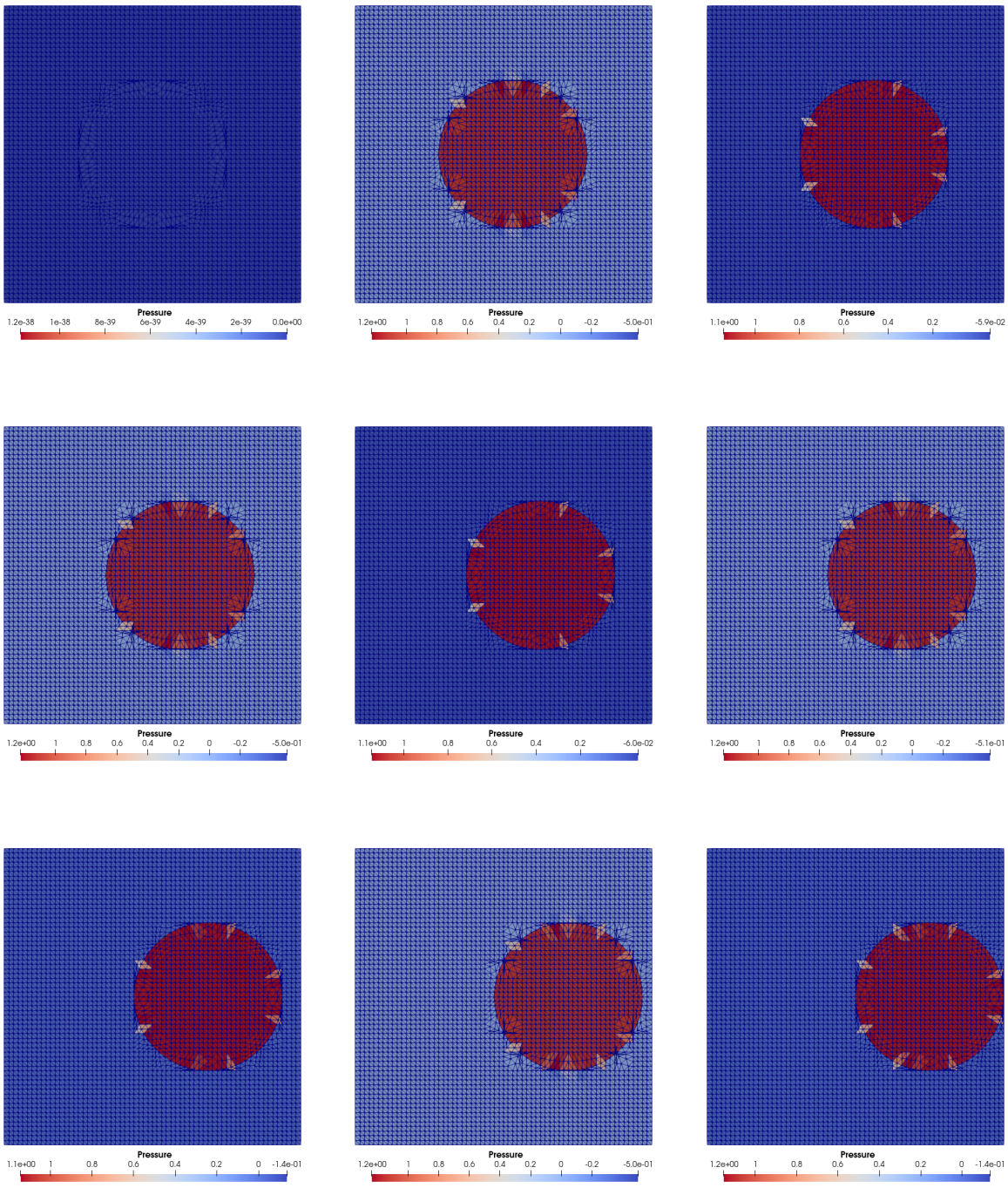

Figure 5.22: Pressure for $t = \frac{i}{8}$, $i = 0, ..., 8$ with mesh size 1/32. The discrete pressure values are close to 1 in Ω_1 and close to 0 in Ω_2.

Chapter 6: Discretization of fluid-structure interaction problems

In this chapter, we study a model problem of a fluid-rigid body interaction problem (2.4.1). The model problem is constructed by taking only the drag force, which is acting on the rigid body in the vertical direction such that

$$\begin{aligned} \rho_f\, \partial_t \boldsymbol{u}_f - \nabla \cdot \boldsymbol{\sigma}(\boldsymbol{u}_f, p_f) = \mathbf{0}, \quad \nabla \cdot \boldsymbol{u}_f &= \mathbf{0} \qquad \text{in} \quad \Omega_f, \\ \frac{\mathrm{d}}{\mathrm{dt}} \boldsymbol{u}_s \cdot m_s &= \mathbf{f}_s \qquad \text{in} \quad \Omega_s, \\ \boldsymbol{u}_f &= \boldsymbol{u}_s \qquad \text{on} \quad \Gamma_{\mathrm{I}}, \\ \boldsymbol{u}_f &= \mathbf{0} \qquad \text{on} \quad \Gamma_{\mathrm{W}} \cup \Gamma_{\mathrm{B}}, \\ \boldsymbol{\sigma}(\boldsymbol{u}_f, p_f)\, \boldsymbol{n} &= 0 \qquad \text{on} \quad \Gamma_{\mathrm{T}}, \end{aligned} \tag{6.0.1}$$

with the stress tensor

$$\boldsymbol{\sigma}(\boldsymbol{u}_f, p_f) := \mu \nabla \boldsymbol{u}_f - p_f \mathbb{I}. \tag{6.0.2}$$

Here, $\mathbf{f}_s$ is the force acting on the rigid body

$$\mathbf{f}_s = \begin{pmatrix} 0 \\ m_s\, g - V_s\, \rho_f\, g + \boldsymbol{F}_{drag} \end{pmatrix} \tag{6.0.3}$$

where $V_s = \dfrac{m_s}{\rho_s}$ and $g = -9,81 \frac{m}{s^2}$. The drag force $\boldsymbol{F}_{drag}$ is defined as follows

$$\boldsymbol{F}_{drag} = \int_{\Gamma_{\mathrm{I}}} \boldsymbol{\sigma}(\boldsymbol{u}_f, p_f)\, \boldsymbol{n}\, \boldsymbol{e}_2 \, \mathrm{d}s, \tag{6.0.4}$$

where $\boldsymbol{e}_2$ is the unit vector in vertical direction.

6.1 Solid equation

We consider the solid equation of the problem (6.0.1) as the movement of the solid and it is governed by Newton's second law of motion. We assume that the solid material is relatively hard and has a spherical form. Since we will take only vertical movement of the

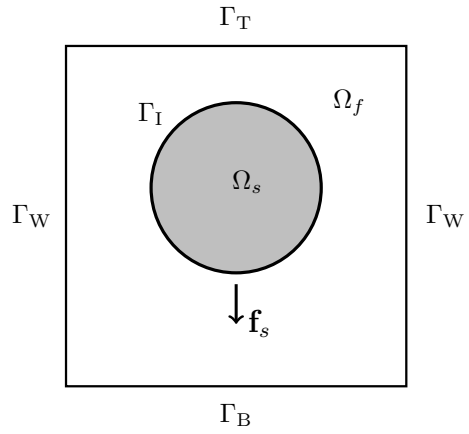

Figure 6.1: Geometry and notations of the fsi problem, $\Omega = \Omega_s \cup \Gamma_{\mathrm{I}} \cup \Omega_f$.

solid, we get a scalar ODE as follows:

$$\frac{\mathrm{d}}{\mathrm{dt}}\boldsymbol{u}_s(t) = \left(1 - \frac{\rho_f}{\rho_s}\right) g + \frac{1}{V_s\,\rho_s}\,\boldsymbol{F}_{drag}, \tag{6.1.1}$$

where $\boldsymbol{u}_s(t) = \frac{\mathrm{d}}{\mathrm{dt}}\boldsymbol{c}_s$ is the solid velocity with the center of mass $\boldsymbol{c}_s$ of the solid Ω_s.
The solid body equation is coupled with fluid equations through the boundary conditions at the interface Γ_I as follows:

$$\boldsymbol{u}_f|_{\Gamma_{\mathrm{I}}} = \boldsymbol{u}_s = \frac{\mathrm{d}}{\mathrm{dt}}\boldsymbol{c}_s. \tag{6.1.2}$$

6.1.1 Evaluation of the surface integral.

Surface integrals (6.1.3) are evaluated by using the $Babuška - Miller$ trick, see Remark 8.17 of the book [83] or [11]. We show first the derivation for the drag functional. For that, we define a test function $\boldsymbol{\xi} \in H^1(\Omega(t))^2$ with a vanishing first component ξ_1. We define the second component ξ_2 as follows:

$$\xi_2 = \begin{cases} 1, & \text{on} \quad \Gamma_{\mathrm{I}} \\ 0, & \text{else} \end{cases}$$

It holds

$$\boldsymbol{F}_{drag} = \int_{\Gamma_{\mathrm{I}}} \boldsymbol{\sigma}(\boldsymbol{u}_f, p_f)\,\boldsymbol{n}\,\boldsymbol{e}_2\,\mathrm{d}s = \int_{\Gamma_{\mathrm{I}}} \boldsymbol{\sigma}(\boldsymbol{u}_f, p_f)\,\boldsymbol{n}\,\boldsymbol{\xi}\,\mathrm{d}s.$$

Now we use the divergence theorem on Ω_f and we obtain

$$\boldsymbol{F}_{drag} = \int_{\Gamma_{\mathrm{I}}} \boldsymbol{\sigma}(\boldsymbol{u}_f, p_f)\,\boldsymbol{n}\,\boldsymbol{\xi}\,\mathrm{d}s = \int_{\Omega_f} \Big(\boldsymbol{\sigma}(\boldsymbol{u}_f, p_f)\nabla\boldsymbol{\xi} + \nabla\cdot\boldsymbol{\sigma}(\boldsymbol{u}_f, p_f)\,\boldsymbol{\xi}\Big)\,\mathrm{d}x.$$

After using the first equation of (2.4.1), we get

$$\boldsymbol{F}_{drag} = \Big(\boldsymbol{\sigma}(\boldsymbol{u}_f, p_f), \nabla\boldsymbol{\xi}\Big)_{\Omega_f} + \Big(\rho_f\,\partial_t\boldsymbol{u}_f, \boldsymbol{\xi}\Big)_{\Omega_f}. \tag{6.1.3}$$

Now, (6.1.3) is exactly the bilinear form that we have to evaluate when we set up the right-hand side and the system matrix.

6.2 Discretization and Implementation

For spatial discretization, we apply the *locally modified finite element scheme* introduced in chapter 5. For time discretization, we use implicit Euler method for the unsteady Stokes equation and explicit Euler method for solid ODE.

Solid ODE

We discretize the scalar ODE (6.1.1) with given $\boldsymbol{u}_s^0, \boldsymbol{u}_f^0, p_f^0$ and for all $k = 0, 1, ..., n-1$. It holds with time step τ:

$$\frac{\boldsymbol{u}_s^{k+1} - \boldsymbol{u}_s^k}{\tau} = \Big(1 - \frac{\rho_f}{\rho_s}\Big)\, g + \frac{1}{V_s\, \rho_s}\, \boldsymbol{F}_{drag}^k\Big(\boldsymbol{u}_f^k, p_f^k, \boldsymbol{\xi}^k\Big)$$
$$\boldsymbol{u}_s^{k+1} = \boldsymbol{u}_s^k + \bigg(\Big(1 - \frac{\rho_f}{\rho_s}\Big)\, g + \frac{1}{V_s\, \rho_s}\, \boldsymbol{F}_{drag}^k\Big(\boldsymbol{u}_f^k, p_f^k, \boldsymbol{\xi}^k\Big)\bigg)\, \tau,$$

likewise the center of mass (6.1.2) of the rigid body with given $\boldsymbol{c}_s^0$ and for all $k = 0, 1, ..., n-1$, it holds

$$\boldsymbol{c}_s^{k+1} = \boldsymbol{c}_s^k + \boldsymbol{u}_s^{k+1}\, \tau.$$

Unsteady Stokes equation

We discretize the time dependent Stokes equation in (2.4.1) with given $\boldsymbol{u}_f^0$ and for all $k = 0, 1, ..., n-1$. It holds with time step τ

$$\frac{\boldsymbol{u}_f^{k+1} - \boldsymbol{u}_f^k}{\tau} - \nabla \cdot \boldsymbol{\sigma}(\boldsymbol{u}_f^{k+1}, p_f^{k+1}) = \boldsymbol{0}. \tag{6.2.1}$$

6.2.1 Handling of dynamic meshes

In the numerical approximation (6.2.1), the velocity approximation $\boldsymbol{u}_f^k$ at time t_k that has been computed on the domain $\Omega_f(t_n)$ has to be evaluated on the new domain $\Omega_f(t_{k+1})$ at time t_{k+1}. The velocity $\boldsymbol{u}_f^k$ is divergence-free with respect to the test space corresponding to the domain $\Omega_f(t_k)$, but this condition no longer holds on the new spatial domain at time t_{k+1}. Thus, in the spatial discrete case, the loss of the discrete divergence-free condition gives us nonphysical osculation, in particular, in the discrete solution for pressure. Many authors studied this problem by assuming static finite element mesh, e.g Temam [92], Girault and Raviart [93], Heywood and Rannacher [63], [64], Bause [16]. Error estimates for finite element approximations of the Stokes system on dynamic meshes have been established in [26]. We follow here [26] and use the discrete Stokes projection to evaluate

the solution at time t_k on the new domain at time t_{k+1}.

Divergence-free Stokes projection: After computing $(\boldsymbol{u}_f^k, p_f^k)^T \in \boldsymbol{V}(\Omega(t_k)) \times L(\Omega(t_k))$ we first compute a projection $\tilde{\boldsymbol{u}}_f^k$ of $\boldsymbol{u}_f^k$ into $\boldsymbol{V}(\Omega(t_{k+1}))$ which is divergence-free with respect to the test function in $\boldsymbol{V}(\Omega(t_{k+1}))$ and use this projection as initial values for the next time step. The projection $\tilde{\boldsymbol{u}}_f^k$ is determined by:

$$\begin{aligned} \left(\nabla \tilde{\boldsymbol{u}}_f^k, \nabla \varphi\right) - \left(\tilde{p}_f, \nabla \cdot \varphi\right) &= \left(\nabla \boldsymbol{u}_f^k, \nabla \varphi\right) \quad \forall \varphi \in \boldsymbol{V}(\Omega(t_{k+1})) \\ \left(\nabla \cdot \tilde{\boldsymbol{u}}_f^k, \zeta\right) &= 0 \qquad\qquad\quad \forall \zeta \in L(\Omega(t_{k+1})) \end{aligned} \tag{6.2.2}$$

Then we apply the projection $\tilde{\boldsymbol{u}}_f^k$ in (6.2.1) and for all $k = 0, 1, ..., n-1$ it holds with time step τ:

$$\begin{aligned} \left(\frac{\boldsymbol{u}_f^{k+1} - \tilde{\boldsymbol{u}}_f^k}{\tau}, \varphi\right) + \left(\nabla \boldsymbol{u}_f^{k+1}, \nabla \varphi\right) - \left(p_f^{k+1}, \nabla \cdot \varphi\right) &= \boldsymbol{0} \quad \forall \varphi \in \boldsymbol{V}(\Omega(t_{k+1})) \\ \left(\nabla \cdot \boldsymbol{u}_f^{k+1}, \xi\right) &= 0 \quad \forall \xi \in L(\Omega(t_{k+1})) \end{aligned} \tag{6.2.3}$$

Implementation

The described algorithm and equations above have been implemented in the finite element library Gascoigne3d.

6.2.2 Numerical experiment

In our numerical example we study the convergence rates of the *locally modified finite element* approximation of the fluid-structure problem. We consider the falling ball example of the problem (6.0.1) with $\Omega := [-2, 2]^2$ and rigid body Ω_s on the time interval $[0, 2]$. At $t = 0$ the rigid body domain is described by $\Omega_s(0) := \{\boldsymbol{x} = (x, y)^T \in \mathbb{R}^2 \,|\, x^2 + y^2 \leq r\}$ for a given circle radius $r = 0.5$. A material parameters densities and viscosity are given as $\rho_f = 1$, $\rho_s = 10$ and $\mu = 1$. *Boundary conditions:* on the interface Γ_I between the fluid and solid, the Dirichlet boundary condition is given by the continuity of the velocity (6.1.2). On the wall and bottom boundaries $\Gamma_W \cup \Gamma_B$ we take homogeneous Dirichlet boundary and *do-nothing* condition on the top boundary, for the notations see Figure 2.3. The y component for velocity and pressure profiles are shown in Figures 6.2, 6.3 at the beginning and the end of time. In Figures 6.4 and 6.5 (left) we compare the approximate solutions for the velocity in y-direction, rigid body motion and the drag functional with mesh size $h = 0.03125$ and time step $\tau = 0.02$ before and after using divergence-free Stokes projection (6.2.2). We also investigate the velocity in y-direction, rigid body motion and the drag functional for different mesh sizes with fixed time step $\tau = 0.02$, and for different time steps with fixed mesh size $h = 0.03125$, see Figures 6.6, 6.7 and 6.8. The convergence orders for velocity in y-direction, rigid body motion and Drag functional in each iteration and their mean values are plotted in Figures 6.9, 6.10 and 6.11, respectively. We have

observed that the mean values of the convergence orders are for velocity in y-direction $\mathcal{O}(\tau + h^2)$, rigid body motion $\mathcal{O}(\tau + h^2)$ and drag functional $\mathcal{O}(\tau + h^{\frac{1}{2}})$. The Stokes projection is used for evaluating the velocity approximation on the new meshes. Our observation is that if the configuration of the patch is changed in the new time step the Stokes projection is capable of preventing a loss in the rate of convergence. Moreover, the drag functional depends on pressure which is unstable. These could be reasons why the mean value of the convergence of order of the drag functional is $\mathcal{O}(\tau + h^{\frac{1}{2}})$, see Figure 6.12 (left). Next, we investigate the convergence for the drag functional by neglecting the pressure component. In Figure 6.5 (right), we show the behavior of the drag functional without pressure component. The convergence orders in each iteration and the mean value of the convergence orders for the drag functional without pressure component is plotted in Figure 6.12 and we observe that the mean value of convergence orders for the drag functional without pressure component has $\mathcal{O}(\tau + h^2)$.

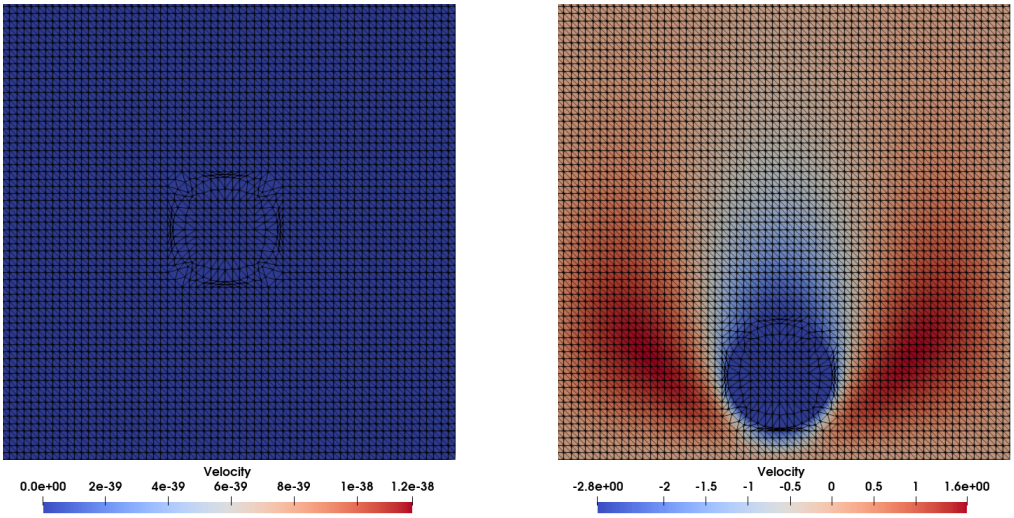

Figure 6.2: Second component of the velocity at time $t = 0$ (left) and $t = 1$ (right).

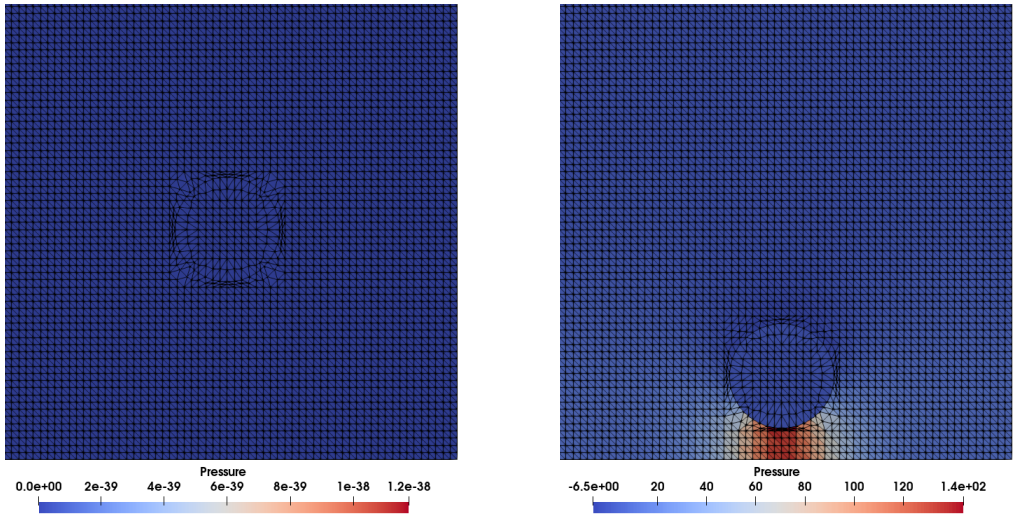

Figure 6.3: Pressure profile at time $t = 0$ (left) and $t = 1$ (right).

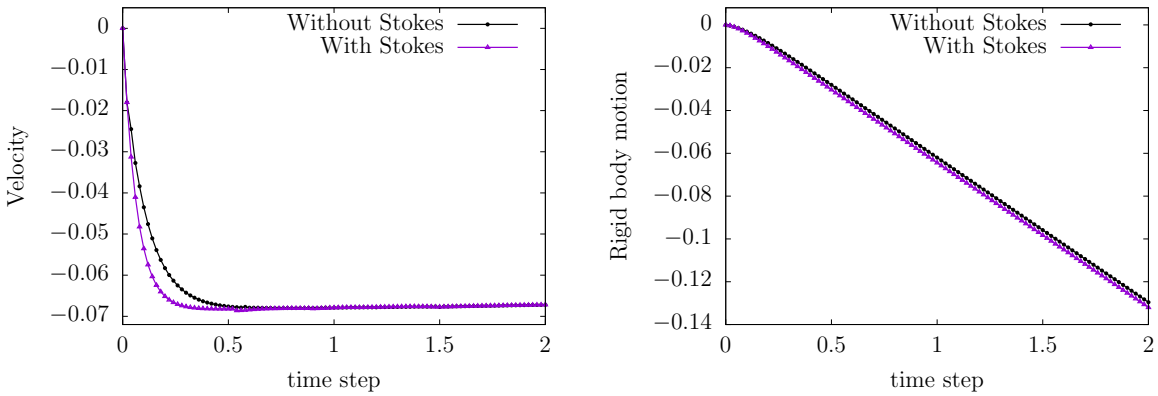

Figure 6.4: Comparison the results for velocity and motion before and after using Stokes projection with mesh size $h = 0.03125$ and time step $\tau = 0.02$.

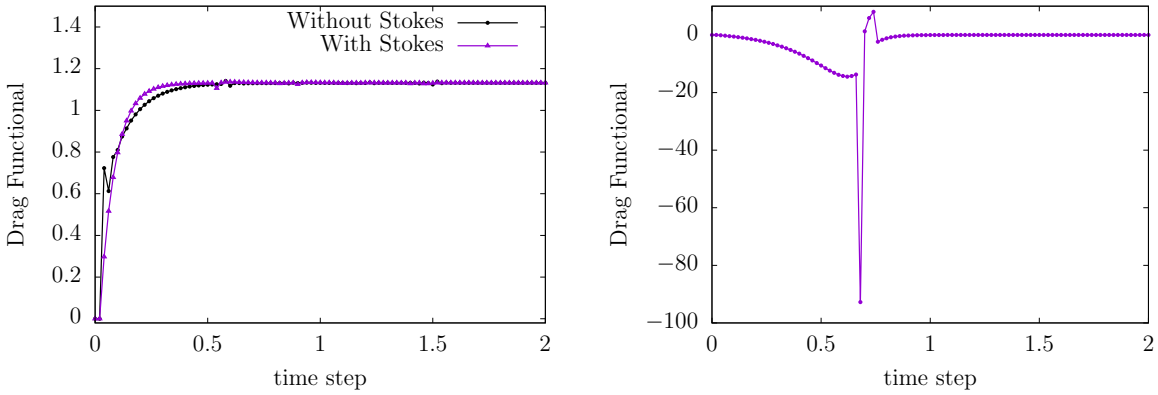

Figure 6.5: Left: Comparison the results for drag before and after using Stokes projection with mesh size $h = 0.03125$ and time step $\tau = 0.02$. Right: Behavior of the drag without pressure component.

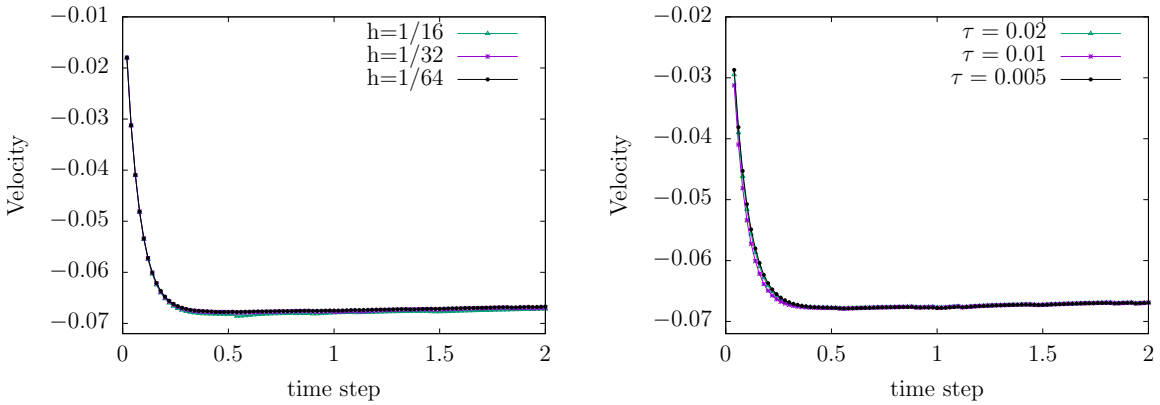

Figure 6.6: Velocity in y-direction with fixed time step $\tau = 0.02$ and different mesh sizes (left) and with fixed mesh size $h = 1/32$ and different time steps (right).

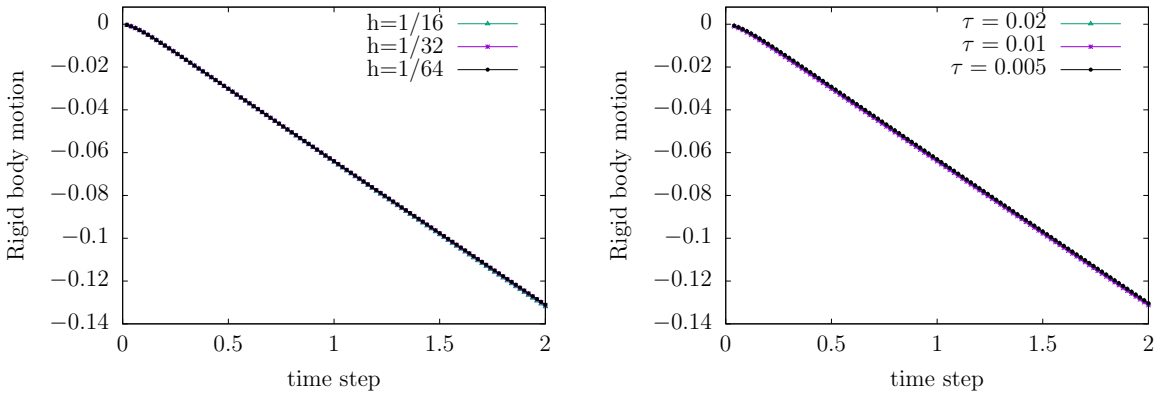

Figure 6.7: Rigid body motion with fixed time step $\tau = 0.02$ and different mesh sizes (left) and with fixed mesh size $h = 1/32$ and different time steps (right).

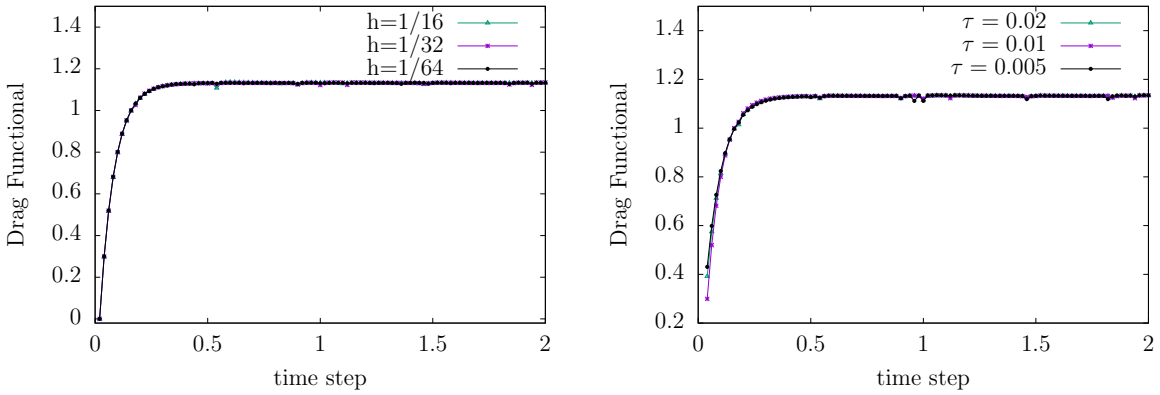

Figure 6.8: Drag functional with fixed time step $\tau = 0.02$ and different mesh sizes (left) and with fixed mesh size $h = 1/32$ and different time steps (right).

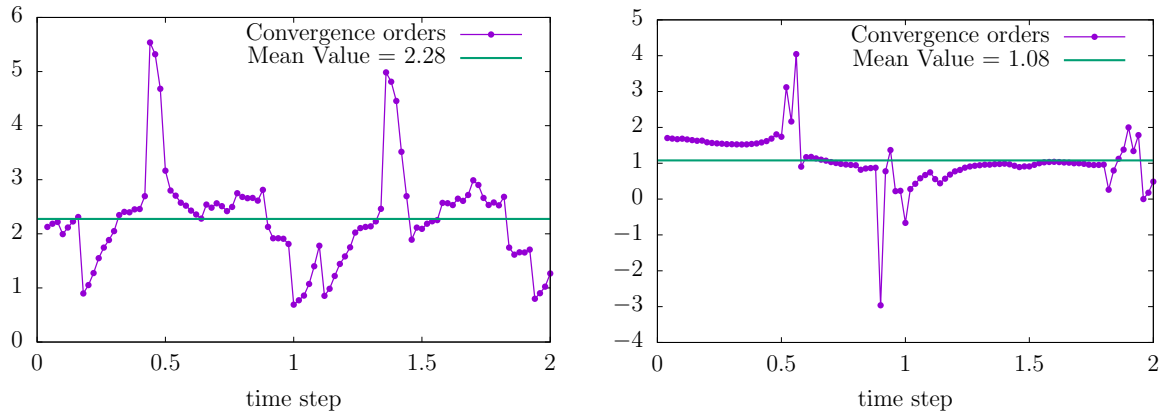

Figure 6.9: Convergence order for the velocity in y-direction and their mean value with fixed time step $\tau = 0.02$ and different mesh sizes (left) and with fixed mesh size $h = 1/32$ and different time steps (right).

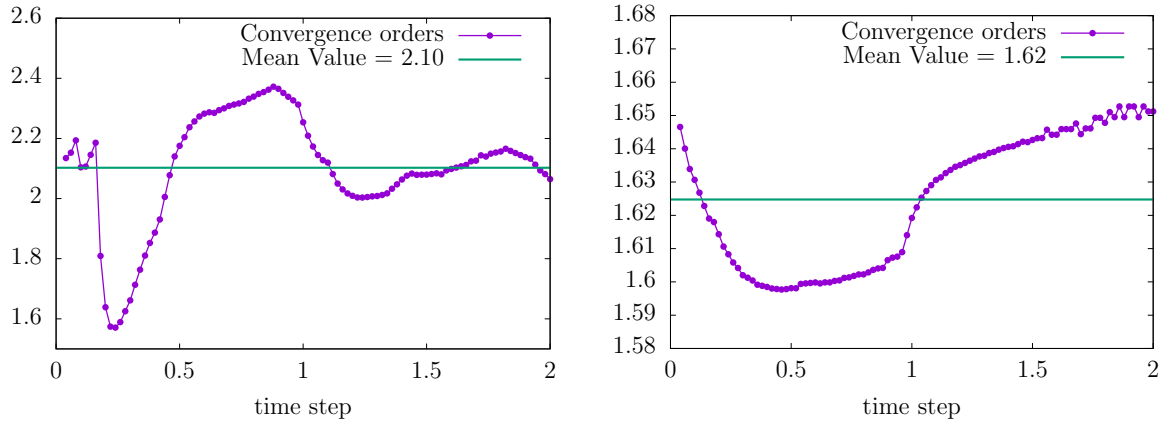

Figure 6.10: Convergence order for the rigid body motion and their mean value with fixed time step $\tau = 0.02$ and different mesh sizes (left) and with fixed mesh size $h = 1/32$ and different time steps (right).

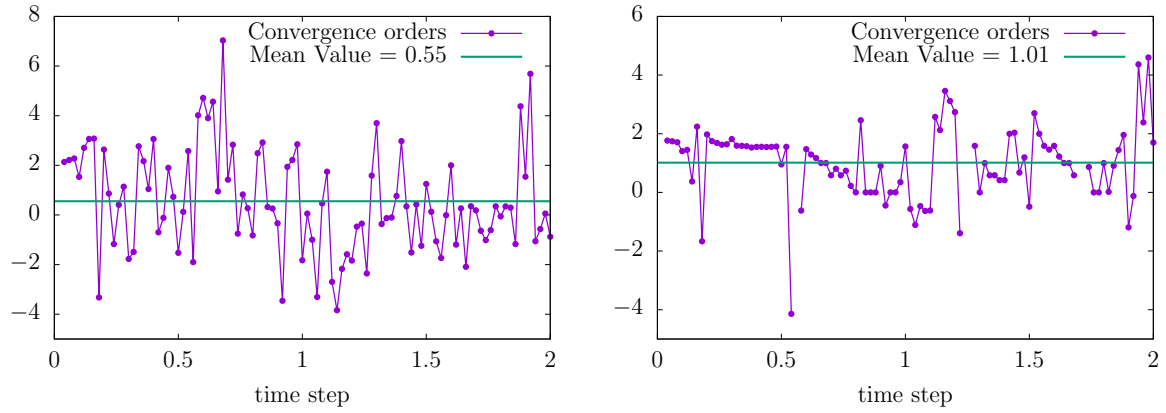

Figure 6.11: Convergence order for the drag functional and their mean value with fixed time step $\tau = 0.02$ and different mesh sizes (left) and with fixed mesh size $h = 1/32$ and different time steps (right).

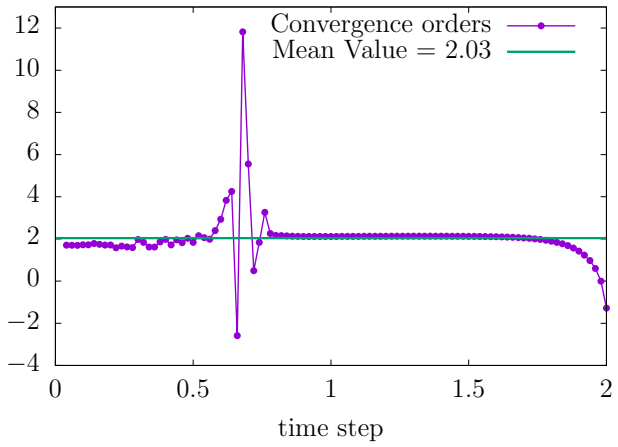

Figure 6.12: Convergence orders for the drag functional without pressure component and their mean value with different mesh sizes and fixed time step $t = 0.02$.

Chapter 7: Conclusion and Future work

Elliptic interface problems

We have presented an extension of the locally modified finite element method for interface problem that was introduced in [47], to second order. We were able to show optimal-order error estimates of order $3-\epsilon$ in the L^2-norm and $2-\epsilon$ in the discrete energy norm. In the standard H^1-norm, the convergence order is reduced to 1.5, due to the mismatch of continuous and discrete interface. Finally, we have presented different numerical examples that illustrate the convergence behaviour and the performance of the method.

Tho-phase flow problems

First, we analyzed a stationary Stokes interface problem. For the discretization, we applied locally modified finite elements for the velocity combined with piecewise constant elements for the pressure. We proved the discrete *inf-sup* condition for the $\mathcal{P}_2 - \mathcal{P}_0$ elements. We presented optimal error estimates in the L^2-norm and sub-optimal estimates in the energy norm for the Stokes interface problem. Moreover, we considered stationary and time dependent Stokes interface problems with surface tension. In the variational formulation of these problems, a linear functional which describes the surface tension force occurs and it depends on the location and the curvature of the interface. Thus, we used a Laplace-Beltrami operator to handle the curvature term and for time dependent problem we applied the semi-implicit time integration of the surface tension force.

Fluid-structure problems

We investigated a fluid-structure-interaction problems. In the numerical simulations we took a rigid body model for the falling particles. We studied locally modified finite element approximations of the time dependent Stokes system, which prescribed the fluid model, on dynamically changing meshes. We applied the implicit Euler method for time discretization and used the discrete Stokes projection.

Future work

For the future, we have some ideas to apply our method for advanced problems.

– Apply the *inf-sup* stable $\mathcal{P}_2 - \mathcal{P}_0$ elements for the discretization of interface problems including Navier-Stokes equations.

– Extend the rigid body to elastic solids in the fluid-structure-interaction problems.

– The $\mathcal{P}_2 - \mathcal{P}_0$ elements is not optimal since the pressure is 2 orders lower. Thus, we prefer to use a parametric finite element method for a balanced approach such as $\mathcal{P}_2 - \mathcal{P}_1$ elements.

Bibliography

[1] M. Ainsworth, G. R. Barrenechea, and A. Wachtel. Stabilization of high aspect ratio mixed finite elements for incompressible flow. *SIAM J. Numerical Analysis*, 53:1107–1120, 2015.

[2] M. Ainsworth and P. Coggins. The stability of mixed hp-finite elemenet methods for Stokes flow on high aspect ratio elements. Application to the Stokes equations. *SIAM J. Numerical Analysis*, 38:1721–1761, 2000.

[3] T. Apel. *Anisotropic finite elements: Local estimates and application.* Advances in Numerical Mathematics. Teubner, Stuttgart, 1999.

[4] T. Apel, V. Kempf, A. Linke, and C. Merdon. A nonconforming pressure-robust finite element method for the Stokes equations on anisotropic meshes. *IMA Journal of Numerical Analysis*, (draa097):1–25, 2021.

[5] T. Apel, T. Knopp, and G. Lube. Stabilized finite element methods with anisotropic mesh refinement for the Oseen problem. *Appl Numer Math.*, 58(12):1830–1843, 2008.

[6] T. Apel and G. Matthies. Nonconforming, anisotropic, rectangular finite elements of arbitrary order for the Stokes problem. *SIAM Journal on Numerical Analysis*, 46(4):1867–1891, 2008.

[7] T. Apel, S. Nicaise, and J. Schöberl. A non-conforming finite element method with anisotropic mesh grading for the Stokes problem in domains with edges. *Numerical Analysis*, 2000.

[8] I. Babuška. The finite element method for elliptic equations with discontinuous coefficients. *Computing*, 5:207–213, 1970.

[9] I. Babuška. The finite element method for elliptic equations with discontinuous coefficients. *Computing*, 5:207–213, 1970.

[10] I. Babuška, U. Banarjee, and J. E. Osborn. Generalized finite element methods: Main ideas, results, and perspective. *Int J Comput Methods*, 1:67–103, 2004.

[11] M. A. Babuška, I. The post-processing approach in the finite element method. i. calculations of displacements, stresses and other higher derivatives of the displacements. *Internat. J. Numer. Methods Engrg.*, 20:1085–1109, 1984.

[12] E. Bänsch. Numerical methods for the instationary Navier-Stokes equations with a free capillary surface. *Habilation thesis, Universität Freiburg*, 1998.

[13] E. Bänsch. Finite element discretization of the Navier-Stokes equations with a free capillary surface. *Numerische Mathematik*, 88:203 – 235, 2001.

[14] G. R. Barrenechea and A. Wachtel. The inf-sup stability of the lowest order Taylor–Hood pair on affine anisotropic meshes. *IMA Journal of Numerical Analysis*, 40(4):2377–2398, 07 2019.

[15] S. Basting and R. Prignitz. An interface-fitted subspace projection method for finite element simulations of particulate flows. *Comput Methods Appl Mech. Engrg.*, 267:133–149, 2013.

[16] M. Bause. On optimal convergence rates for higher-order Navier–Stokes approximations. I. Error estimates for the spatial discretization. *IMA Journal of Numerical Analysis*, 25(4):812–841, 2005.

[17] Y. Bazilevs, K. Takizawa, and T. E. Tezduyar. *Computational fluid-structure interaction: methods and applications*. John Wiley & Sons, 2013.

[18] R. Becker, M. Braack, D. Meidner, T. Richter, and B. Vexler. *The Finite Element Toolkit Gascoigne 3d*. 2021. `https://www.gascoigne.de`.

[19] R. Becker and R. Rannacher. Finite element solution of the incompressible Navier-Stokes equations on anisotropically refined meshes. *Notes on Numerical Fluid Mechanics*, 49:52–62, 1995.

[20] M. Behr and F. Abraham. Free-surface flow simulations in the presence of inclined walls. *Computer Methods in Applied Mechanics and Engineering*, 191:5467–5483, 11 2002.

[21] C. Bernardi. Optimal finite-element interpolation on curved domains. *SIAM J Numer Anal*, 26(5):1212–1240, 1989.

[22] J. M. Boland and R. A. Nicolaides. Stability of finite elements under divergence constraints. *Numerical Analysis*, 20:722–731, 1983.

[23] C. Börgers. A triangulation algorithm for fast elliptic solvers based on domain imbedding. *SIAM Journal on Numerical Analysis*, 27:1187–1196, 1990.

[24] M. Braack, R. Becker, D. Meidner, T. Richter, and B. Vexler. The finite element toolkit gascoigne (v1.01), 2021. doi.org/10.5281/zenodo.5574969.

[25] J. Bramble and J. King. A finite element method for interface problems in domains with smooth boundaries and interfaces. *Adv Comput Math*, 6:109–138, 1996.

[26] A. Brenner, E. Bänsch, and M. Bause. A priori error analysis for finite element approximations of the Stokes problem on dynamic meshes. *Ima Journal of Numerical Analysis*, 34:123–146, 2014.

[27] E. Burman, M. A. Fernández, and S. Frei. A Nitsche-based formulation for fluid-structure interactions with contact. *ESAIM: M2AN*, 54(2):531–564, 2020.

[28] E. Burman, M. A. Fernández, S. Frei, and F. M. Gerosa. A mechanically consistent model for fluid-structure interactions with contact including seepage. 2021. arXiv preprint: 2103.11243 [math.NA].

[29] E. Burman and P. Hansbo. Fictitious domain finite element methods using cut elements: II. a stabilized Nitsche method. *Applied Numerical Mathematics*, 62(4):328–341, 2012.

[30] E. Burman, C. He, and M. G. Larson. Comparison of shape derivatives using CutFEM for ill-posed Bernoulli free boundary problem. *Journal of Scientific Computing*, 88(2):1–28, 2021.

[31] S. Claus and P. Kerfriden. A CutFEM method for two-phase flow problems. *Computer Methods in Applied Mechanics and Engineering*, 348:185–206, 2019.

[32] D. Coutand and S. Shkoller. The interaction between Quasilinear Elastodynamics and the Navier-Stokes equations. *Rational Mech. Anal.*, 179:303–352, 2007.

[33] C. Crowe, J. Schwarzkopf, M. Sommerfeld, and Y. Tsuji. *Multiphase Flows with Droplets and Particles*. Taylor & Francis, 1997.

[34] G. de Rham. *Variétés Différentiables*. Hermann, Paris, 1960.

[35] I. Denisova and V. Solonnikov. Classical solvability of the problem on the motion of two viscous incompressible fluids. *St Petersburg Mathematical Journal*, 7:755–, 10 1996.

[36] I. V. Denisova. Solvability in Hölder spaces of a linear problem concerning the motion of two fluids separated by a closed surface. *Algebra i Analysis*, 5:122–148, 1993.

[37] R. L. DiPerna and P. Lions. Ordinary differential equations, transport theory and sobolev spaces. *Invent. Math.*, 98:511–547, 1989.

[38] T. Dupont. Mesh modification for evaluation equations. *Math.Comp.*, 39:85–107, 1982.

[39] L. Evans. *Partial differential equations*. American Mathematical Society, 2010.

[40] F. Brezzi, M. Fortin. *Mixed and hybrid finite element methods*. Springer, New York, 1991.

[41] X. Fang. An isoparametric finite element method for elliptic interface problems with nonhomogeneous jump conditions. *WSEAS Transactions on Mathematics*, 12, 2013.

[42] M. Feistauer and V. Sobotíková. Finite element approximation of nonlinear problems with discontinuous coefficients. *ESAIM: M2AN*, 24:457–500, 1990.

[43] L. Formaggia, A. Quarteroni, and A. Veneziani. *Cardiovascular Mathematics: Modeling and simulation of the circulatory system*, volume 1. Springer Science & Business Media, 2010.

[44] S. Frei. Eulerian finite element methods for interface problems and fluid-structure interactions. *PhD thesis, Heidelberg University, http://www.ub.uni-heidelberg.de/archiv/21590*, 2016.

[45] S. Frei. An edge-based pressure stabilization technique for finite elements on arbitrarily anisotropic meshes. *Int J Numer Methods Fluids*, 89(10):407–429, 2019.

[46] S. Frei, G. Judakova, and T. Richter. A locally modified second-order finite element method for interface problems and its implementation in 2 dimensions. *ESAIM: Mathematical Modelling and Numerical Analysis, DOI:10.1051/m2an/2023022*, 2023.

[47] S. Frei and T. Richter. A locally modified parametric finite element method for interface problems. *SIAM Journal on Numerical Analysis*, 52:2315–2334, 2014.

[48] S. Frei and T. Richter. An accurate Eulerian approach for fluid-structure interactions. In S. Frei, B. Holm, T. Richter, T. Wick, and H. Yang, editors, *Fluid-Structure Interaction: Modeling, Adaptive Discretization and Solvers*, Radon Series on Computational and Applied Mathematics, pages 69–126. Walter de Gruyter, Berlin, 2017.

[49] S. Frei and T. Richter. A second order time-stepping scheme for parabolic interface problems with moving interfaces. *ESAIM: Mathematical Modelling and Numerical Analysis*, 51(4):1539–1560, 2017.

[50] S. Frei, T. Richter, and T. Wick. Eulerian techniques for fluid-structure interactions: Part I–Modeling and simulation. In *Numerical Mathematics and Advanced Applications-ENUMATH 2013*, pages 745–753. Springer, 2015.

[51] S. Frei, T. Richter, and T. Wick. Eulerian techniques for fluid-structure interactions: Part II–Applications. In *Numerical Mathematics and Advanced Applications-ENUMATH 2013*, pages 755–762. Springer, 2015.

[52] S. Frei, T. Richter, and T. Wick. Long-term simulation of large deformation, mechano-chemical fluid-structure interactions in ALE and fully Eulerian coordinates. *Journal of Computational Physics*, 321:874 – 891, 2016.

[53] S. Frei, T. Richter, and T. Wick. An implementation of a locally modified finite element method for interface problems in deal.II. *Zenodo*, 2018. https://doi.org/10.5281/zenodo.1457758.

[54] S. Frei, T. Richter, and T. Wick. LocModFE: Locally modified finite elements for approximating interface problems in deal.ii. *Software Impacts*, 2021. to appear. ArXiV preprint: 1806.00999 [math.NA].

[55] S. Ganesan, G. Matthies, and L. Tobiska. On spurious velocities in incompressible flow problems with interfaces. *Computer Methods in Applied Mechanics and Engineering*, 196(7):1193–1202, 2007.

[56] P. Gangl. A local mesh modification strategy for interface problems with application to shape and topology optimization. In *Scientific Computing in Electrical Engineering*, pages 147–155. Springer, Cham, 2018.

[57] H. Garcke, K. F. Lam, R. Nürnberg, and E. Sitka. A multiphase Cahn–Hilliard–Darcy model for tumour growth with necrosis. *Mathematical Models and Methods in Applied Sciences*, 28(03):525–577, 2018.

[58] S. Gross and A. Reusken. *Numerical methods for two-phase incompressible flows*, volume 40. Springer Science & Business Media, 2011.

[59] C. Gürkan and A. Massing. A stabilized cut discontinuous Galerkin framework for elliptic boundary value and interface problems. *Computer Methods in Applied Mechanics and Engineering*, 348:466–499, 2019.

[60] M. Gurris, D. Kuzmin, and S. Turek. Finite element simulation of compressible particle-laden gas flows. *J. Computational Applied Mathematics*, 233(12):3121–3129, 2010.

[61] A. Hansbo and P. Hansbo. An unfitted finite element method, based on Nitsche's method, for elliptic interface problems. *Computer Methods in Applied Mechanics and Engineering*, 191(47-48):5537–5552, 2002.

[62] P. Hansbo, G. Larson, and S. Zahedi. A cut finite element method for a Stokes interface problem. *Applied Numerical Mathematics*, (85):90–114, 2014.

[63] J. G. Heywood and R. Rannacher. Finite element approximation of the nonstationary Navier–Stokes problem. i. regularity of solutions and second-order error estimates for spatial discretization. *SIAM Journal on Numerical Analysis*, 19(2):275–311, 1982.

[64] J. G. Heywood and R. Rannacher. Finite element approximation of the nonstationary Navier–Stokes problem. part iv: Error analysis for second-order time discretization. *SIAM Journal on Numerical Analysis*, 27(2):353–384, 1990.

[65] J. Hoffman, B. Holm, and T. Richter. The locally adapted parametric finite element method for interface problems on triangular meshes. In S. Frei, B. Holm, T. Richter, T. Wick, and H. Yang, editors, *Fluid-Structure Interaction: Modeling, Adaptive Discretization and Solvers*, Radon Series on Computational and Applied Mathematics, pages 41–68. de Gruyter, 2017.

[66] S. Höllbacher and G. Wittum. A sharp interface method using enriched finite elements for elliptic interface problems. *Numerische Mathematik*, 147(4):759–781, 2021.

[67] S.-R. Hysing, S. Turek, D. Kuzmin, N. Parolini, E. Burman, S. Ganesan, and L. Tobiska. Quantitative benchmark computations of two-dimensional bubble dynamics. *International Journal for Numerical Methods in Fluids*, 60(11):1259–1288, 2009.

[68] M. Ignatova, I. Kukavica, I. Lasiecka, and A. Tuffaha. On well-posedness and small data global existence for an interface damped free boundary fluid–structure model. *Nonlinearity*, 27:467, 02 2014.

[69] G. Judakova and M. Bause. Numerical investigation of multiphase flow in pipelines. *International Journal of Mechanical and Mechatronics Engineering*, 11(9):1540 – 1546, 2017.

[70] R. Kellogg. On the poisson equation with intersecting interfaces. *Applicable Anal.*, 4:101–129, 1975.

[71] S. Knauf, S. Frei, T. Richter, and R. Rannacher. Towards a complete numerical description of lubricant film dynamics in ball bearings. *Computational Mechanics*, 53(2):239–255, 2014.

[72] U. Langer and H. Yang. Numerical simulation of parabolic moving and growing interface problems using small mesh deformation. *Bericht-Nr. 2015-16; Johann Radon Institute for Computational and Applied Mathematics.*

[73] C. Lehrenfeld. High order unfitted finite element methods on level set domains using isoparametric mappings. *Comput Methods Appl Mech Eng*, 300:716 – 733, 2016.

[74] C. Lehrenfeld and A. Reusken. Analysis of a high order unfitted finite element method for an elliptic interface problem. *IMA J. Numer. Anal.*, 38:1351–1387, 2018.

[75] C. Lehrenfeld and A. Reusken. L^2-estimates for a high order unfitted finite element method for elliptic interface problems. *Journal of Numerical Mathematics*, 27:85–99, 2018.

[76] N. Moës, J. Dolbow, and T. Belytschko. A finite element method for crack growth without remeshing. 46:131–150, 1999.

[77] J. Nečas. *Equations aux Derivees Partielles*. Presses de Université de Montréal, Montréal, 1965.

[78] A. Nouri, F. Poupaud, and Y. Demay. An existence theorem for the multi-fluid Stokes problem. *Quarterly of applied mathematics*, LV:421–435, 1997.

[79] M. Olshanskii and A. Reusken. Analysis of a Stokes interface problem. *Numerische Mathematik*, 103:129–149, 2006.

[80] M. A. Olshanskii and A. Reusken. Analysis of a Stokes interface problem. *Numer. Math.*, (103):129–149, 2006.

[81] C. S. Peskin. Flow patterns around heart valves: a numerical method. *Journal of Computational Physics*, 10(2):252–271, 1972.

[82] R. Rannacher and S. Turek. Simple nonconforming quadrilateral Stokes element. *Numerical Methods Partial Differential Equations*, (8):97–111, 1992.

[83] T. Richter. *Fluid Structure Interactions: Models, Analysis and Finite Elements*. Springer, 2017.

[84] T. Richter and G. Judakova. Locally modified second order finite elements, 2021. doi.org/10.5281/ZENODO.5575064.

[85] D. Schötzau, C. Schwab, and R. Stenberg. Mixed hp-fem on anisotropic meshes. II. Hanging nodes and tensor products of boundary layer meshes. *Numerische Mathematik*, 83:667–697, 1999.

[86] V. Solonnikov. Solvability of a problem on the motion of a viscous incompressible fluid bounded by a free surface. *Izv. Akad. Nauk SSSR Ser. Mat.*, 41:6:1323–1358, 1977.

[87] V. Solonnikov. On the problem of non-stationary motion of two viscous incompressible liquids. *Journal of Mathematical Sciences*, 142:1844–1866, 04 2007.

[88] K. Stein, R. Benney, V. Kalro, T. E. Tezduyar, J. Leonard, and M. Accorsi. Parachute fluid–structure interactions: 3-d computation. *Computer Methods in Applied Mechanics and Engineering*, 190(3-4):373–386, 2000.

[89] R. Stenberg. A technique for analysing finite element methods for viscous incompressible flow. *International Journal for Numerical Methods in Fluids*, 11:935 – 948, 10 1990.

[90] T. Apel, S. Nicaise. The inf-sup condition for low order elements on anisotropic meshes. *Calcolo*, 322(41):89–113, 2004.

[91] K. Tanaka, K. Sekine, M. Mizuguchi, and S. Oishi. Estimation of Sobolev-type embedding constant on domains with minimally smooth boundary using extension operator. *Journal of Inequalities and Applications*, 2015(1):1–23, 2015.

[92] R. Temam. *Navier-Stokes Equations: Theory and numerical analysis*. American Mathematical Society, Providence, 2000.

[93] V. Girault, P.-A. Raviart. *Finite element methods for Navier-Stokes equations. Theory and algorithms*. Springer Series in Computational Mathematics. Springer-Verlag Berlin Heidelberg, 1986.

[94] F. Van de Vosse, J. De Hart, C. Van Oijen, D. Bessems, T. Gunther, A. Segal, B. Wolters, J. Stijnen, and F. Baaijens. Finite-element-based computational methods for cardiovascular fluid-structure interaction. *Journal of Engineering Mathematics*, 47(3):335–368, 2003.

[95] A. Vogel, S. Reiter, M. Rupp, A. Nägel, and G. Wittum. Ug 4: A novel flexible software system for simulating PDE based models on high performance computers. *Comput Visual Sci*, 16(4):165–179, 2013.

[96] I. Voulis and A. Reusken. A time dependent Stokes interface problem: well-posedness and space-time finite element discretization. *ESAIM: M2AN*, 52:2187–2213, 2019.

[97] A. Ženíšek. The finite element method for nonlinear elliptic equations with discontinuous coefficients. *Numerische Mathematik*, 58:51–77, 1990.

[98] W. A. Wall and T. Rabczuk. Fluid–structure interaction in lower airways of CT-based lung geometries. *International Journal for Numerical Methods in Fluids*, 57(5):653–675, 2008.

[99] J. Wloka. *Partielle Differentialgleichungen*. Teubner, Stuttgart, 1982.

[100] H. Xie, K. Ito, Z.-L. Li, and J. Toivanen. A finite element method for interface problems with locally modified triangulation. *Contemporary Mathematics*, 466:179–190, 2008.